

Engineering-Oriented, Image-based 3D Data Acquisition with Applications

by

Chunsheng Yu

Advisor: Prof. **Qingjin Peng**

A Thesis submitted to the Faculty of Graduate Studies of
The University of Manitoba
in partial fulfilment of the requirements of the degree of

Doctor of Philosophy

Department of Mechanical & Manufacturing Engineering

The University of Manitoba

Copyright © 2008 by Chunsheng Yu

THE UNIVERSITY OF MANITOBA
FACULTY OF GRADUATE STUDIES

COPYRIGHT PERMISSION

Engineering-Oriented, Image-based 3D Data Acquisition with Applications

BY

Chunsheng Yu

**A Thesis/Practicum submitted to the Faculty of Graduate Studies of The University of
Manitoba in partial fulfillment of the requirement of the degree**

Of

Doctor of Philosophy

Chunsheng Yu © 2008

**Permission has been granted to the University of Manitoba Libraries to lend a copy of this
thesis/practicum, to Library and Archives Canada (LAC) to lend a copy of this
thesis/practicum, and to LAC's agent (UMI/ProQuest) to microfilm, sell copies and to
publish an abstract of this thesis/practicum.**

**This reproduction or copy of this thesis has been made available by authority of the
copyright owner solely for the purpose of private study and research, and may only be
reproduced and copied as permitted by copyright laws or with express written
authorization from the copyright owner.**

Abstract

This dissertation presents research and development of image-based 3D data acquisition methods from an engineering perspective. The automation, low cost, portability and flexibility of these data acquisition methods are required for engineering applications. The goal of this research is to simplify the processing and interactive operations between operators and image-based 3D data acquisition systems. The research in this dissertation includes improving image-based 3D data acquisition methods, and applying proposed methods to two engineering applications.

An automatic recognition method for the detection of a checkerboard pattern with five double-triangle figures is proposed for camera calibration. This method has been tested in different lighting conditions with a complicated background and in different view orientations. A unified-calibration method for FTP (Fourier Transform Profilometry) methods is proposed to determine the system parameters. The proposed method unifies the height calibration and the plane calibration in one step. There is only one image of the specially designed pattern required to calibrate the 3D data acquisition system of FTP methods, making calibration simpler and faster. A new phase unwrapping algorithm based on a correlation map for FTP methods is proposed to generate reliable phase data. The phase unwrapping algorithm is further simplified by avoiding the necessity of choosing the width of the filter window.

The first engineering application developed in this research is to monitor ice accretions on power transmission lines for Manitoba Hydro. The edge detection, epipolar line and

correlation methods are combined in a practical way to find the ice shape. It provides an effective approach to detect ice accretion on power transmission lines.

The second application developed is a VR (Virtual Reality)-based data retrieval system to search product data in virtual environments. It enables users to have an overview of the product data structure and to find relevant information rapidly. Web technology is used in the system for communication and data sharing. UML (Unified Model Language) is used to analyze the process of product and system design. An image-based 3D data acquisition system is developed. The system can also be used to aid 3D modeling for virtual environments.

Acknowledgements

This dissertation could not be finished without the support of many people. This is my opportunity to thank all these people for their suggestions, encouragement and assistance.

First, I would like to express my gratitude towards my advisor, Dr. Qingjin Peng, who gave me the opportunity to work with his research group. He provided me an exciting working environment with many opportunities to develop new ideas and work on industrial applications.

I would like also to thank Dr. Walton and Dr. ElMekkawy for the valuable comments and suggestions to my research as members of my study committee.

I am also indebted to many colleagues. I would like to especially acknowledge Mr. W. Hu and Mr. P. Wang working for the ice detection project. I would also like to thank all my colleagues, Chulho Chung, Xiumei Kang, Hector Sanchez, Heewan Lee, Mahmud Ahsan, Qing Niu, Tingting Zhao and Tao Luan. They made these years at University of Manitoba as a pleasant time.

The financial support of the Natural Sciences and Engineering Research Council of Canada (NSERC) and Manitoba HVDC Research Centre Inc. is also gratefully acknowledged.

Last but not least, I would like to thank my family for their support. This is very important to me. First and the most, I want to express my gratitude and love to my wife, Jinhua Li for never ending support, love and understanding. I would like to thank my mother-in-law, Wangsheng Huang, who took care of my daughter through my thesis writing. I would also like to thank the support from my parents Hongcheng Yu and

Yajuan Wang and my brother Chunshui Yu. They deserve to be proud of their contribution to my Ph.D. degree. At last, I want to express my love to my daughter Winnie Zhujia Yu and my son Samuel Zhuxiu Yu.

List of Abbreviations

Abbreviation	Description
1D	One dimensional
2D	Two dimensional
2D FTP	Two-dimensional Fourier transform profilometry
3D	three dimensional
BMP	Bitmap
CAD	Computer-Aided Design
CE	Concurrent Engineering
CCD	Charged Couple Device
CNC	Computer Numerical Control
CT	Industrial X-Ray Computed Tomography
CMM	Coordinate Measuring Machine
DFT	discrete Fourier transform
FTP	Fourier Transform Profilometry
GA	Genetic Algorithms
HMD	Head mounted display
IFTP	Improved Fourier transform profilometry
IGES	Initial Graphics Exchange Specification
IRM	Icing-Rate Meter
JPEG	Joint Photographic Experts Group

MFTP	Modified Fourier transform profilometry
MRPII	Manufacturing Resource Planning
OpenCV	Open Computer Vision Library
PDM	Product Data Management
PMP	Phase-measuring profilometry
SFS	Shape-from-shading
SQL	Structured Query Language
STEP	Standard for The Exchange of Product model data
TDI	Time Delay and Integration
UML	Unified Model Language
USB	Universal Serial Bus
VR	Virtual Reality
VRML	Virtual Reality Model Language
XML	eXtensible Markup Language

List of Notations

Symbol	Description
CM	The correlation-map function
$Corr$	The correlation function
E	The essential matrix
f	The focal length
F	The fundamental matrix
f_r	The spatial frequency of the projected fringes in the reference plane
f_{r0}	The fundamental frequency of an observed grating image
H	3×3 homography matrix
$I(x, y)$	The gray intensity of a pixel at (x, y)
K	The intrinsic matrix
$M(x, y)$	The modulation of a deformed grating image
P	The perspective projection matrix
R	3×3 rotation matrix,
t	3D translation vector,
$\Delta\phi(x, y)$	The phase information

List of Figures

Figure 1.1	A family tree of 3D data acquisition methods	2
Figure 1.2	The overview of research objective	6
Figure 1.3	The structure of this dissertation	11
Figure 2.1	Laser scanner	14
Figure 2.2	(a) An image without grating; (b) An image with deformed grating; (c) 3D plot of the reconstructed object.	17
Figure 2.3	Geometry structure of a pattern and the image of the pattern	18
Figure 2.4	Two types of the calibration pattern	19
Figure 2.5	Two geometries of the FTP method	22
Figure 2.6	The calibrating model plane	23
Figure 2.7	Calibration patterns	24
Figure 2.8	The layout of a system calibration	25
Figure 2.9	A 1-D phase distribution and how it appears when wrapped modulo 2π	26
Figure 2.10	The 1D spatial frequency spectra of a pure fringe pattern	29
Figure 2.11	The 1D spatial frequency spectra of a fringe pattern with noise and objects	29
Figure 3.1	An overview of the process of the calibration-based 3D data acquisition	37
Figure 3.2	An example of a pair of corresponding image points	38
Figure 3.3	Digital image formation	39

Figure 3.4	A pinhole model with the optical center is in front of the image plane	40
Figure 3.5	A pinhole model with the image plane is in front of the optical center	40
Figure 3.6	An digital image in 2D array format	41
Figure 3.7	The process of spatial filtering	43
Figure 3.8	The mask for point detection	44
Figure 3.9	Roberts cross	46
Figure 3.10	Prewitt mask	47
Figure 3.11	Sobel mask	47
Figure 3.12	The correlation-matching process	49
Figure 3.13	Perspective projection from the world coordinate system to the image plan	50
Figure 3.14	Illustration of pixel dimensions	52
Figure 3.15	2D homography	53
Figure 3.16	The epipolar geometry	55
Figure 3.17	The geometry of the triangulation method	58
Figure 4.1	proposed checkerboard pattern with special designed figures	60
Figure 4.2	The coordinate systems defined by a checkerboard pattern	61
Figure 4.3	Double-triangle figure, a template and correlation map	64
Figure 4.4	Coordinate system of the pattern	66
Figure 4.5	The block diagram of the feature detection	67
Figure 4.6	Example of a template image and template size (20x20 pixels)	67

Figure 4.7	Even lights of indoor (template size 11*11, rotate angle: 0)	70
Figure 4.8	High contrast lighting at the indoor environment (template size 11*11, rotate angle: 0)	71
Figure 4.9	Sun light with complex background (template size 15*15, rotate angle: 0)	71
Figure 4.10	Sun light with shade (template size 15*15 rotating angle: 5)	71
Figure 4.11	Pattern in an angle (template size 11*11, rotating angle: 12)	72
Figure 4.12	The picture is taken by Kodak digital camera (template size 11*11, rotating angle: -10)	72
Figure 4.13	The picture is taken by Sumsung camcorder (template size 11*11, rotating angle: 0)	72
Figure 4.14	Images of the new checkerboard pattern	74
Figure 5.1	A geometry structure of the projection and image system	76
Figure 5.2	Filtering in the Fourier spectrum	78
Figure 5.3	Coordinate system for 3D coordinates calculation	79
Figure 5.4	A sinusoidal grating	80
Figure 5.5	Coordinate systems for 3D coordinates calculation	81
Figure 5.6	The helper pattern	82
Figure 5.7	Geometry structures of the camera, the projector and the helper pattern	83
Figure 5.8	Geometry structure of the image and the helper pattern	86
Figure 5.9	System hardware and layout	87
Figure 5.10	The overall process of the FTP-based 3D data acquisition	88

Figure 5.11	(a) The dimensions of the helper pattern; (b) Original image of the holder	89
Figure 5.12	The image of the helper pattern	90
Figure 5.13	(a) Sinusoidal grating image (b) Deformed grating and the holder	91
Figure 5.14	The recovered shape of the holder	91
Figure 5.15	Profile of the holder that is measured by CMM	92
Figure 5.16	Profile of the holder that is obtained by FTP	92
Figure 6.1	The process of 1D phase unwrapping algorithm	96
Figure 6.2	A phase distribution with two “ spot noise”	96
Figure 6.3	The phase distribution after phase unwrapping	97
Figure 6.4	The process of reliability-based phase unwrapping algorithm	98
Figure 6.5	The source image and four computer-generated fringe images	99
Figure 6.6	The relationship of the correlation-map function with the intensity of the image background	101
Figure 6.7	The relationship of the correlation-map function with the intensity of the image background with noise	101
Figure 6.8	The proposed algorithm of the correlation based phase unwrapping method	103
Figure 6.9	The process of the phase unwrapping	103
Figure 6.10	The layout of the experimental system	105
Figure 6.11	The deformed fringe pattern on the kettle	105
Figure 6.12	Computer generated fringe images	106

Figure 6.13	The wrapped phase obtained by FTP method	106
Figure 6.14	The modulation map and the correlation map for phase unwrapping	106
Figure 6.15	The result obtained by using the 1D phase unwrapping algorithm	107
Figure 6.16	The comparison result obtained by the correlation method	108
Figure 6.17	The comparison result obtained by the modulation method	109
Figure 6.18	The comparison result obtained by the modulation method with a wider window	109
Figure 7.1	The framework of the 3D ice detection system	112
Figure 7.2	The workflow of points matching	114
Figure 7.3	Feature-based and area-based points matching method	115
Figure 7.4	Flow chart of the algorithm of 3D ice thickness acquisition	115
Figure 7.5	Peak points on an ice image	117
Figure 7.6	System structure	119
Figure 7.7	The component diagram of the ice detection system	120
Figure 7.8	The camera calibration	126
Figure 7.9	Multiple scan to detect ice edges	126
Figure 7.10	Epipolar lines in two images	127
Figure 7.11	The 3D coordinates calculation of peak points on edges of the ice	127
Figure 7.12	System installation	128
Figure 7.13	Hoarfrost on the power transmission line at daytime	129
Figure 7.14	Hoarfrost on the power transmission line at night	129

Figure 7.15	Ice on the power transmission line at daytime	130
Figure 7.16	Ice on the power transmission line at night	130
Figure 8.1	The framework of the VR-based data retrieval system	132
Figure 8.2	System structure of the integrated product database	134
Figure 8.3	The VR construction from different data	137
Figure 8.4	The structure of the VR-based user interface	138
Figure 8.5	The structure of the image based 3D data acquisition system	140
Figure 8.6	User interfaces for photogrammetry method	141
Figure 8.7	User interfaces for FTP method	142
Figure 8.8	A general product design and manufacturing process	143
Figure 8.9	Class diagram of product data deposit	144
Figure 8.10	HMD and Data-glove	145
Figure 8.11	System structure of getting data from product data deposit	146
Figure 8.12	Interface of EON software with VR Hardware	148
Figure 8.13	The structure of the virtual user	149
Figure 8.14	Implementation of virtual user control	149
Figure 8.15	The system user interface	150
Figure 8.16	2D drawing in the VR-based user interface	151
Figure 8.17	The flow chart of building a 3D model of the CMM machine	152
Figure 8.18	The images for camera calibration	152
Figure 8.19	The image of the CMM machine	153
Figure 8.20	Two images for measuring parts 1 and 2	153
Figure 8.21	Two images for measuring widths and heights of parts 3 to 9	154

Figure 8.22	Two images for measuring widths of parts 3 to 9	154
Figure 8.23	The 3D model of the CMM machine	155

List of Tables

Table 4.1	Experimental results of the intrinsic parameters of the camera	74
Table 4.2	Experimental results of the extrinsic parameter for one image	74
Table 5.1	A comparison of the unified calibration method and other calibration methods	93
Table 7.1	The functions in the server program	120
Table 7.2	The functions in the client program	120
Table 7.3	The network protocol in server side	121
Table 7.4	The network protocol in client side	121
Table 7.5	List of commands	124
Table 7.6	Experimental results of ice thickness calculation	128
Table 8.1	Function of class in the model of product data deposit	144
Table 8.2	The dimensions of the CMM machine	155

CONTENTS

ABSTRACT	I
ACKNOWLEDGEMENTS.....	III
LIST OF ABBREVIATIONS	V
LIST OF NOTATIONS.....	VII
LIST OF FIGURES.....	VIII
LIST OF TABLES.....	XV
CHAPTER 1 INTRODUCTION	1
1.1 ANALYSIS OF TECHNIQUES FOR 3D DATA ACQUISITION.....	1
1.2 APPLICATION AREAS	4
1.3 THE RESEARCH SCOPE AND OBJECTIVES	5
1.4 CONTRIBUTIONS	8
1.5 OUTLINE OF THE DISSERTATION	9
CHAPTER 2 LITERATURE REVIEW	12
2.1 REVIEW OF 3D DATA ACQUISITION METHODS	12
2.2 CAMERA CALIBRATION	17
2.3 SYSTEM CALIBRATION FOR FTP METHODS.....	21
2.4 PHASE UNWRAPPING FOR FTP METHODS.....	25
2.5 ICE DETECTION SYSTEM.....	29
2.6 PRODUCT DATA RETRIEVAL SYSTEMS.....	34
CHAPTER 3 BACKGROUND	36
3.1 A BRIEF INTRODUCTION ON CALIBRATION-BASED 3D DATA ACQUISITION.....	36
3.2 CAMERA MODEL.....	38
3.3 2D IMAGES	41

3.4 IMAGE PRE-PROCESSING	42
3.5 FEATURE EXTRACTION	44
3.6 FEATURE MATCHING BY CORRELATION	47
3.7 THE INTRINSIC AND EXTRINSIC PARAMETERS OF A CAMERA.....	50
3.8 2D HOMOGRAPHY	53
3.9 EPIPOLAR GEOMETRY	54
3.10 3D RECONSTRUCTIONS FROM TWO 2D IMAGES	56
CHAPTER 4 AUTOMATIC DETECTION OF CHECKERBOARD PATTERN FOR CAMERA CALIBRATION	59
4.1 INTRODUCTION	59
4.2 PATTERN BASED CAMERA CALIBRATION	60
4.3 PATTERN DESIGN.....	63
4.4 POSITION CHECK OF DOUBLE-TRIANGLE FIGURES.....	65
4.5 AUTOMATIC DETECTION OF CHECKERBOARD	66
4.6 EXPERIMENTS	69
CHAPTER 5 A UNIFIED CALIBRATION METHOD IN FTP METHODS	75
5.1 INTRODUCTION	75
5.2 THE FTP METHOD AND 3D COORDINATES CALCULATION	76
5.3 IMAGE-BASED PARAMETER MEASUREMENT METHODS	82
5.4 A FTP-BASED 3D DATA ACQUISITION SYSTEM WITH UNIFIED CALIBRATION	86
5.5 EXPERIMENTS AND DISCUSSIONS.....	89
CHAPTER 6 CORRELATION BASED PHASE UNWRAPPING IN FTP METHODS.....	94
6.1 INTRODUCTION	94
6.2 1D PHASE UNWRAPPING ALGORITHM	95
6.3 THE RELIABILITY-GUIDED PHASE UNWRAPPING ALGORITHM.....	97
6.4 ANALYSIS OF THE CORRELATION-BASED PHASE UNWRAPPING METHOD.....	98

6.5 THE PROPOSED ALGORITHM FOR THE CORRELATION BASED PHASE UNWRAPPING METHOD.....	102
6.6 THE EXPERIMENTS	104
CHAPTER 7 THE IMAGE-BASED 3D ICE DETECTION SYSTEM.....	110
7.1 INTRODUCTION.....	110
7.2 THE 3D ICE DETECTION METHOD.....	113
7.3 DEVELOPMENT OF THE ICE DETECTION SUPPORT SYSTEM.....	118
7.4 EXPERIMENTS	124
CHAPTER 8 A VR-BASED DATA RETRIEVAL SYSTEM	131
8.1 THE FRAMEWORK OF THE VR-BASED DATA RETRIEVAL SYSTEM.....	131
8.2 KEY TECHNOLOGIES IN THE FRAMEWORK IMPLEMENTATION	133
8.3 VR-BASED USER INTERFACE	136
8.4 IMAGE BASED 3D DATA ACQUISITION SYSTEM	138
8.5 AN EXAMPLE AND DISCUSSION.....	142
8.6 CMM MACHINE MODELING.....	151
CHAPTER 9 CONCLUSIONS AND FUTURE RESEARCH	156
9.1 SUMMARY	156
9.2 FUTURE RESEARCH.....	158
BIBLIOGRAPHY	160
CURRICULUM VITAE	174

Chapter 1

Introduction

This chapter introduces techniques of three-dimensional (3D) data acquisition related to the research work. The analysis of techniques for 3D data acquisition is presented first, and then the demand for developing image-based 3D data acquisition from engineering perspective is discussed. The scope of this research and contributions made are also presented in this chapter.

1.1 Analysis of techniques for 3D data acquisition

3D data are a set of spatial coordinates of an object. Obtaining 3D data of the object is the first step in acquiring details of an object. Many engineering applications require 3D data, such as reverse engineering, product quality control, product inspection and virtual manufacturing. 3D data acquisition is an essential research topic in engineering.

A number of 3D data acquisition methods have been developed. A family tree of 3D data acquisition methods is shown in Figure 1.1. These methods are divided into two categories: contact and non-contact approaches. Contact approaches have contact with object's surface during the data acquisition, whereas non-contact ones do not have contact with the object in the measurement. Contact sensors are typically touch probes that consist of jointed arms attached to a narrow pointer. A 3D shape can be measured by positioning the probe on the object and triggering the computer to record positions of the probe. Non-contact methods are generally operated by projecting energy waves onto an object followed by recording the

transmitted or reflected energy. Reflective methods for 3D data acquisition are subdivided into three categories: Radar, Laser and Image-based methods. In these methods, different types of energy including radar, laser or light are projected onto the surface of an object in a structured manner. By measuring the reflection from the object, 3D data of the object can be obtained. In image-based methods, lighting is projected onto the object and 3D data are extracted from one or more digital images captured from the object. The advantage and disadvantage of these methods will be reviewed in Chapter 2.

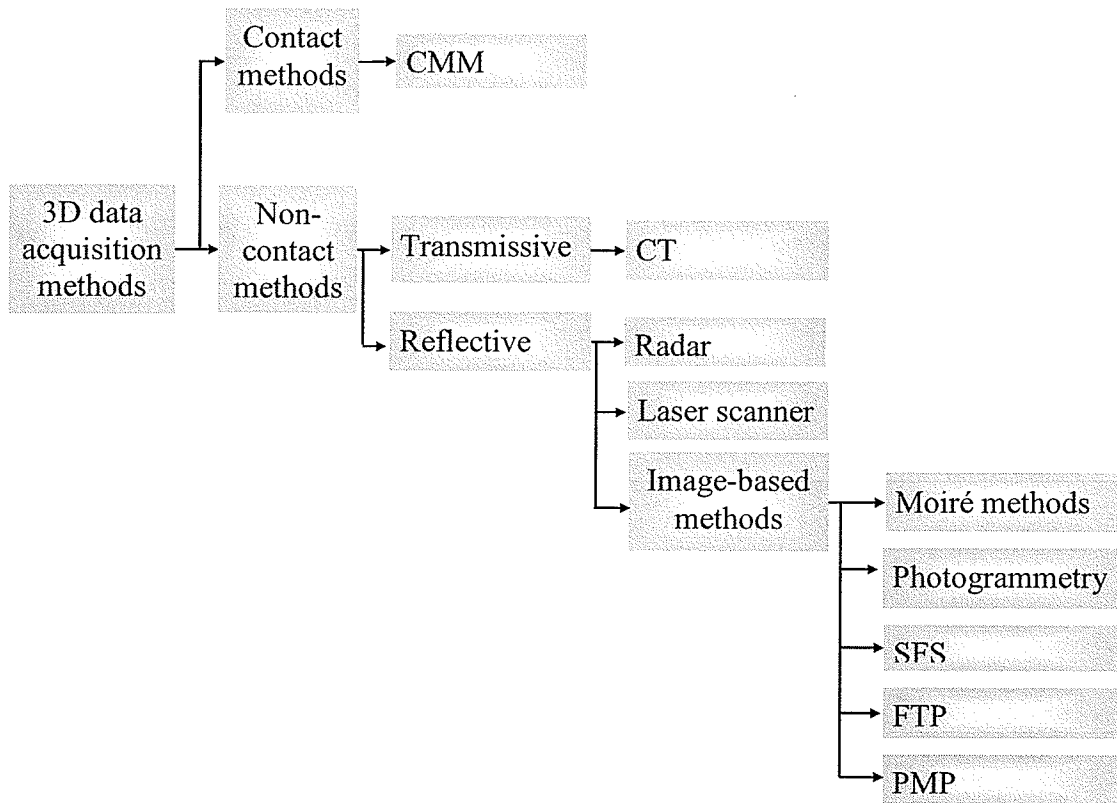


Figure 1.1 A family tree of 3D data acquisition methods

These 3D data acquisition methods vary in their accuracy, measurement range and calculation speed, and each is suitable for certain types of applications. From the engineering perspective, 3D data acquisition methods with automation, low cost, portability and

flexibility are required. Therefore, 3D data acquisition methods that do not meet these criteria are not the solution for this purpose: these would include such methods as Industrial X-Ray Computed Tomography (CT), laser scanners and Coordinate Measuring Machines (CMMs). The image-based 3D data acquisition methods provide a low-cost solution to acquire 3D data of objects because of the decreasing cost of computer systems and electronic products. Digital cameras are quick, adaptable and portable tools for collecting data. Therefore, this research will focus on image-based 3D data acquisition methods. Among the image-based methods, the Fourier Transform Profilometry (FTP) method is easier to install than the Phase-measuring profilometry (PMP) and the Moiré methods, and more flexible than the Shape-from-shading (SFS) method. But the FTP method is only suitable for small and medium-sized objects with freeform surfaces. The photogrammetry method is suitable for large, medium and small sized objects. But it is not capable of producing accurate 3D data for an unmarked and freeform surface. The cooperation of two methods is a feasible approach to 3D data acquisition for different sizes and types of objects. The research presented in this dissertation proposes some new methods to enhance the existing FTP and Photogrammetry methods from the engineering perspective. Simplifying the operation process of these methods and reducing the interactive manipulation between operators and computers are goals of this research.

In this research, 3D data acquisition methods are employed in two engineering applications. One is the 3D shape acquisition of ice accretions on power transmission lines. The other is the 3D data acquisition for a Virtual Reality (VR)-based data retrieval system.

1.2 Application areas

Algorithms of 3D data acquisition from the engineering perspective are a major consideration in this research. The proposed algorithms should be able to be applied to 3D data acquisition in any engineering application. In particular, this research focuses on two engineering applications that are explained as below.

The first application is the image-based 3D acquisition of ice accretions on power transmission lines. It is embedded in the project “Development of a digital image recognition system to detect ice accretions on conductors”, a co-operative research project with the Manitoba HVDC Research Centre, Inc. When power transmission lines are exposed to severe ice loads they are at risk of tearing down pole cross-arms and associated hardware. Repair is costly. The early detection and knowledge of ice accretion on power transmission lines will assist in minimizing damage cost. In this research, an image-based 3D ice acquisition algorithm is proposed to monitor ice accretions on power transmission lines. The ice accretion on power transmission lines is monitored by measuring ice thickness continuously. The proposed detection system is a new concept enabling cost-effective decision making for removing ice, and is therefore valuable to the corporation. An automatic checkerboard detection algorithm developed for the photogrammetry method is applied in this research.

The second application is the image-based 3D data acquisition for a VR-based data retrieval system. VR is a computer-generated 3D environment. VR provides users a virtual design and manufacturing environment. Users can design 3D models of a product, simulate the manufacturing process and analyze the product function in the virtual environment. Some examples are as follows. In product design: a VR system can handle the viewing and the

examination of product assemblies (Jezernik and Hren, 2003); CAD (Computer-aided Design) models can be explored in an immersive VR environment (Paillot et al, 2003); VR environments can be used in product development and evaluation (Bao et al, 2002; Moore et al, 2003). In the product manufacturing: VR environments can be used for simulating manufacturing operations (Chawla and Banerjee, 2001); a layout planning tool can be developed using VR environments (Korves and Loftus, 2000). VR environments have also been used in the manufacturing training system (Fernandesa et al, 2003). In the research presented in this dissertation, a VR-based data retrieval system is proposed. A VR-based interface is used to represent product hierarchical information for understanding overall product information easily and finding relevant information rapidly. An important part of the VR-based data retrieval system is 3D model construction. The FTP and Photogrammetry methods are applied in an image-based 3D data acquisition system to acquire the 3D data of existing objects; the data are then used for VR environment construction with a cost-effective solution. The techniques developed for this application can also be applied to other virtual environment constructions.

1.3 The research scope and objectives

There are variant algorithms designed for FTP and Photogrammetry methods. However, these algorithms are normally designed purely from a theoretical perspective, not from an engineering application perspective. From the engineering perspective, a simple process with automatic operation is preferable. Therefore the goals of this research are to simplify the operating procedures of FTP and Photogrammetry methods, and to reduce interactive manipulations between operators and computers in both methods.

The objectives of acquiring 3D data by photogrammetry and FTP methods are shown in Figures 1.2 and explained below.

- (1) Finding a checkerboard recognition method for the automatic camera calibration of photogrammetry. A reliable detection of calibration patterns will be developed.
- (2) Exploring an easy and quick way to calibrate FTP-based 3D data acquisition systems. In current FTP methods, the calibration procedure includes a height calibration (Z-axis) and a plane calibration (X-axis and Y-axis). A series of images are taken in different locations of the calibration pattern. The mass data of the images have to be processed. The calibration is a time-consuming process. A simple and fast way to calibrate the FTP-based 3D data acquisition system is required.

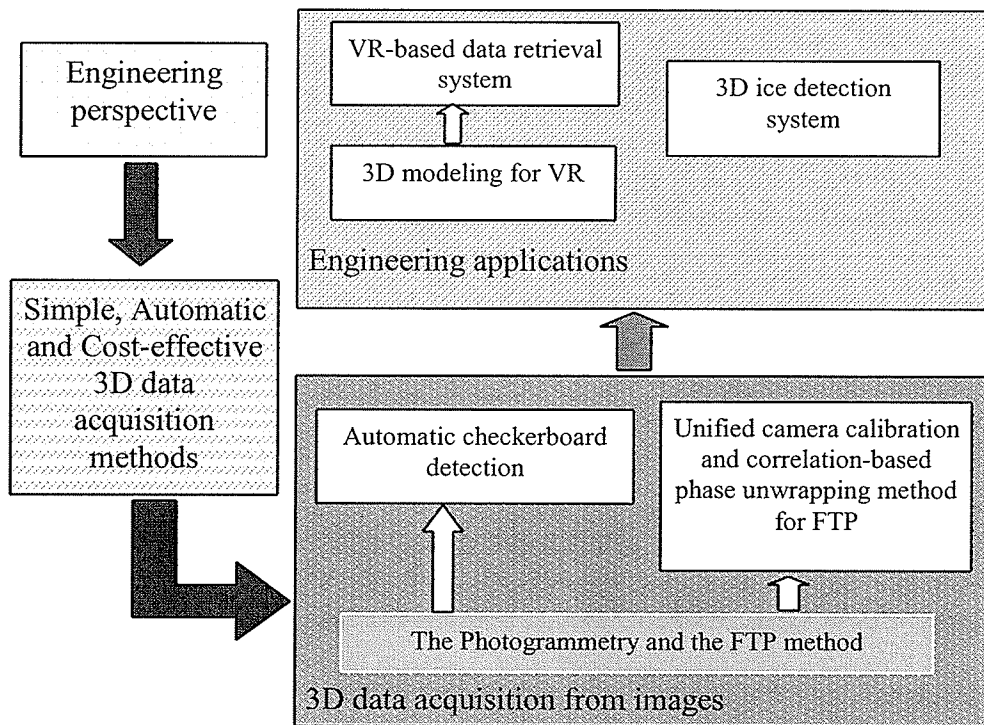


Figure 1.2 The overview of research objectives

(3) Investigating a simplified phase unwrapping method for FTP methods. In current quality-guided phase unwrapping methods, a modulation function is normally used for phase unwrapping. A filter window is required to calculate the modulation function. It takes time to obtain a proper width of the filter window. A simplified phase unwrapping method is needed for efficiently obtaining a proper width of the filter window.

(4) Searching for an effective way to match corresponding points in two ice images. Required by the photogrammetry method, it is to be applied in the 3D ice detection system. The difficulty is to find the corresponding points in the ice images, as the ice is transparent or semi-transparent and the surface of the ice is smooth; therefore it is easily affected by background noise. The noise may decrease the gradient to deteriorate the performance of feature detection. As the ice thickness calculation will only need the 3D information on the top and bottom edges of the ice, rather than the total surface, the interested corresponding points will only be located on the ice edges. These points will be used to calculate the maximum ice thickness along a power transmission line.

(5) Implementing the proposed methods for VR constructions. The Photogrammetry and FTP methods will be applied to 3D modeling for VR systems. A software environment for the proposed methods will be developed. With this software, experience can be gained on applying the proposed methods to VR constructions.

(6) Developing a VR-based data retrieval system. Concurrent Engineering (CE) is an approach to integrate resources in product development. It involves all procedures of product development in parallel. Collaboration is a fundamental element in CE applications (Salomone, 1995). Product information should be accessed conveniently and managed effectively. The current research focuses on the integration of product information rather than

a user-friendly search interface to retrieve information effectively. However, we believe it is necessary to have an easy-to-use system to search and view product information.

1.4 Contributions

In this research, three novel methods are developed for obtaining 3D data from 2D (two-dimensional) images. The methods are implemented in two applications. The contributions of this research consist of the following two parts.

1. The development of three novel methods for the 3D data acquisition process as follows:

- An automatic recognition method is proposed for the detection of a checkerboard pattern in the camera calibration. The experimental results show that the method is robust over a range of illuminations and various backgrounds. The proposed method can be used for automatic camera calibration in real-world environments. This work is published in the *Journal of Optical Engineering* (Yu and Peng, 2006).
- A unified-calibration method is proposed for the FTP method. There is only one image of a specially designed pattern required in the calibration of the FTP-based 3D data acquisition system. The height calibration and the plane calibration are unified in one step. The experiments show that the method is feasible for FTP-based 3D data acquisition. This work is published in the *Journal of Optics and Laser in Engineering* (Yu and Peng, 2007).
- A new phase unwrapping algorithm based on the correlation map for the FTP method is proposed. A correlation-map function is proposed to calculate the reliability of the fringe image and to avoid choosing the width of the window in calculating the modulation. As the value of the correlation-map function is lower in areas of local shadow and has more abrupt

discontinuity than in other areas, the correlation-map function is used as a guide to find the optimized phase unwrapping path. The experimental results show the method is feasible. This work is published in the Journal of Optics and Laser in Engineering (Yu and Peng, 2007).

2. Applications of the proposed methods in following areas:

- A novel method is developed to monitor ice accretions on power transmission lines using an image-based 3D detection technique. The method uses two ice images of the same power transmission line taken by two cameras to calculate the 3D ice shape. The automatic camera calibration method proposed in this research is used to calibrate two cameras and calculate the essential matrix. The benefit of this research is to provide early warning of ice accretion to minimize damage cost to power transmission lines. This work is published in IEEE Canada 2006 (Yu et al, 2006).

- A VR-based data retrieval system for product design and manufacturing is proposed. The system not only provides an integrated product database but also uses VR and Web technologies for easing navigation of product data and for searching product data in a virtual design and manufacturing environment. This work is published in the Proceedings of ASME 2005 International Design Engineering Technical Conference (Yu and Peng, 2005).

1.5 Outline of the dissertation

Following parts of this dissertation are organized as follows:

Chapter 2 reviews literature in the related fields that include 3D data acquisition methods, camera calibration, system calibration for FTP methods and phase unwrapping algorithm for

FTP methods. Technologies related to image-based ice detection and VR-based data retrieval systems are also reviewed. The problem statement and research strategy for each area are presented in this chapter.

Chapter 3 explains the background of the photogrammetry method. Basic concepts used in this research are presented. The pinhole model of a camera, the image formation and 3D reconstruction from two 2D images are introduced. Some properties of the epipolar line, homography, and image formation processing are described. Feature extraction and correlation-based feature matching are also introduced in this chapter.

Chapter 4 introduces the automatic recognition of a new checkerboard for the camera calibration. This approach is based on the homography constraint of two 2D images. A new checkerboard with five double-triangle figures is designed. An iterative algorithm and a homography method are discussed in order to find the position of the new checkerboard in images. The experimental results are presented at the end of this chapter.

Chapter 5 discusses unified-calibration for the FTP method. First a general calibration procedure and the principle of FTP methods are introduced. Then the system parameters for calibration are derived from this principle. After the algorithm of the unified-calibration method is introduced, the experimental results are presented in the end of this chapter.

Chapter 6 introduces a correlation-based phase unwrapping method for the FTP method. First, the 1D phase unwrapping algorithm and the reliability-guided phase unwrapping algorithm are introduced. A correlation-map function is then introduced to calculate the reliability of the fringe image. The algorithm of the correlation-based phase unwrapping is developed. Finally, the experimental results of the 1D phase unwrapping method and the reliability-guided phase unwrapping method are presented.

Chapter 7 describes the image-based 3D ice detection system. The development of the system includes two parts: one is the algorithm for searching corresponding points in two ice images; the other is the software to support the hardware. The experimental results of the algorithm and the support software are presented.

Chapter 8 introduces a VR-based data retrieval system. The framework of the system, the key technologies in implementing this framework and the principles of constructing the VR-based user interface are discussed. An image-based 3D data acquisition system to aid in building the 3D user interface is introduced. Implementing this system in the VR-based data retrieval system is also presented in this chapter.

The conclusions and further research are presented in Chapter 9. The organisation of the dissertation is summarised in Figure 1.3.

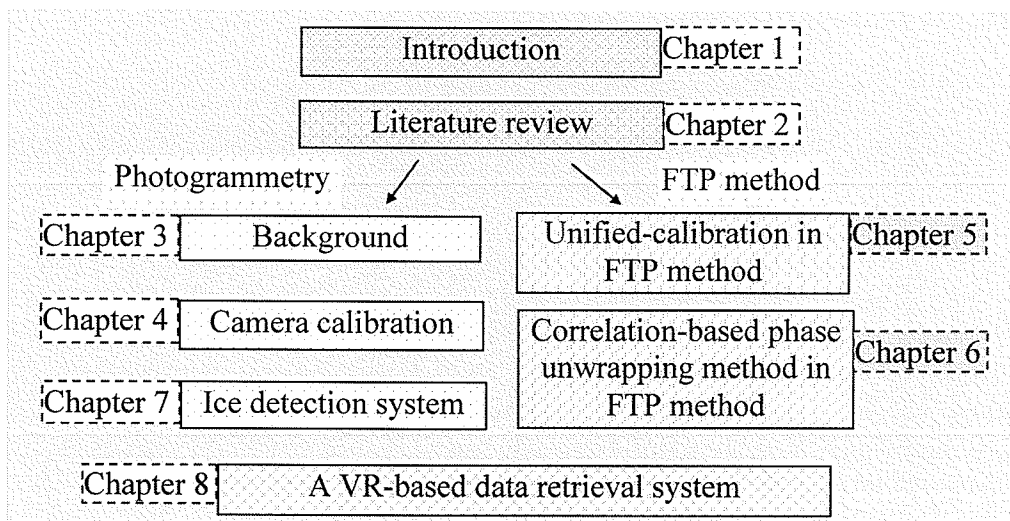


Figure 1.3 The structure of this dissertation

Chapter 2

Literature review

This chapter reviews literature in: (1) 3D data acquisition methods; (2) camera calibration; (3) system calibration for FTP methods; (4) phase unwrapping for FTP methods; (5) ice detection systems; and (6) VR-based data retrieval systems.

Before discussing the specific methods that are proposed, the general concepts and methods developed by others will be discussed in this chapter. Based on the literature review, problems of current methods are identified.

2.1 Review of 3D data acquisition methods

As it is shown in Figure 1.1 of Chapter 1, the details of 3D data acquisition methods are described as follows.

CMM uses a mechanical contact method to obtain 3D data of an object. It is precise but the equipment is expensive. CMM is limited by mechanical problems in object size, measurement volume and materials used (Peng and Loftus, 2000). For example, it cannot be used to measure fragile objects or objects with a soft surface. CMM's speed of measurement is also slow.

CT is a transmissive approach to acquire 3D data (Isdale, 1998). It scans an object using high energy X-Ray and measures the amount of radiation that passes through the object along various lines of sight. After a back projection or Fourier projection slice reconstruction, the 3D data can be obtained. It is insensitive to the reflective properties of the surface of objects

and can capture the internal cavities of an object that are not visible from the outside. But the system is generally very expensive and needs a large space for installation. In addition, the accuracy is degraded if there is a large variation in material densities, such as wood glued to steel.

The radar method is based on the propagation and reflection of high frequency electromagnetic waves (Grégoire *et al*, 2003). In this method, the 3D information of an object is obtained by measuring the time required for a pulse of sound or microwave energy to bounce back from the object. Amplitude or frequency-modulated continuous energy waves can also be used in conjunction with phase or frequency shift detectors. The radar method is suitable for measuring large objects at a long distance; but the method fails in measuring small objects at a short distance because the time-of-flight can only be detected in femtosecond (10^{-12} second) range. That is about at least tens of meters.

The laser scanner has been an accurate tool for building 3D models of an object. There are four methods that use laser to acquire 3D data of an object (Chen *et al*, 2000). The first method is Time/Light in Flight. It is based on the direct measurement of the time of flight of a laser pulse. A laser pulse is reflected back to the receiving sensor by the object and a reference laser pulse is passed through an optical fibre and received by the sensor, the time difference between the two pulses being converted to distance. The second method is the point laser triangulation. The principle of point laser triangulation is given in Figure 2.1 (Stojanovic *et al*, 2002). A laser beam is focused on the object surface producing light spot S. Spot S is focused at S' on the image plane. The height between spot S and a reference plane is h . The angle between the laser beam and the lens center O is θ . The distance between spot S' and the reference plane is dx on the image plane. From the geometry, $h = dx / A * \sin(\theta)$.

Where $A = OO'/O'O''$. The third method is the laser speckle pattern sectioning. Laser radar 3D imaging, also known as speckle pattern sampling, is a 2D slice of the object's 3D Fourier transform. Two or more 2D slices of object's 3D transform are taken using a CCD (charged couple device) array at each different laser wavelength, and the individual frames are added up to generate a 3D data array. A 3D Fourier transform is applied to this data array to obtain the 3D shape of an object. The fourth method is the laser tracking system. Differing from mechanical, electromagnetic or ultrasonic trackers, the laser tracker uses an interferometer to measure distance, and two high- accuracy angle encoders determine vertical and horizontal angles. However, the processing is slow using a laser beam to capture 3D data because the surface has to be scanned line-by-line. The system is expensive and the high-energy laser beam needs to be treated with care (Peng and Loftus, 2000).

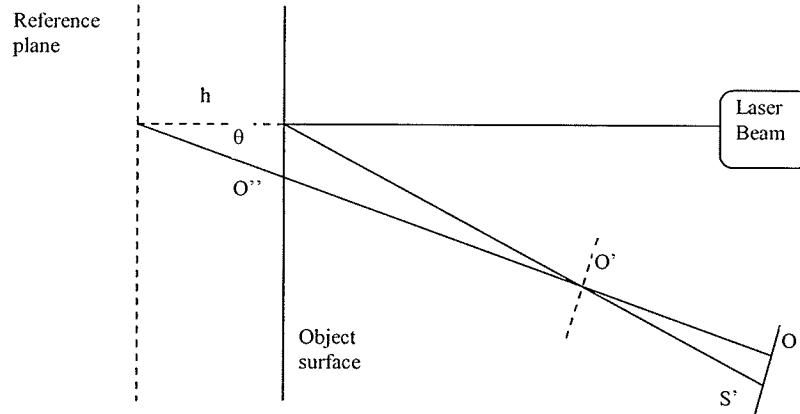


Figure 2.1 Laser scanner

In Moiré methods there are two gratings, one is a master grating and the other is a reference grating, from which contour fringes can be generated and resolved by a CCD camera. Using the contour fringes the 3D shape of an object can be obtained (Chen *et al*, 2000). Moiré methods have phase discrimination problems when the surface is not smooth. This problem

means that Moiré methods cannot avoid errors when the slope of the surface is greater than a limitation. It is also to be noted that the Moire method's system structure and algorithm is complex.

In photogrammetry methods, two or more images have to be acquired by either two cameras at the same time or by one camera at different times. Then image coordinates of any feature points in the two images can be measured. Using the image coordinates of these points, the 3D coordinates of the feature points can be calculated, and the whole 3D object can be reconstructed. This method can be used for multiple images. There are two photogrammetry methods: (1) the calibration-based model construction (Zhang, 2000; Qurban and Sohaib, 2001), and (2) the calibration-free model construction (Achour and Benkhelif, 2001; Pollefeys *et al*, 2000). A calibration pattern is needed to calculate the camera position for 3D model reconstruction in the first method. But the camera position will be calculated by using correspondent points with the calibration pattern in the second method.

The key to the photogrammetry methods is the correspondence problem: that is, to determine the point in one image that corresponds to a give point in the other image. Generally, it is hard to solve the correspondence problem on a smooth surface. It is necessary to project some additional signs onto the object surface to find correspondence points on all captured images. So far, there are many strategies to project different structured lighting patterns onto the object to recover the 3D shape of an object (Salvimas, 2001). The purpose of these strategies is to improve the accuracy of recovery and increase the flexibility of different techniques. These strategies have provided good solutions for 3D shape acquisition, but some drawbacks related to these techniques include: complicated patterns and algorithms in the processing of captured images, and the expense of forming an application (Isdale, 1998).

SFS is a method that can reconstruct the 3D shape of an object by the mapping between the shading and surface shape in terms of the reflectance function $I(x, y) = R(p, q)$, where $I(x, y)$ denotes image intensity, $p = zx$ and $q = zy$, z is the depth of the object and (x, y) are projected spatial coordinates of the 3D object (Dovgard and Basri, 2004). SFS methods can be divided into four groups: minimization approaches, propagation approaches, local approaches, and linear approaches (Zhang *et al*, 1999). The photometric stereo method is the multi-image version of SFS. Rather than using a single intensity image in the conventional SFS, the photometric stereo method uses two or more intensity images of the object under different illumination conditions, which improves the accuracy of the result. In the SFS method, the reflection model of an object's surface has to be assumed. However, real images of object's surface do not always follow the assumed model. Therefore the SFS method is somewhat inaccurate and is sensitive to noise.

In PMP methods, a fringe pattern is projected onto the object by varying the phase of the pattern. Three or more deformed fringe pattern images are captured by a CCD camera and the phase distribution of the object can be calculated by these images. The 3D shape of the object can then be recovered by mapping the phase distribution to the height (Quan *et al*, 2001). Many effective phase-measuring algorithms have been established (Li and Su, 2001).

In FTP methods (Su and Chen, 2001), a Ronchi grating or a sinusoidal grating is projected onto the object surface (Figure 2.2). The deformed grating image is captured by a CCD camera. 3D data of the object can be obtained by calculating the Fourier transformation of the image, filtering in spatial frequency domain and calculating the inverse Fourier transformation. FTP needs only one (or two) image(s) to do full field analysis but the result is not as accurate as SFS methods.

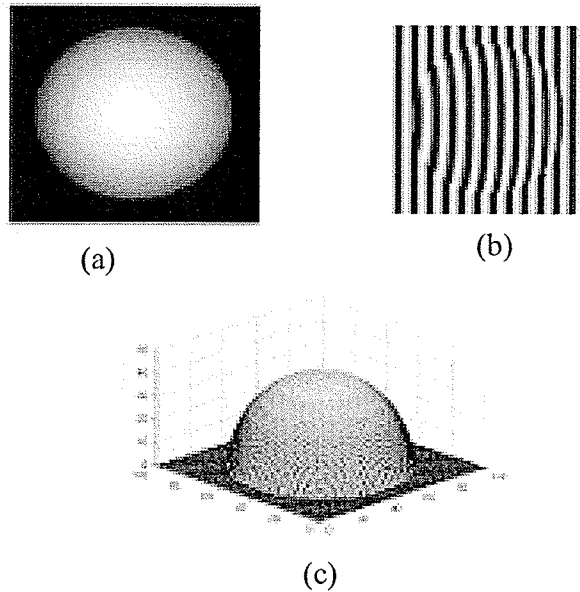


Figure 2.2 (a) An image without grating; (b) An image with deformed grating; (c) 3D plot of the reconstructed object.

2.2 Camera calibration

In camera calibration, two types of parameters have to be determined. These parameters include: (a) intrinsic parameters, such as the focal length, principle points and distortion, and (b) extrinsic parameters, such as rotation and translation between a camera coordinate system and the 3D world coordinate system. Two steps are needed to calibrate a camera. The first step is to establish the correspondences between image points in the image plane and points on the pattern in the world coordinate system as shown in Figure 2.3. This process is called feature extraction and matching. The coordinates of image points and pattern points are obtained in the process. The second step is to compute the intrinsic and extrinsic parameters using coordinates of image and pattern points by certain numerical methods.

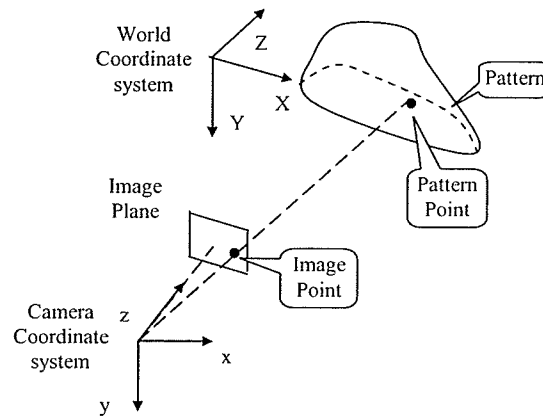


Figure 2.3 Geometry structure of a pattern and the image of the pattern

Use of calibration patterns to calibrate a camera is an accurate and reliable method of obtaining parameters (Shu *et al*, 2003). One of the most commonly used calibration patterns is an object with black squares on white background as shown in Figure 2.4 (a) (Heikkila and Silven, 1997; Tsai, 1987). The 3D coordinates of corners of those black squares must be known precisely to obtain an accurate calibration, but this is a costly pattern building procedure (Valkenburg, 1996). Recently, there is a trend to use planar patterns in camera calibration because the planar patterns provide an easy and inexpensive solution (Sturm and Maybank, 1999; Forbes *et al*, 2002). There are different techniques available for camera calibration using the planar calibration pattern, such as concentric conics (Yang *et al*, 2000), checkerboard (Figure 2.4(b)) (Zhang, 1999), 1D objects (points aligned on a line) (Zhang, 2004), vanishing line (Zhaoxue and Pengfei, 2004) and a pencil of lines passing through a circle (Meng *et al*, 2003); or using GA (Genetic Algorithms) (Bouchouicha *et al*, 2003) and neural networking (Jun and Kim, 1999).



(a) Calibration pattern with two orthogonal planes (b) Checkerboard calibration pattern

Figure 2.4 Two types of the calibration pattern

The existing methods mentioned above only focused on the second step of camera calibration; they ignored the features extraction and matching. The lack of robust feature extraction and matching prevents these methods from being used in practical applications. This research will focus on the first step of the camera calibration using a checkerboard pattern. An overview of automatic feature extraction and matching of the checkerboard pattern is described as follows.

The checkerboard pattern, as shown in Figure 2.4 (b) is one of the most commonly used planar calibration patterns. Its feature points are grid corners formed by all black or white squares, which can be easily detected (Shu *et al*, 2003). The process of locating feature points of the checkerboard pattern includes finding edges of the pattern, grouping the detected edges into quadrilaterals, and clustering the edges into rows and columns. The checkerboard pattern can then be found by topological filtering. The feature points can be found by intersecting lines (Cumani, 2002). But it is difficult to find the checkerboard pattern in a complicated background of images using this method.

"Attributed relational graph matching" was used by Soh (1997) and Matas (1997) for finding the checkerboard pattern in an image. A 3x3 mask of the Sobel operator is used for filtering

the raw image. It is then followed by an adaptive threshold based on a local gradient histogram analysis. The black squares are detected in the preceding steps. Each square is linked and gap bridging is applied wherever necessary. To segment the calibration chart and recover the position and orientation of all calibration points (i.e. centers of the squares), "Attributed relational graph matching" between the features extracted and the model is performed. Little detail was given in the papers and there is no method provided to get the coordinates of grid corners that is used in the camera calibration. The method fails when there are shadows on the checkerboard pattern because the Sobel operator is sensitive to high intensity point variations.

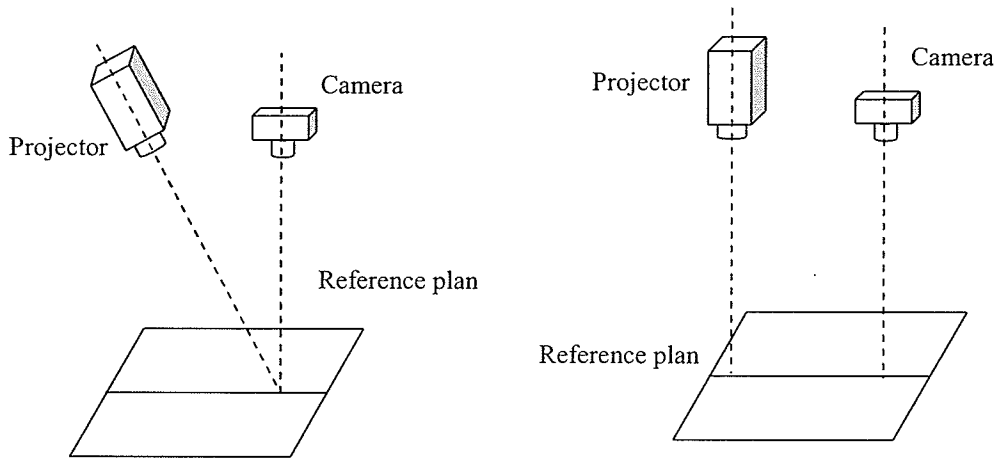
Delaunay triangulation was used by Shu (2003). The corner features are detected by a corner detector, and the corners are then connected using Delaunay triangulation. Pairs of neighbouring triangles are combined into quadrilaterals, which are then topologically filtered and ordered. A unique data structure is proposed in the paper for representing both triangular and quadrilateral meshes. This mesh structure allows users to exploit the strong topological constraints in a regular grid. The method is able to handle images with severe radial distortions. The problem with this method is that it supposes "the Delaunay triangulation will usually generate triangles by diagonalizing the tiles", which makes this method fail in complicated background environments.

The OpenCV (Open Computer Vision Library) function, `cvFindChessBoardCornerGuesses`, can find feature points of the checkerboard pattern in an image, but false detection occurs too often because the conditions required for corners selection are difficult to satisfy. There is a manual method to find grid corners of the checkerboard pattern in the software "Camera calibration toolbox for MATLAB " (Bouguet), but there is no document about the algorithm.

These methods are not reliable in unconstrained environments. In this research, a novel method for the feature extraction and matching of the checkerboard pattern in unconstrained environments is proposed.

2.3 System calibration for FTP methods

The FTP method was introduced by Takeda *et al* (Takeda and Mutoh, 1983). It has been greatly improved and studied by many researchers. The effectiveness of windowing to reduce errors in the FTP method is studied by Fiona *et al* (2004). The phase error caused by sampling the fringe patterns in the FTP method was studied by Chen *et al* (1999). A two-dimensional continuous wavelet (2D-CWT)-based filter is used to remove the background components and high frequency of fringe images (Gdeisat *et al*, 2006; Wang *et al*, 2004). A bi-color fringe pattern is used to improve the FTP method (Chen *et al*, 2004; Chen *et al*, 2006). A windowed Fourier transform is used to extract the zero spectrum of the deformed fringe image in the FTP method (Su *et al*, 2005). Two-dimensional Fourier transform profilometry (2D FTP) is applied in the FTP method to provide better height information extraction from noise when speckle-like structures and discontinuities exist in the fringe images (Lin and Su, 1995). An improved Fourier transform profilometry (IFTP) is presented by Li *et al* (1990), Yi and Huang (1997) and Li and Su (1990). Obtaining a 360 degree 3D shape of an object by using the FTP method is studied by Su *et al* (1997).



(a) Crossed-optical-axes geometry

(b) parallel-optical-axes geometry

Figure 2.5 Two geometries of the FTP method

The system calibration of an FTP system includes a height calibration (Z-axis) and a plane calibration (X-axis and Y-axis). The parameters consist of positions and orientations of the camera and projector, the internal parameters of the camera, and the reference plane location. In most cases, these parameters are difficult to measure directly. Therefore, a calibration procedure is needed in the FTP method to determine the parameters.

A comprehensive study of the system calibration was done by Chan *et al* (1994). The paper presents the system calibration for both crossed-optical-axes geometry and parallel-optical-axes geometry as shown in Figure 2.5.

A method using a virtual phase calibrating model plane as shown in Figure 2.6 for system calibration is presented by Zhang *et al* (2005). The plane (X-axis and Y-axis) calibration and height (Z-axis) calibration are studied respectively in the paper. The calibration methods need to collect at least two series of images. One is a pure fringe image series of a model plane produced by projecting a sinusoidal fringe pattern onto the model plane. The image

series provides the phase information of the model plane at a different location. The other is an image series of the model plane without the fringe pattern, which provides the relationship between the coordinates of feature points on the images and their 3D coordinates. The virtual phase calibration method needs only one image series, i.e. a pure fringe image series of the model plan. The calibration of the X-axis and Y-axis is performed by a least-square map function method, the calibration of the Z-axis is performed by a piecewise linear interpolation method.

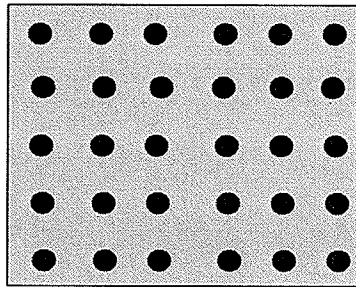


Figure 2.6 The calibrating model plane

An object with a known profile, shown in Figure 2.7 (a), is used to calibrate an FTP system by Sansoni *et al* (1994). First, the coarse approximation of the parameters of the system is measured. The object is then used to measure the parameters of the system. A calibration map is produced by evaluating the difference between the measured and the actual profile of the object. The height, calculated by the coarse approximation of the parameters of the system and its errors, is presented in the map for each calibration point. The approximation of the system parameters is adjusted based on the calibration map. This procedure is repeated until the required measurement accuracy is obtained.

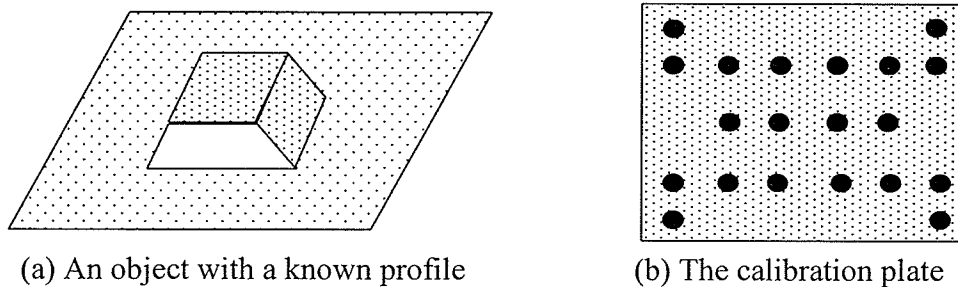


Figure 2.7 Calibration patterns

A calibration plate shown in Figure 2.7 (b) and a CMM are used by Hu *et al* (2003) to calibrate the system. The plate is made of aluminium and is machined by a CNC (Computer Numerical Control) milling machine. The surface is sprayed with white paint to improve its condition for measurement. The hole positions are calibrated by the CMM. A two-step approach is proposed in the research. The approximate values of the system parameters are measured at first. The calibration plate is then measured at different positions. The distances between various holes are calculated by three phase-shifted fringe patterns and a centerline pattern. The results are compared with the values obtained by the CMM. The measurement errors are used in an iterative algorithm to calculate the system parameters. The first step is important because it determines the approximate values of the parameters. Without these approximate values as initial values, the iterative algorithm may take an excessively long time and converge to wrong values.

A least-squares calibration approach was proposed by Guo *et al* (2005). A simple nonlinear function was proposed to represent the mapping relationship between the depth map and phase distribution. A series of images of a target plane at a sequence of positions with known depth is taken. The nonlinear function is used to measure the corresponding phase

distributions of the images. The phase distributions are used in a least-squares algorithm with a simple linear computation to calibrate the system.

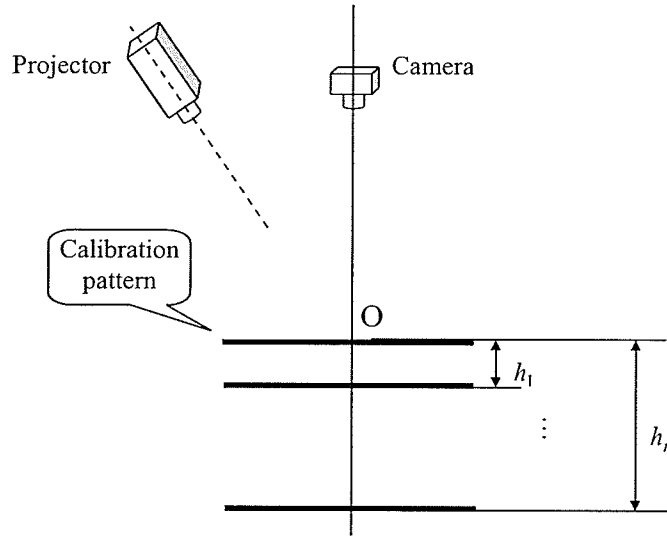


Figure 2.8 The layout of a system calibration

But these methods need a series of images of a calibration pattern and the calibration procedure is time-consuming. In this research, a unified calibration method for the FTP-based 3D data acquisition is proposed.

2.4 Phase unwrapping for FTP methods

Phase unwrapping is an essential process in the FTP method for the height calculation of an object. Because the phase map obtained by the FTP method is limited from π to $-\pi$; this is called a wrapped phase. The natural phase must be obtained by suitable unwrapping algorithms. Figure 2.9 shows a continuous 1D phase distribution and the same distribution when it is wrapped by 2π .

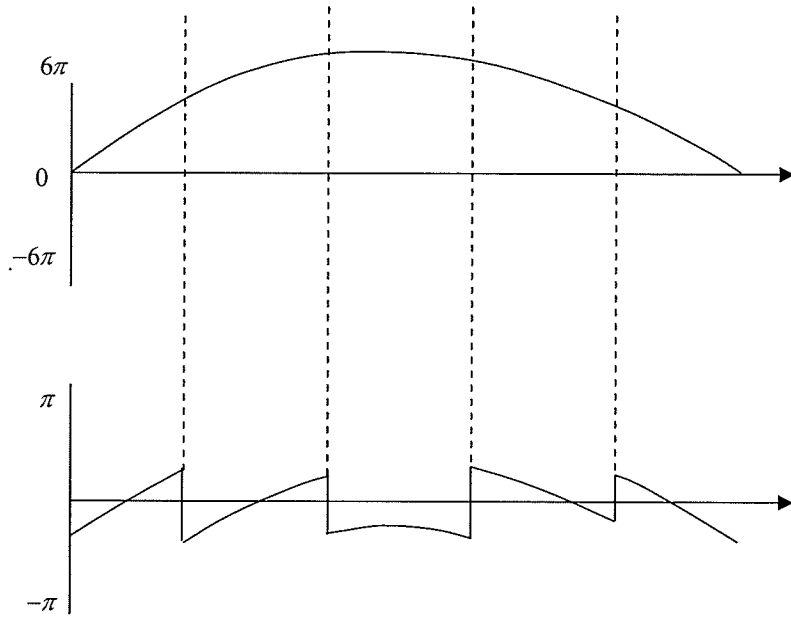


Figure 2.9 A 1D phase distribution and when it is wrapped by 2π

For a perfect wrapped phase distribution, the continuous natural phase can be obtained by comparing the wrapped phase in neighbouring pixels, and adding or subtracting multiples of 2π to obtain the real phase between the two pixels (Su and Xue, 2001). As the unwrapped phase is a cumulative function of the original wrapped phase, phase unwrapping should be path-independent. The natural phase should be single-valued. But in practice, irregular changes of object's surface may result in a shadow or excessive density or sparsity of the fringe distribution on the deformed fringe image. These factors may result in phase discontinuities, low modulation or regional undersampling of the fringe (Li and Su, 2002). It is impossible to obtain a correct natural phase in such areas (Su and Xue, 2001). Therefore phase unwrapping is path-dependent. As phase unwrapping is a cumulative process, an error at any given point can propagate along the unwrapping path. Choosing an optimized unwrapping path to avoid error accumulation has been addressed by some researchers.

Reviews of phase unwrapping algorithms were presented from the early 1990's (Andra *et al*, 1991; Judge and Bryanston-Cross, 1994; Su, 1996; Huntley and Coggrave, 1998). These algorithms can be classified into three categories (Herraez *et al*, 2002; Lu *et al*, 2005): global algorithms, region algorithms (Meneses *et al*, 2005), and path-following algorithms. The path-following algorithms can be further classified into three sections: path-dependent methods (Huang and Lai, 2002), residue-compensation methods, and quality-guided methods. Global algorithms are robust for noisy fringe images but time-consuming (Herraez *et al*, 2002). Region algorithms are not as robust as global algorithms but they are faster (Herraez *et al*, 2002). Path-dependent methods are fast but fail with noisy fringe images (Meneses *et al*, 2005). Residue-compensation algorithms are efficient at timely execution but not robust (Herraez *et al*, 2002). In quality-guided methods, a reliability map is used to identify the pixel's reliability of the wrapped phase. The pixel's reliability is used to guide the direction of phase unwrapping. The path of phase unwrapping is always along the optimized direction from the pixel with high reliability value to the pixel with low reliability value. Therefore, error is limited to local minimum areas even in the worst case. The quality-guided method has therefore attracted many researchers' attention to phase unwrapping methods (Herraez *et al*, 2002).

Su and Chen (2004) presented a review of quality-guided methods. The review shows that the modulation function is a very important parameter of reliability in phase unwrapping as the value of modulation in the areas of local shadow and abrupt discontinuities is lower than that of other parts. And low modulation means low phase reliability (Su *et al*, 1993). Modulation has been successfully used in research to produce an optimized reliability map for phase unwrapping, such as cross-amplitudes (Takeda and Abe, 1996), edge detection with

modulation (Li *et al*, 1997), and the fitting error with modulation (Li and Su, 2002). However, modulation calculating with the FTP method requires careful consideration.

In FTP methods, a filter window is required to calculate the modulation (Su and Chen, 2004). A small window can simplify phase unwrapping for the FTP method but it may decrease the precision of the 3D data by eliminating useful parts of the spectrum (Su and Xue, 2001). A big window can bring information of a higher order and zero frequency into the fundamental frequency, so that the wrong phase unwrapping is inevitable. Figure 2.10 is the 1D spatial frequency spectra of the image of a pure fringe pattern. There are no system errors (background noise) in the pure fringe pattern image: therefore there is only Q2 in the spatial frequency spectra. Q2 is the spectrum of the fundamental component (the grating frequency carrier). Figure 2.11 is the 1D spatial frequency spectra of the images of the pure fringe pattern projected on an object. There are some signals that were brought in by the experiment system and environments therefore there are Q1 and Q3 in the spatial frequency spectra except Q2. Q1 is the spectrum of background of the images and Q3 is the spectrum of all frequency that is higher than the fundamental component. The FTP method uses a window to remove Q1 and Q3 to calculate the modulation. If a big window is used then Q1 and Q3 are brought into the fundamental frequency. Modulation is calculated with noise. If a small window is used then a part of Q2 is removed from the fundamental frequency. The modulation is calculated but useful parts of the frequency are lost. Therefore, the width of the window should be chosen carefully based on the shape and surface of the measured object. It will take some time to obtain a proper width. A correlation-based phase unwrapping method is proposed in this research to avoid choosing the width of the filter window for phase unwrapping in FTP methods.

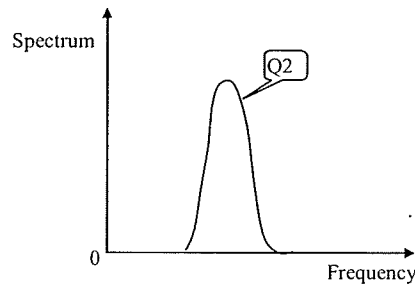


Figure 2.10 The 1D spatial frequency spectra of a pure fringe pattern

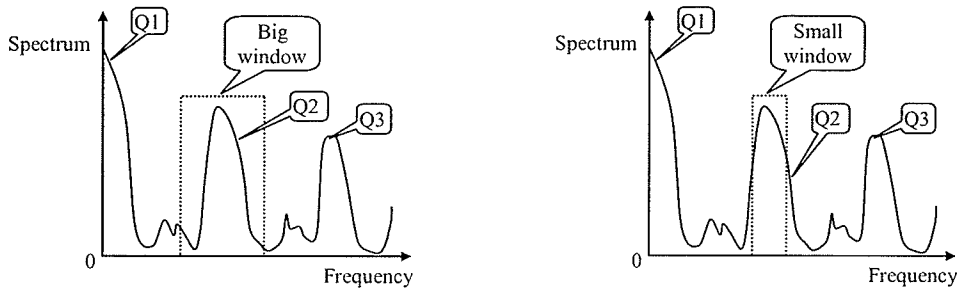


Figure 2.11 The 1D spatial frequency spectra of a fringe pattern with noise and objects

2.5 Ice detection systems

Most of the damage on overhead power transmission lines that cause towers to collapse is due to ice accumulation on power transmission lines (Savadjiev and Farzaneh, 2004). Canada is one of the countries in which power transmission lines suffer severe icing problems. For example, the 1998 ice storm caused severe damage to Hydro-Québec's power transmission system. Therefore the ice accumulation detection methods have drawn a lot of attention in Canada.

A common ice detector is the icing-rate meter (IRM). It is an instrument that detects and measures the icing potential of the air in contact with a probe. When the IRM is installed near a power transmission line, the real-time data on icing rates and the total accumulated weight on a specific line component can be provided. The operator can then assess the risks of

overloads of power transmission lines. Therefore it gives the operator time to reduce potential damage on the power transmission systems. It is a very versatile device that can measure all types of atmospheric icing, whether caused by the passage of cold clouds or by freezing precipitation such as freezing rain or wet snow. Unfortunately, the IRM is unable to differentiate between hoarfrost and ice, or to detect accurately ice thickness on conductors, and it is costly. The problem is that the detection device is on its sensing probe, not directly on power transmission lines.

An image-based method for measuring ice accumulation on power transmission lines was developed by Borkowski (2002). The proposed method combines two methods in a non-standard way. One is the δ -mesh method and the other one is the Gouraud shading algorithm. The disadvantages of the method are: (1) As the vibration of power transmission lines in real environments was not considered in the method, accurate ice thickness cannot be obtained by this method; (2) the method does not automatically detect the edges of ice; and (3) the input image for the method can only contain one power transmission line with uniform sky in the background, therefore it fails to detect ice on power transmission lines with complex backgrounds.

In this research, a novel image-based 3D ice thickness acquisition algorithm is proposed. The major problem involved in 3D ice thickness calculation is to find corresponding points in two ice images. The general process of finding the corresponding points in two images includes two steps. The first step is feature extraction, and the second step is point matching.

Feature extraction refers to methods that aim at determining the location and orientation of image features in an image. The resulting features are subsets of the image. Many feature detection algorithms can be found in literature. A template-based method was proposed by

Luo *et al* (1998). The corners are considered to be located at the saddle points of the magnitude of the vector potential. The junctions of the edge and symmetry lines are corners. An isolated point detection method was described by Gonzalez and Woods (2002). The rate of change of gradient direction and the gradient magnitude are used to detect corner points. Zheng *et al* (1999) proposed a gradient-direction corner detection method based on the Plessey corner detection method. A neural network was used to detect corners by Basak and Mahata (2000). Pei and Ding (2005) proposed a new corner detection method. The sum of the differences is used to observe the variations along the adaptive vertical and tangent axes. The variations are classified into 36 types and a 'case table' is used to detect the corners. The gradients calculated along x and y -axes, used in many existing algorithms, are not needed in this method. The Gabor wavelet was used by Gao *et al* (2004) to detect corners. The input image is transformed to several wavelet scales and along several directions. The magnitude along the direction that is orthogonal to the gradient orientation is used for the corner measurement. A support vector machine-based algorithm for corner detection was presented by Banerjee *et al* (2004). A four dimensional feature vector is used to store the direction of maximum gray-level change for each edge. A support vector machine is designed using feature vectors to detect the corner points. Wavelet transform was used to detect corners by Lee *et al* (1995) and Penersini *et al* (2000).

An overview on edge detection methods was described by Ziou and Tabbone (1998). The first-order derivatives are used in Roberts Cross, Prewitt, Sobel and Canny methods (Heath *et al*, 1997). The second-order derivatives are used in the directed second-order derivative method and the Laplacian zero-crossing detection method (Gonzalez and Woods, 2002). The comparison of these methods was discussed by Heath *et al* (1997). The conclusion is that

there are no significant differences between the performances of these methods, therefore the choice of the edge detection algorithm depends on the applications.

A blob detector is used to detect regions in an image. The blob detectors are roughly grouped into four categories (Hinz, 2005): (1) Matched filters / template matching; (2) Watershed detection; (3) Structure tensor analysis followed by hypothesis testing of gradient directions; and (4) The region detection through a scale-space analysis. From a theoretical point of view, the region detection through the scale-space analysis is the most advanced one (Hinz, 2005), and it is often carried out through the computation of local extremes of some normalized derivatives of linear scale-space image representation (Damerval and Meignen, 2007).

Corresponding point matching is performed by calculating the similarity of two image points. The algorithms of similarity measurement are divided into two categories: area-based matching and feature-based matching (Li and He, 2002).

Computing correlation (Vincent and Laganier, 2002) and sum of squared differences (SSD) (Kanade and Okutomi, 1994) are the basic techniques for obtaining the correspondence between two or more images. The main problem of the techniques is the size selection of an appropriate window. The window size should be large enough to include enough information of intensity variation, but small enough to avoid the effects of projective distortion.

An adaptive window method was proposed by Kanade and Okutomi (1994) to select an appropriate window by evaluating the local variation of intensity and disparity. A statistical model of the disparity distribution within the window is created. An edge detection-based adaptive window method was proposed by Wang (2004). The window is chosen by the intensity variance without the influence of disparities; therefore the method is robust for variation of intensity. A new color area-based matching approach based on self-organization

neural networks was proposed by Hua *et al* (2004). The color information is used for calculating color features similarities. The neural networks are used to obtain the correspondence of images.

Using features instead of the intensities allows a representation which is more invariant with respect to distortions by illumination, reflectance or geometry. This makes feature-based algorithms more robust than area-based matching. An algorithm based on a multi-resolution, multiple-hypothesis scheme was designed by Cham and Cipolla (1998). The core of the algorithm is a Bayesian framework for incorporating similarity measurement of feature correspondences in regression. A novel neural network architecture was proposed by Branca *et al* (1998) to solve the correspondence problem. A nonlinear relaxation labelling approach is used to estimate correct matches from high order compatibility measurements. And the cross-ratio similarities are used as constraints to determine compatibilities between feature matches. Feature locality and the gray-level gradient associated with the feature were used by Candocia and Adjouadi (1998) to measure the similarity of features. Local and global matching strategies are integrated in a matching procedure to ensure that the features are matched with a high degree of similarity. The parallel of epipolar lines were used by Lu and Manduchi (2004) as a constraint for feature matching. The algorithm reduces the mismatches and the dimension of search domain.

The preceding research all focus on a general solution of feature detection and feature matching in image processing. None of them has been used to monitor the ice accumulation in real environments. In this research, the proposed method will combine the existing methods in a practical way to provide a useful solution to find the corresponding points in two ice images.

2.6 Product data retrieval systems

Concurrent engineering (CE) is a key technique to improve the performance of companies in the integration of people, tools, information and processes working together efficiently. In CE, people may work at different corporations or different disciplines of a company. The collaboration is the fundamental element in this situation (Salomone, 1995). It is very important for the right people to get the right information at the right time. Different members on a team may use different software and hardware systems. It is important for product information to be accessible conveniently and to be managed effectively.

The most recent work on product data retrieval is on XML (eXtensible Markup Language) - based data exchange format. The XML-based data exchange facilitates the information integration and interoperability of teamwork because XML can provide a well-understood syntax and Web-friendly application for data exchange (Amstel *et al*, 2000; Burkett, 2001).

Another method is the STEP (Standard for The Exchange of Product model data)-based information integration (Yang and Pei, 1999). There are also a lot of systems that use the Internet to support information flow (Huang *et al*, 2000; Yang and Jiang, 2002; Shen and Wang, 2003).

These systems all focus on the smoothness of the information flow among members of a team but rarely consider a user-friendly searching interface to let members find information effectively. Some rigid interface methods, such as table-based or schematic queries, have been used in information systems (Santos *et al*, 2000). Using interfaces of these systems, the information, such as component's ID and component's name, should be typed in by users to search the product information. All menu or process flows of an application have to be memorized by users. It is difficult for new users to search information in these systems. On

the other hand, the product information usually has a hierarchical structure. These systems cannot provide users with an overview of hierarchy information, nor does it allow users to visualize a specific node within the whole context. Therefore, it is necessary to have a user-friendly search system to view product information.

So far, several 3D interfaces for database access have been proposed, such as Warehouse Metaphor (Massari *et al*, 1997), Keywords, Visual Query Language and Hypercube (Soetebier *et al*, 1999). In these 3D searching systems, Cubes or cones are used to represent a product hierarchy structure. And the 3D model is helpful to search product information. But they cannot provide users an immersive environment for product data retrieval. In this research, a VR-based user-friendly interface is proposed. It can provide users with a good understanding of the product hierarchy or product function. Therefore it enables users to get an overview of the product data structure and to find relevant information rapidly.

Chapter 3

Calibration-based 3D data acquisition

This chapter presents theories and concepts related to this research. A brief introduction to 3D data acquisition from two 2D images is presented. A camera model and calibration parameters are discussed along with the fundamentals of epipolar and homography. Image processing methods on feature detection and matching are also presented in this chapter.

3.1 A brief introduction on calibration-based 3D data acquisition

One kind of Photogrammetry employs the calibration-based 3D data acquisition method. A calibration object with known geometry is used to calibrate a camera for obtaining the intrinsic and extrinsic parameters accurately. The accurate 3D information of objects can then be obtained. A general process of the method is shown in Figure 3.1. The process is explained as follows:

(1) Camera calibration is an essential step in the method (Meng *et al*, 2003). Two types of parameters associated with a camera have to be determined in camera calibration: these include intrinsic parameters, such as focal length, principle points and aspect ratio; and extrinsic parameters, such as rotation and translation between a camera frame and a 3D world frame.

(2) Image acquisition is a procedure of capturing digital images by one or several calibrated cameras. Obtained image data are 2D images. The pixel values in the images typically indicate the light intensity on an object or scene. Pre-processing ensures that the images satisfy the requirements of the further operations. The pre-processing includes the following work:

- Size and color modification of the image to assure that the image meets the requirement for further processing.
- Noise reduction for the quality of images.
- Contrast enhancement for easily detecting information in the processing.

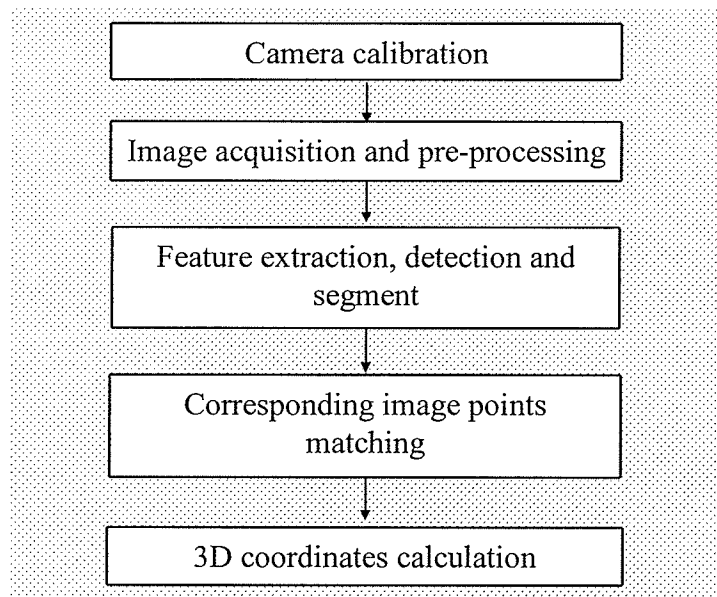


Figure 3.1 An overview of the process of the calibration-based 3D data acquisition

(3) Feature extraction obtains features of the image. The feature definition depends on the type of application. For example, in the 3D ice shape calculation, the iced power transmission line can be defined as a feature. Or the edges of the iced power transmission

line can be defined as a feature. Generally, the image features can be divided into 3 groups: points (corners), lines (edges) and regions (blobs).

(4) Corresponding image points matching finds a point of an object in different images using the similarity measurement. A pair of corresponding image points is shown in Figure 3.2. There is an object point in the world coordinate system. The projected points in both images (left and right) are the corresponding image points.

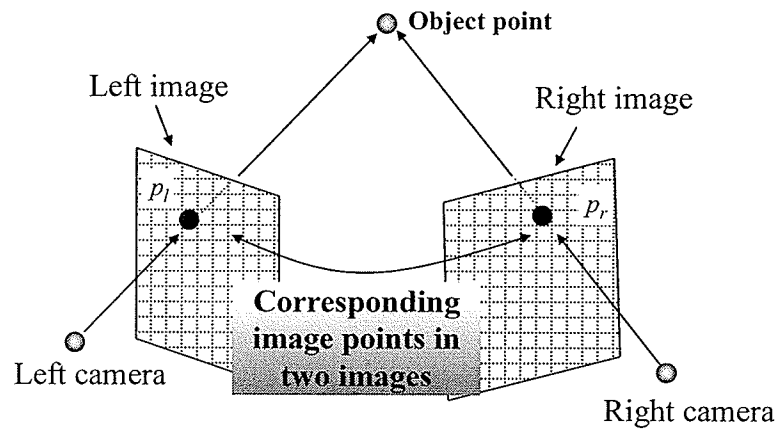


Figure 3.2 An example of a pair of corresponding image points

(5) 3D coordinates calculation is the final process of 3D data acquisition. The 3D coordinates of objects can be obtained through a triangulation algorithm from these corresponding image points.

3.2 Camera model

A camera is composed of a set of lenses used to convert light into an image as shown in Figure 3.3. The figure shows the lighting from an illumination source being reflected from an object to the camera. The camera collects the incoming lighting and records it onto an image

plane. The image plane is composed of an array of sensors. The sensor array converts lighting into a digital image. A complete description of the functioning of lenses will not be discussed here. A simple model of the camera, a pinhole model, is described and will be used in this research.

In the pinhole model, the lenses system of the camera is simplified to a hole with size zero in Figure 3.4. Rays are forced to pass through the hole. The hole is called the optical center. If a point P has coordinates $P = [X, Y, Z]$ relative to a reference coordinates system centered at the optical center o , with its z-axis being the optical axis of the camera, then the relationship of the coordinates of P and its image point $p(x, y)$ can be obtained from similar triangles in Figure 3.4 .

$$x = -\frac{fX}{Z}, \quad y = -\frac{fY}{Z} \quad (3.1)$$

Where f is the focal length.

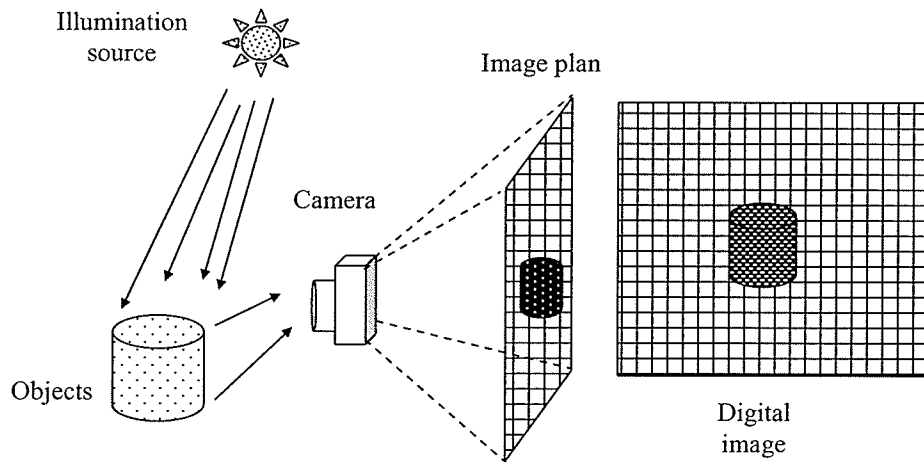


Figure 3.3 Digital image formation

There are two negative signs in Equation (3.1), which makes the object image to appear with upside down on the image plane as shown in Figure 3.4. To eliminate this effect, the image plane can be placed in front of the optical center o in Figure 3.5. Therefore $z = -f$ instead of $z = +f$. In this case, the coordinates of the image points p (x, y) is given by:

$$x = \frac{fX}{Z}, y = \frac{fY}{Z} \quad (3.2)$$

This pinhole model is used in this research.

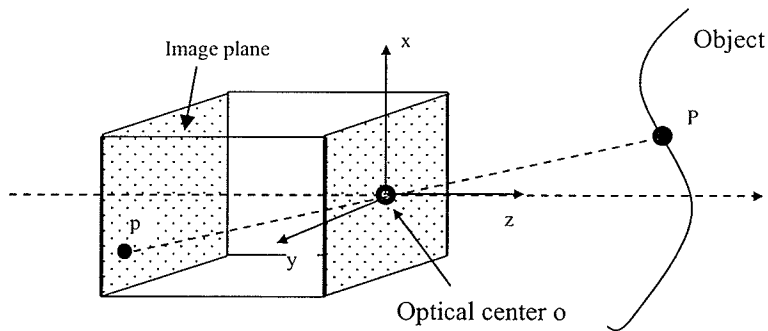


Figure 3.4 A pinhole model with the optical center in front of the image plane

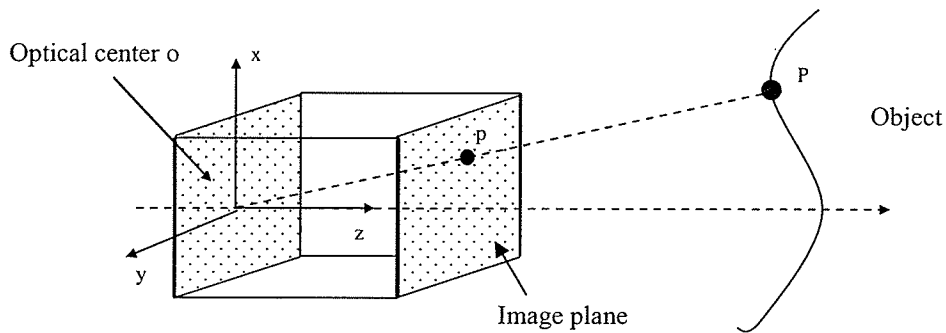


Figure 3.5 A pinhole model with the image plane in front of the optical center

3.3 2D images

Figure 3.6 shows a digital image which is a representation of a 2D image as a finite set of digital values, called pixels. Typically, the pixels are stored in the computer memory as a 2D array of integers. The greyscale digital images are used in this research. A greyscale image is typically composed of shades of gray, varying from black at the weakest intensity to white at the strongest. It is denoted by two-dimensional functions of the form $f(x,y)$, where (x,y) is the coordinates of one pixel. The values of the coordinates (x,y) are discrete quantities. Assume that an image $f(x,y)$ has M rows and N columns. The value of the coordinates at the origin is $(x,y) = (0,0)$. The maximum value of the coordinates is $(x,y) = (M,N)$.

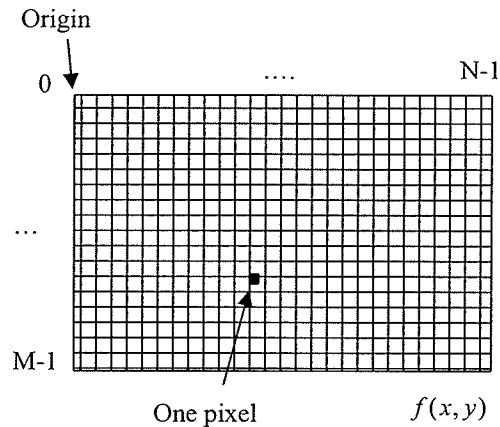


Figure 3.6 A digital image in 2D array format

The matrix form of the image $f(x,y)$ can be expressed in the following form:

$$f(x,y) = \begin{bmatrix} f(0,0) & f(0,1) & \dots & f(0,N-1) \\ f(1,0) & f(1,1) & \dots & f(1,N-1) \\ \dots & \dots & \dots & \dots \\ f(M-1,0) & f(M-1,1) & \dots & f(M-1,N-1) \end{bmatrix} \quad (3.3)$$

The right side of this equation is a greyscale digital image. Each element of the matrix array is one pixel. The term image will be used throughout the rest of this research to denote a greyscale digital image.

3.4 Image pre-processing

An image may be subject to noise. The noise may be generated from several sources, such as electrical sensor noise, photographic grain noise, and channel errors. These noises should be reduced before doing any further operations. The classical solution for reducing noises uses filtering techniques.

Image noise arising from sensor noise, photographic grain noise or channel errors usually appears as discrete isolated pixel variations that are not spatially correlated. Pixels that are in error often appear visually to be markedly different from their neighbours. Therefore noises in an image generally have a higher-spatial-frequency spectrum than the normal image components. Low-pass filtering can be effective for noise reduction. There are two types of low-pass filter, one is spatial filter and the other one is frequency domain filter. In this research, spatial filtering methods will be used because the filtering operations in the methods are performed directly on the pixels of the images and the methods are easy to be implemented.

The mechanics of spatial filtering are shown in Figure 3.7. The process consists of moving the filter mask from upper-left to lower-right in an image. At each point (x, y) , the response of the filter at each point of the image is calculated using a predefined algorithm. The algorithms include linear spatial filtering and nonlinear spatial filtering. In this research, the linear spatial filtering is used. For linear spatial filtering, the result of filtering is given by a

sum of products of the filter coefficients and the corresponding image pixels in the area spanned by the filter mask. In general, linear spatial filtering of an image f of size $M \times N$ with a filter mask m of size $m \times n$ given by the following equation (Gonzalez and Woods, 2002):

$$R(x, y) = \sum_{s=-a}^a \sum_{t=-b}^b m(s, t) f(x + s, y + t) \quad (3.4)$$

where, $a = (m - 1) / 2$ and $b = (n - 1) / 2$.

For example, for a 3×3 filter mask $m(3,3)$, the result of the linear filtering with the filter mask at a point (x, y) in the image $f(x, y)$ is:

$$R = m(-1, -1) f(x - 1, y - 1) + m(-1, 0) f(x - 1, y) + \dots + m(0, 0) f(x, y) + \dots + m(1, 0) f(x + 1, y) + m(1, 1) f(x + 1, y + 1) \quad (3.5)$$

Note that the coefficient $m(0,0)$ coincides with image value $f(x, y)$, indicating that the mask is centered at (x, y) when the computation of the sum of products takes place.

The process of linear spatial filtering given in Equation (3.5) is similar to a frequency domain concept called convolution. Therefore the linear spatial filtering is referred to as “convolving a mask with an image” (Gonzalez and Woods, 2002).

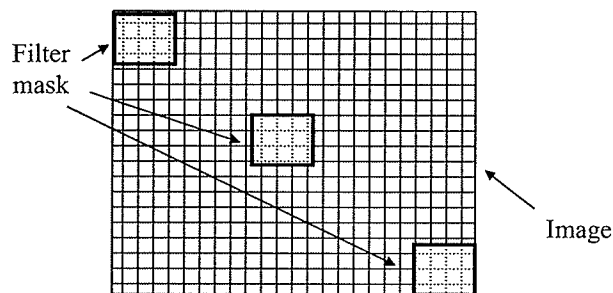


Figure 3.7 The process of spatial filtering

Equation (3.6) shows one 3×3 linear spatial filter which is used in this research. Use of the filter yields the standard average of the pixels under the filter mask. The “sharp” transitions in gray levels can be reduced in an image by replacing the value of every pixel in the image by the average of the gray levels of the neighbour pixels. Therefore the noise can be reduced.

$$m(x, y) = \frac{1}{9} \begin{pmatrix} 1 & 1 & 1 \\ 1 & 1 & 1 \\ 1 & 1 & 1 \end{pmatrix} \quad (3.6)$$

3.5 Feature extraction

3.5.1 Point detection

A mask shown in Figure 3.8 is used to detect the isolated points in an image. The process of the point detection is as same as the process of image filtering. The mask is moved through the image to compute the sum of products of the mask coefficients and the corresponding image pixels in the area spanned by the mask. If the value of the sum is greater than a threshold then a point is detected at the location.

-1	-1	-1
-1	8	-1
-1	-1	-1

Figure 3.8 The mask for point detection

3.5.2 Edge detection

Pixels in an image where brightness changes particularly sharply are often the locations of edges. Differential detection is a generic approach to detect edges in the image. There are two major classes of the differential detection: first- and second-order derivative. For the first-

order class, a spatial first-order differentiation is performed, and the resulting gradient is compared to a threshold value. The edges are detected if the gradient exceeds the threshold. For the second-order derivative class, the edges are decided if there is a significant spatial change in the polarity of the second derivative. In general, the detection of zero-crossings in the second derivative is used to capture significant spatial change. The second-order derivative methods are good at noise reduction. However, there are two drawbacks that prevent the method from practical applications. One is so-called spaghetti effect. The spaghetti effect tends to create closed loops of edges on an image. The other one is that the method smoothes the shape too much; for example, sharp corners are lost. (Gonzalez and Woods, 2002). For these reasons, the first-order method is used in this research.

First-order derivatives of a digital image are based on the generation of gradients in two orthogonal directions of an image. The gradient of an image $f(x,y)$ at location (x,y) is defined as the vector (Gonzalez and Woods, 2002):

$$\nabla f = \begin{bmatrix} G_x \\ G_y \end{bmatrix} = \begin{bmatrix} \frac{\partial f}{\partial x} \\ \frac{\partial f}{\partial y} \end{bmatrix} \quad (3.7)$$

where G_x is the gradient along x-axis, and G_y is the gradient along y-axis.

In an image, the gradient vector points in the direction of maximum rate of change of f at coordinates (x,y) . The magnitude of the gradient vector gives the maximum rate of increase of $f(x,y)$ per unit distance in the direction of the magnitude, it is used for feature detection. It is defined by (Gonzalez and Woods, 2002):

$$\nabla f = mag(\nabla f) = \left[G_x^2 + G_y^2 \right]^{\frac{1}{2}} \quad (3.8)$$

The magnitude of the gradient vector is also called the gradient in this research if there is no confusion. The direction of the gradient vector is an important quantity for feature detection. It is defined by (Gonzalez and Woods, 2002):

$$\alpha(x, y) = \tan^{-1}\left(\frac{G_y}{G_x}\right) \quad (3.9)$$

where $\alpha(x, y)$ represents the direction angle of the vector ∇f at (x, y) . The angle is measured with respect to the x -axis.

The simplest method of discrete gradient calculation is to calculate the difference of pixels along rows and columns of an image. The x -axis gradient is defined as (Gonzalez and Woods, 2002):

$$G_x(x, y) = f(x+1, y) - f(x, y) \quad (3.10)$$

and the y -axis gradient is defined as (Gonzalez and Woods, 2002):

$$G_y(x, y) = f(x, y+1) - f(x, y) \quad (3.11)$$

These definitions of x and y -axis gradients are chosen such that G_x and G_y are positive for an edge that increases in amplitude from left to right and from bottom to top of the image. These definitions are called Roberts cross and can be implemented by using a mask shown in Figure 3.9.

-1	0		0	-1
0	1		1	0

Figure 3.9 Roberts cross

Masks of size 2×2 are difficult to implement because they do not have a clear center. Therefore masks of size 3×3 are the most common in practice. Figures 3.10 and 3.11 show two examples of masks of size 3×3 , the Sobel mask and the Prewitt mask (Prett, 200).

-1	-1	-1
0	0	0
1	1	1

-1	0	1
-1	0	1
-1	0	1

0	1	1
-1	0	1
-1	-1	0

-1	-1	0
-1	0	1
0	1	1

Figure 3.10 Prewitt mask

-1	-2	-1
0	0	0
1	2	1

-1	0	1
-2	0	2
-1	0	1

0	1	2
-1	0	1
-2	-1	0

-2	-1	0
-1	0	1
0	1	2

Figure 3.11 Sobel mask

The Sobel mask differs from the Prewitt mask in that the values of the north, south, east, and west pixels are doubled. The motivation for this weighting is to give equal importance to each pixel in terms of its contribution to the spatial gradient. The Sobel mask has slightly superior noise-suppression characteristics (Prett, 2000).

The masks discussed above are used to obtain the gradient components G_x and G_y . To avoid computing squares and squares root in Equation (3.8), an approach used frequently is to approximate the gradient by absolute values (Gonzalez and Woods, 2002) :

$$\nabla f = |G_x| + |G_y| \quad (3.12)$$

A point on an edge will be detected at the location where the gradient is greater than a threshold.

3.6 Feature matching by correlation

One of the most fundamental factors of feature matching in image processing is correlation (Gonzalez and Woods, 2002). Using correlation methods, a feature of interest is compared to

all unknown features in an image. If the correlation between an unknown feature and the feature of interest is greater than a threshold, the unknown feature is labelled as the matched feature.

The correlation method is used to measure the squared Euclidean distance $d_{f,w}^2(u, v)$ between a sub-image $w(x, y)$ and an image $f(x, y)$. The sub-image is a part of an image containing the feature of interest. The image contains all unknown features.

$$d_{f,w}^2(u, v) = \sum_{x,y} [f(x, y) - w(x+u, y+v)]^2 \quad (3.13)$$

Where (u, v) is the size of $w(x, y)$.

In the expansion of $d_{f,w}^2(u, v)$,

$$d_{f,w}^2(u, v) = \sum_{x,y} [f^2(x, y) - 2f(x, y)w(x+u, y+v) + w^2(x+u, y+v)] \quad (3.14)$$

The term $w^2(x+u, y+v)$ represents a summation of the template energy. It is a constant and is independent of the coordinate. The image energy over the window area is represented by the first term $f^2(x, y)$. It generally varies slowly over the image field. The second term $w^2(x+u, y+v)$ is recognized as the correlation between the image and the sub-image. At the coordinate location of the sub-image match, the correlation $c(x, y)$ should become large to yield a small difference.

$$c(x, y) = \sum_{x,y} f(x, y)w(x+u, y+v) \quad (3.15)$$

Therefore, the correlation is a measure of the similarity between the sub-image and the image. But the correlation function given in Equation (3.15) has the disadvantage of being sensitive to changes in the amplitude of $f(x, y)$ and $w(x, y)$. For example, increasing values of $f(x, y)$ will

increase the value of $c(x,y)$. This disadvantage can be avoided by performing matching via the normalized cross-correlation, which is defined as (Gonzalez and Woods, 2002) :

$$r(u,v) = \frac{\sum_x \sum_y [f(x,y) - \bar{f}(x,y)][w(x+u,y+v) - \bar{w}]}{\left\{ \sum_x \sum_y [f(x,y) - \bar{f}(x,y)]^2 \sum_x \sum_y [w(x+u,y+v) - \bar{w}]^2 \right\}^{\frac{1}{2}}} \quad (3.16)$$

Figure 3.12 shows a simple example of the correlation-matching process. The objective is to find matches of a sub-image $w(x, y)$ of size $J \times K$ within an image $f(x, y)$ of size $M \times N$, where $J \leq M$ and $K \leq N$. The origin of $f(x, y)$ is at top left corner, the origin of $w(x, y)$ is at its center. For one position (x_0, y_0) inside $f(x, y)$, the application of Equation (3.16) yields one value of $c(x, y)$. As $w(x, y)$ is moved around the image area, x and y are varied, therefore $c(x, y)$ are obtained. The highest value of $c(x, y)$ is in the position where the best match between $f(x, y)$ and $w(x, y)$ is found.

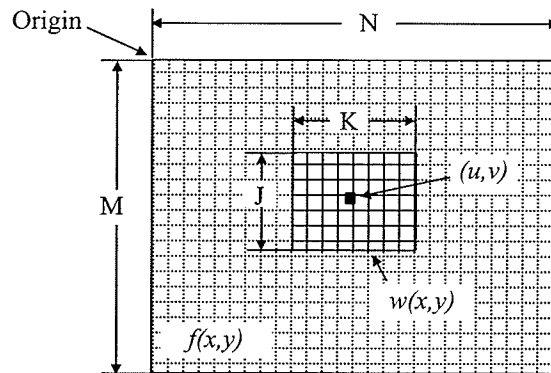


Figure 3.12 The correlation-matching process

3.7 The intrinsic and extrinsic parameters of a camera

The following sections are entirely about the overview of projective geometry and geometry of 3D vision systems used throughout the research.

As mentioned in Section 3.1, the pinhole model of a camera is used in this research. There exists a relationship which maps the projective space to the camera's image plan: $P^3 \rightarrow P^2$.

The relation is expressed by the following equation:

$$s\tilde{m} = P\tilde{M} \quad (3.17)$$

Where $\tilde{M} = [X, Y, Z, 1]^T$ is the homogeneous coordinates of a 3D point $M = [X, Y, Z]^T$ in a Euclidean world coordinate system. $\tilde{m} = [x, y, 1]^T$ is the homogeneous coordinates of a 2D image point $m = [x, y]^T$ in the image plane. s is a scale factor. P is called the perspective projection matrix. It is a 3×4 matrix representing the relationship: $P^3 \rightarrow P^2$.

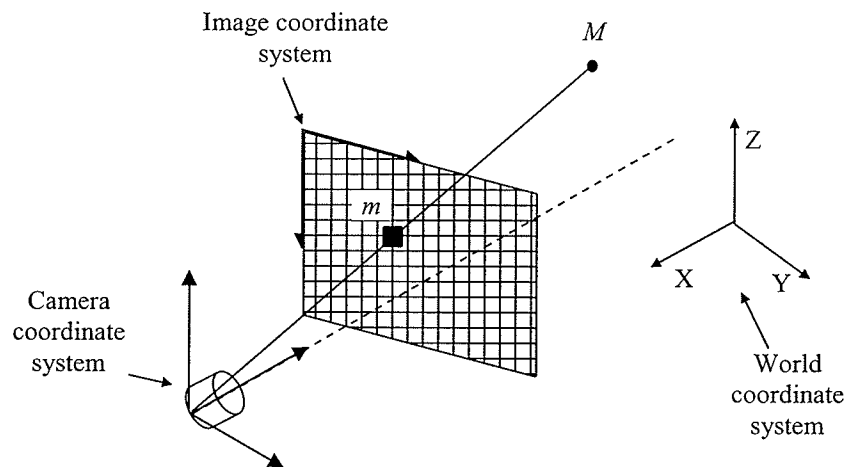


Figure 3.13 Perspective projection from the world coordinate system
to the image plan

Figure 3.13 illustrates the process of transforming a 3D point to a 2D image point. In the figure, the world coordinate system is a scene-centered coordinate system and it is defined by

the system designer. The location of the world coordinate system is arbitrary. The camera coordinate system is a 3D coordinate system with the origin at the optical center of a camera. The x and y axes parallel with the x and y axes in the image plane respectively. The z axis coincides with the optical axis of the camera and points away from the image plane. The image coordinate system is a 2D coordinate system with the origin at the upper left corner of the image. The process includes two steps: one is the transformation between the world coordinate system and the camera coordinate system, the other one is the transformation between the camera coordinate system and the image coordinate system. Therefore the perspective projection matrix P includes two parts: the intrinsic parameters in K and the extrinsic parameters $[R|t]$.

$$P = K[R|t] \quad (3.18)$$

The intrinsic parameters in K are used to convert between the image plane and the camera coordinate system.

$$K = \begin{bmatrix} \frac{f}{S_x} & (\tan \alpha) \frac{f}{S_y} & u_0 \\ 0 & \frac{f}{S_y} & v_0 \\ 0 & 0 & 1 \end{bmatrix} \quad (3.19)$$

Where, f is focal length, α is the skew angle which adjusts the image aspect ratio, and (u_0, v_0) is the image center which is also called the principal point. (S_x, S_y) are pixel dimensions in the x and y directions.

In the camera coordinate system, the unit of the coordinates is metric, but in the image coordinate system, the unit of the image coordinates is pixels. Therefore conversion factors

S_x and S_y are needed to change metric units to pixels. The conversion is illustrated in Figure 3.14.

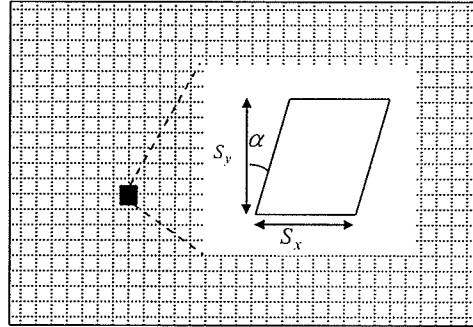


Figure 3.14 Illustration of pixel dimensions

In this research, a simplified matrix of K is used:

$$K = \begin{bmatrix} f_x & s & u_0 \\ 0 & f_y & v_0 \\ 0 & 0 & 1 \end{bmatrix} \quad (3.20)$$

where f_x and f_y are the focal lengths measured in width and height of the pixels, s represents the pixel skew and the ratio $f_x : f_y$ characterises the aspect ratio of the camera.

Extrinsic parameters are needed to transform an object's coordinates in a world coordinate system to a camera coordinate system. It includes two parts:

- A 3D translation vector, t , describing the relative positions of the origins of the two coordinate system, and
- A 3×3 rotation matrix, R , an orthogonal matrix ($R^T R = R R^T = 1$) that aligns the corresponding axes of the two coordinate system.

The orthogonality relations reduce the number of degrees of freedom of R to three.

As a result of some types of imperfections in the design and assembly of the lens composing the cameras, the distortion should be considered. The distortion includes radial distortion and

tangential distortion. The coordinates in undistorted image plane coordinates (x, y) can be obtained from the observed image (distorted image) coordinates (x_d, y_d) by the following equation (Hartley and Zisserman, 2004):

$$\begin{aligned} x &= x_d + (x_d - u_0)(K_1 r^2 + K_2 r^4 + \dots) \\ y &= y_d + (y_d - v_0)(K_1 r^2 + K_2 r^4 + \dots) \end{aligned} \quad (3.21)$$

Where K_1 and K_2 are the first and second parameters of the distortion and

$$r = (x_d - u_0)^2 + (y_d - v_0)^2 \quad (3.22)$$

3.8 2D Homography

The 2D homography (Hartley and Zisserman, 2004) is a projective transformation that maps points from one plane to another plane. Figure 3.15 illustrates the projective transformation. The transformation maps a point (x) in a planar surface (X, Y) in the world coordinate system (O) to one point (x') in an image plane (X', Y') .

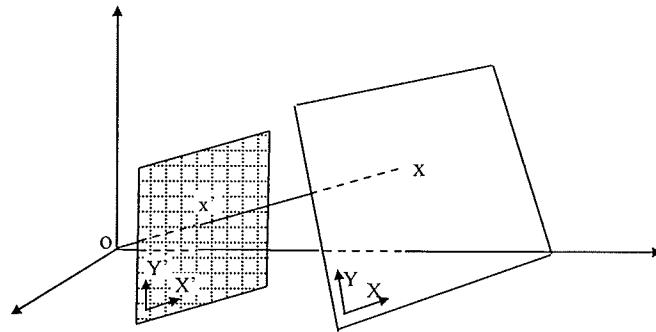


Figure 3.15 2D homography

A homography is represented by a 3×3 –matrix \mathbf{H} .

$$x' = \begin{bmatrix} h_{11} & h_{12} & h_{13} \\ h_{21} & h_{22} & h_{23} \\ h_{31} & h_{32} & h_{33} \end{bmatrix} x \quad \text{OR} \quad x' = Hx \quad (3.23)$$

H introduces a special map between points in the first image and those in the second. For any point x in the first image, its corresponding point x' on the second image is uniquely determined.

3.9 Epipolar geometry

The epipolar geometry (Hartley and Zisserman, 2004) exists in a two-camera system that is shown in Figure 3.16. The figure shows two pinhole cameras. C_l and C_r are their projection center. I_l and I_r are image planes. Each camera identifies a 3D reference frame, the origin of which coincides with the projection center, and the Z-axis with the optical axis. The 3D point P is referred as P_l in left camera reference frame and as P_r in right camera reference frame. They are thought of as vectors $P_l = [X_l, Y_l, Z_l]^T$ and $P_r = [X_r, Y_r, Z_r]^T$ in the camera reference frames respectively. The vectors $p_l = [x_l, y_l, z_l]^T$ and $p_r = [x_r, y_r, z_r]^T$ refer to the projections of P onto the left and right image plane respectively. The focal lengths are denoted by f_l and f_r . R is the rotation matrix and t is the translation matrix.

Points e_l and e_r are called epipole (Hartley and Zisserman, 2004), and they are the intersections of the line joining the two camera centers C_l and C_r with left and right image planes. The plane formed with the three points $C_l P C_r$ is called the epipolar plane. The lines $p_l e_l$ and $p_r e_r$ are called the epipolar lines. They are formed when the epipolar plane intersects with image planes. Consider the triplet P, p_l and p_r . Given p_l , P will lie on the line $C_l P_l$. The image of line $C_l P_l$ in right image is the epipolar line $p_r e_r$, and the line is through the corresponding point p_r . This constraint is called epipolar constraint. It establishes a mapping between points in the left image and lines in the right image and vice

with

$$E = R \begin{bmatrix} 0 & -t_z & t_y \\ t_z & 0 & -t_x \\ -t_y & t_x & 0 \end{bmatrix} \quad (3.29)$$

The matrix E is called the essential matrix E . It establishes a link between the epipolar constraint and the extrinsic parameters of the camera system.

Based on Equation 3.2, following equations can be obtained.

$$p_l = \frac{f_l}{Z_l} P_l \quad \text{and} \quad p_r = \frac{f_r}{Z_r} P_r \quad (3.30)$$

Using Equation 3.30 with Equation (3.28), the epipolar line l_r on the right image can be obtained

$$l_r = E p_l \quad (3.31)$$

Expressing the epipolar constraint algebraically, the following equation needs to be satisfied in order for p_l and p_r to be matched:

$$p_r^T F p_l^T = 0 \quad (3.32)$$

where F is a 3×3 matrix called the fundamental matrix (Hartley and Zisserman, 2004). The following equation also holds:

$$l_r = F p_l \quad (3.33)$$

3.10 3D reconstructions from two 2D images

The methods mentioned in above sections are for detecting features in images, solving the correspondence problem and determining the epipolar geometry. The 3D reconstruction can be obtained based on the parameters obtained from these methods. Given the coordinates of

the corresponding image points from two 2D images, if both intrinsic and extrinsic parameters are known then the reconstruction problem can be solved by triangulation.

Figure 3.17 shows the geometry of the triangulation method. $p_l = (x_l, y_l)$ and $p_r = (x_r, y_r)$ are two known image points in the image coordinate system of image plane I_l and I_r . The projective matrix $P = K[R|t]$ of the system is known. The 3D coordinates of point P is unknown and can be calculated using these parameters. $[X_w, Y_w, Z_w]$ is the world coordinate system. $[x_l, y_l, z_l]$ and $[x_w, y_w, z_w]$ are the camera coordinate systems of the left and right camera. C_l and C_r are the optical centers of the left and right cameras.

From Equation (3.17), the following equations can be obtained (Hartley and Zisserman, 2004),

$$\begin{bmatrix} sx_l \\ sy_l \\ s \end{bmatrix} = \begin{bmatrix} P_{l11} & P_{l12} & P_{l13} & P_{l14} \\ P_{l21} & P_{l22} & P_{l23} & P_{l24} \\ P_{l31} & P_{l32} & P_{l33} & P_{l34} \end{bmatrix} \begin{bmatrix} X_w \\ Y_w \\ Z_w \\ 1 \end{bmatrix} \quad (3.34)$$

and

$$\begin{bmatrix} sx_r \\ sy_r \\ s \end{bmatrix} = \begin{bmatrix} P_{r11} & P_{r12} & P_{r13} & P_{r14} \\ P_{r21} & P_{r22} & P_{r23} & P_{r24} \\ P_{r31} & P_{r32} & P_{r33} & P_{r34} \end{bmatrix} \begin{bmatrix} X_w \\ Y_w \\ Z_w \\ 1 \end{bmatrix} \quad (3.35)$$

Re-arrange the equations,

$$(P_{l11} - P_{l31}x_l)X_w + (P_{l12} - P_{l32}x_l)Y_w + (P_{l13} - P_{l33}x_l)Z_w = P_{l34}x_l - P_{l14} \quad (3.36)$$

$$(P_{l21} - P_{l31}y_l)X_w + (P_{l22} - P_{l32}y_l)Y_w + (P_{l23} - P_{l33}y_l)Z_w = P_{l34}y_l - P_{l24} \quad (3.37)$$

and,

$$(P_{r11} - P_{r31}x_r)X_w + (P_{r12} - P_{r32}x_r)Y_w + (P_{r13} - P_{r33}x_r)Z_w = P_{r34}x_r - P_{r14} \quad (3.38)$$

$$(P_{r21} - P_{r31}y_r)X_w + (P_{r22} - P_{r32}y_r)Y_w + (P_{r23} - P_{r33}y_r)Z_w = P_{r34}y_r - P_{r24} \quad (3.39)$$

The relation of M, P and B can be expressed as,

$$MP = B \quad (3.40)$$

where,

$$M = \begin{bmatrix} P_{l11} - P_{l31}x_l & P_{l12} - P_{l32}x_l & P_{l13} - P_{l33}x_l \\ P_{l21} - P_{l31}y_l & P_{l22} - P_{l32}y_l & P_{l23} - P_{l33}y_l \\ P_{r11} - P_{r31}x_r & P_{r11} - P_{r31}x_r & P_{r11} - P_{r31}x_r \\ P_{r21} - P_{r31}y_r & P_{r22} - P_{r32}y_l & P_{r23} - P_{l33}y_r \end{bmatrix} \quad (3.41)$$

$$P = \begin{bmatrix} X_w \\ Y_w \\ Z_w \end{bmatrix} \quad (3.42)$$

$$B = \begin{bmatrix} P_{l34}x_l - P_{l14} \\ P_{l34}y_l - P_{l24} \\ P_{r34}x_r - P_{r14} \\ P_{r34}y_r - P_{r24} \end{bmatrix} \quad (3.43)$$

The 3D coordinates of point P can be obtained by,

$$P = (M^T M)^{-1} M^T B \quad (3.44)$$

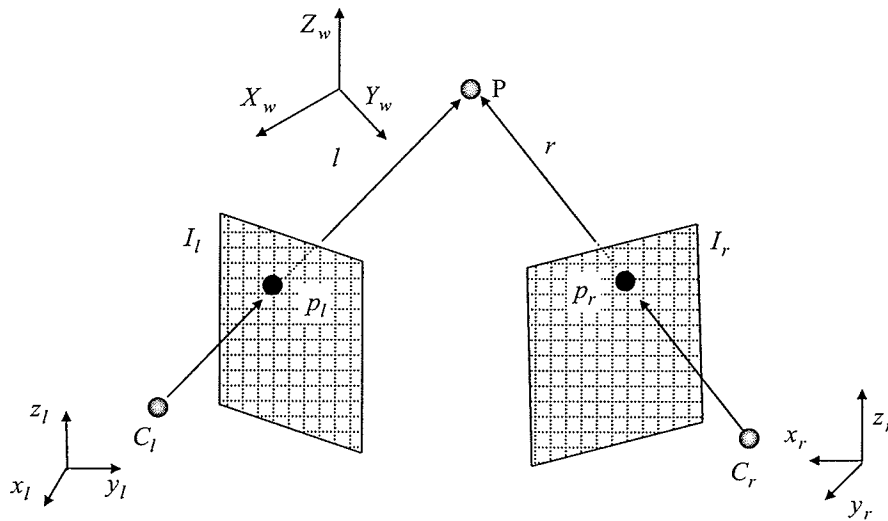


Figure 3.17 The geometry of the triangulation method

Chapter 4

Automatic detection of checkerboard pattern for camera calibration

This chapter describes a novel method developed in this research for automatic camera calibration. Experimental results are also presented in this chapter.

4.1 Introduction

In this chapter, a novel method is proposed for the feature extracting and matching of the checkerboard pattern in unconstrained environments. A novel checkerboard pattern, as shown in Figure 4.1, is designed in this research. Five double-triangle figures are placed at four corners and the centre of the checkerboard pattern respectively. The feature points of the pattern are grid corners formed by all black or white squares shown in Figure 4.1. The double-triangle figures are used to find the location of the checkerboard pattern and feature points of the pattern by an iterative cross-correlation method.

As the checkerboard pattern is on a plane, all feature points on the checkerboard pattern are on the plane. The relationship between all feature points on the pattern and their images is related by homography H . After coordinates of the four corners are found on the image of the checkerboard pattern, the coordinates of feature points in the image of the pattern can be computed using a homograph algorithm. Then these coordinates are sent to a corner finding algorithm to find a precise location of feature points. The coordinates of feature points can be

used in the camera calibration algorithm. This method will be tested in different lighting conditions, with a complicated background and in different view orientations.

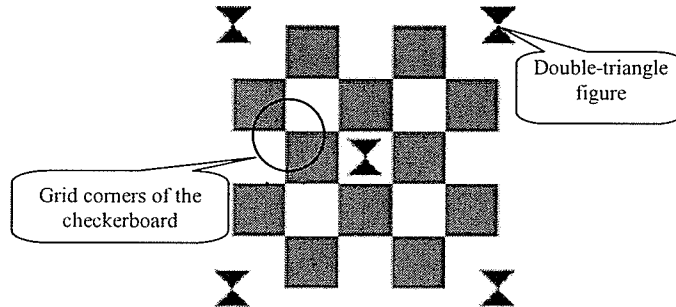


Figure 4.1 The proposed checkerboard pattern with special designed figures

4.2 Pattern-based camera calibration

The pattern-based calibration method is used to calibrate a camera in this research. One of the popular calibration patterns is the checkerboard pattern (Zhang, 1999). As shown in Figure 4.2, the checkerboard pattern defines a world coordinate system. The coordinates of the corners of the black squares on the checkerboard pattern are known in terms of this coordinate system. After these corners in the image are extracted, the correspondence between the 3D points and the 2D image points gives a homography H mentioned in Chapter 3. The intrinsic and extrinsic parameters of a camera can be calculated by using the homography H .

To establish the homography between the checkerboard pattern and its image, it can be assumed that the checkerboard pattern lies at $Z = 0$ in the world coordinate system. Then the projection of a 3D point M on the checkerboard pattern to its image m can be expressed as:

$$\tilde{sm} = K[R \quad t]\tilde{M} \quad (4.1)$$

Where: $K = \begin{bmatrix} \alpha & \gamma & u_0 \\ 0 & \beta & v_0 \\ 0 & 0 & 1 \end{bmatrix}$ is the intrinsic parameter of a camera, α is scaling factor in x -axes,

β is scaling factor in y -axes, γ is the parameter describing the skew of the two image axes and (u_0, v_0) is the coordinate pair of the principle point. $R = [r_1 \ r_2 \ r_3]$ is the rotation matrix from the world system to the camera system, and t is translation vector from the world system to the camera system.

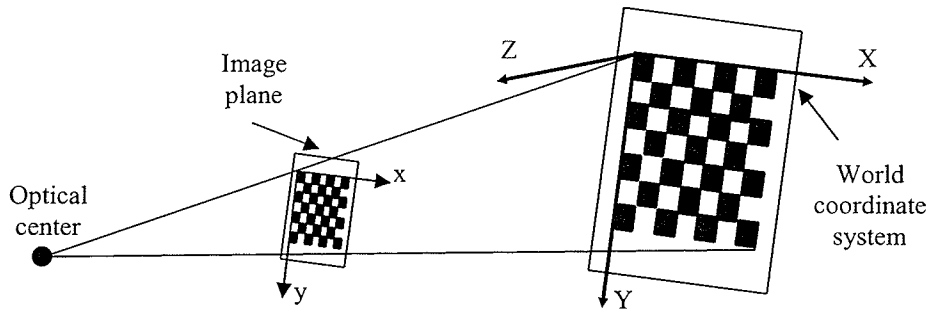


Figure 4.2 The coordinate systems defined by a checkerboard pattern

The model plane is located at $Z = 0$ of the world coordinate system. Therefore, a pattern point M and its image point m are related by a homograph H :

$$sm = HM \text{ and } H = K[r_1 \ r_2 \ t] \quad (4.2)$$

The maximum likelihood method (Zhang, 1999) is used to estimate H . As the image points m_i are corrupted by noise, a maximum likelihood criterion of H is obtained by minimizing the following equation:

$$\min_H \sum_i \|m_i - \hat{m}_i\|^2 \quad (4.3)$$

where

$$\hat{m}_i = \frac{1}{\tilde{h}_3^T M_i} \begin{bmatrix} \tilde{h}_1^T M_i \\ \tilde{h}_2^T M_i \end{bmatrix} \quad (4.4)$$

with \tilde{h}_i is the i^{th} row of H . The nonlinear minimization can be solved using the Levenberg-Marquardt algorithm (Hartley and Zisserman, 2004).

If the homograph is denoted by $H = [h_1 \quad h_2 \quad h_3]^T$, the following can be obtained.

$$[h_1 \quad h_2 \quad h_3]^T = \lambda K [r_1 \quad r_2 \quad t] \quad (4.5)$$

Where λ is an arbitrary scalar.

Because r_1 and r_2 are orthonormal, the following two constrains can be obtained:

$$h_1 K^{-T} K^{-1} h_2 = 0 \quad \text{and} \quad h_1 K^{-T} K^{-1} h_1 = h_2 K^{-T} K^{-1} h_2 \quad (4.6)$$

$$\text{Let } B = K^{-T} K^{-1} \equiv \begin{bmatrix} B_{11} & B_{12} & B_{13} \\ B_{12} & B_{22} & B_{23} \\ B_{13} & B_{23} & B_{33} \end{bmatrix}$$

If correspondent points can be obtained in at least three images, a unique solution of B can be obtained. Once B is estimated, all camera intrinsic parameters can be calculated as follows.

$$\begin{aligned} v_0 &= (B_{12}B_{13} - B_{11}B_{23}) / (B_{11}B_{22} - B_{12}^2) \\ \lambda &= B_{33} - [B_{13}^2 + v_0(B_{12}B_{13} - B_{11}B_{23})] / B_{11} \\ f_x &= \sqrt{\lambda / B_{11}} \\ f_y &= \sqrt{\lambda B_{11} / (B_{11}B_{22} - B_{12}^2)} \\ s &= -B_{12}\alpha^2 \beta / \lambda \\ u_0 &= \gamma v_0 / \alpha - B_{13}\alpha^2 / \lambda \end{aligned} \quad (4.7)$$

The external parameters for each image can also be calculated after the intrinsic parameters of the camera are obtained. The extrinsic parameters can be calculated by Equation (3.19).

$$\begin{aligned} r_1 &= \delta K^{-1} h_1 \\ r_2 &= \delta K^{-1} h_2 \\ r_3 &= r_1 \times r_2 \\ t &= \delta K^{-1} h_3 \end{aligned} \quad (4.8)$$

where the scalar $\delta = 1/\|K^{-1}h_1\| = 1/\|K^{-1}h_2\|$

This method requires the camera to observe the checkerboard pattern from at least 3 views to calculate all intrinsic and extrinsic parameters. Therefore, a set of pattern-image feature point's pairs has to be accurately provided. The coordinates of the feature points on the checkerboard pattern are measured directly on the pattern. The corresponding image feature points should be detected in the image.

4.3 Pattern design

There are three problems that have to be solved for finding and matching the feature points of a checkerboard pattern in an image. One problem is the shape change of geometric figures in the image because of the perspective projection, for example, a circle will become an ellipse after a perspective projection. The second problem is the image noise when pictures are taken in the real-world. The third problem is that the correlation method is a robust method for objects recognition in unconstrained environments but it is sensitive to the scaling or rotation of objects (Gonzalez and Woods, 2002; Horner and Gianino, 1984). The checkerboard pattern is difficult to be found in the image under these three problems. Therefore, in this research, a special designed double-triangle figure is placed on the checkerboard pattern to provide a solution for above-mentioned problems.

Based on the correlation method, the double-triangle figure is designed from experimental results. Comparing with circle, rectangle and triangle figures, the double-triangle figure has three features: (1) It can keep maximum contrast in different conditions as its colour is half black and half white; (2) It can keep the most similarity to perspective projection of the

figure after rotating or scaling the figure; and (3) The accurate position of the figure centre in the image can be obtained using a corner-finding algorithm. Therefore, the double-triangle figure is suitable to this research.

Figure 4.3 shows the experiments to explain these features. The double-triangle template image is obtained by rotating and scaling the original figure. And then the template image is used to compute a correlation with the source image. The source image is composed by a perspective projection of four geometries that include circle, rectangle, double-triangle and triangle. From the correlation maps shown in Figure 4.3, the maximum correlation values are at the location of the double-triangle figure. That means double-triangle figure can keep similarity with the perspective projection after rotating and scaling. The position of a double-triangle figure in an image is the centre location of the double-triangle figure. The positions of double-triangle figures obtained from the correlation computation may sometimes have errors because of the noise in the image or shape change after the perspective projection. The accurate position can be obtained using corner-finding algorithms because the centre of the double-triangle figure is the intersection of the edges of two triangles.

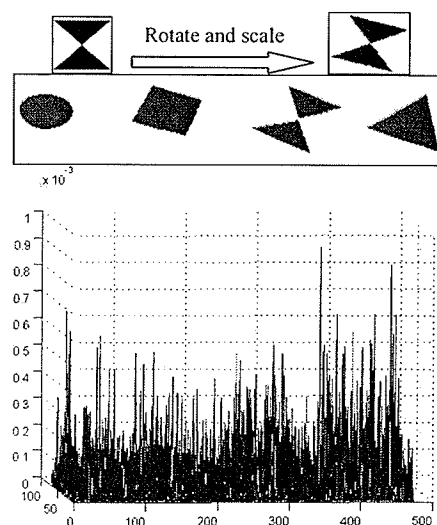


Figure 4.3 Double-triangle figure, a template and correlation map

4.4 Position check of double-triangle figures

After the correlation computing, five positions with the maximum value are selected from the correlation map as the positions of five double-triangle figures. A test is performed to check positions of the five double-triangle figures in the image. Homography is used to test the correction of positions of the double-triangle figures. The principle of the homography is described as follows:

If the coordinate of a point in the checkerboard pattern is known as X_p , homography H is known between the pattern and pattern's image, and the coordinate of a point on pattern's image is obtained as x_p , then:

$$x_p - HX_p = 0 \quad (4.9)$$

To use the homography method to check the positions, a coordinate system is set up on the checkerboard pattern shown in Figure 4.4. The origin is at top-left corner of the pattern. The coordinates of positions of all five figures in the pattern are known because the structure of the pattern is known, i.e., coordinates of points on the pattern are known after a coordinates system is set up on the pattern. A coordinate system for the pattern's image is set up similarly as follows: the origin is located at top-left corner of the image, X axis points left and Y axis directs down. The coordinates of double-triangle figures in the image of the checkerboard pattern can be obtained using the correlation method. Coordinates of four corner figures shown in Figure 4.4 are then used to calculate the homography H between the image and pattern. The coordinate of the middle figure in the pattern and the homography H are used in Equation (4.9) to calculate coordinates of the middle figure on the image. Using the calculated coordinate to compare with the coordinate of the middle figure obtained by

correlation method, if they are equal, the positions obtained in the image by the correlation method are correct positions of double-triangle figures.

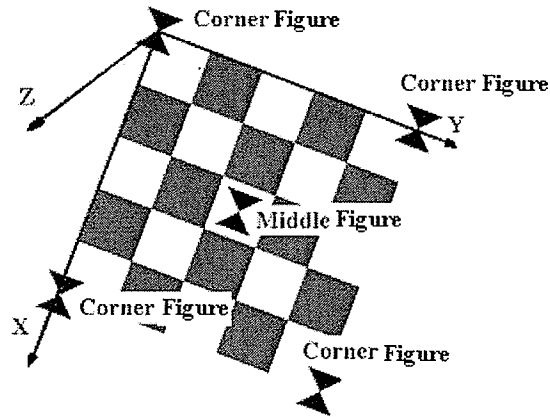


Figure 4.4 Coordinate system of the pattern

4.5 Automatic detection of checkerboard

To find all feature points from an image of the checkerboard pattern, two steps are needed. First step is to find the checkerboard pattern in the image. The second step is to find all feature points of the pattern in the image. An iterated method is developed to automatically find the pattern and all feature points on the pattern's image based on the principle described in Sections 4.3 and 4.4. Figure 4.5 shows the process of this method. The details of the processing are described as follows:

Step 1: A picture of the proposed checkerboard pattern is taken. A filter is used to de-noise the picture. The colour image is converted into a greyscale image.

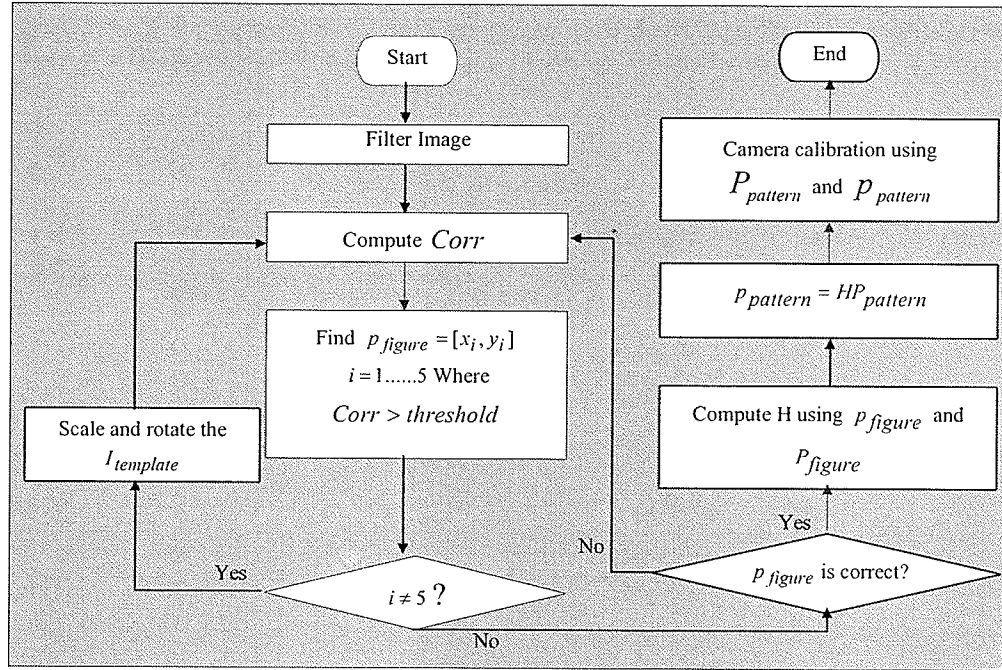


Figure 4.5 The block diagram of the feature detection

Step 2: The correlation is calculated between a double-triangle template and the picture of the checkerboard pattern. The double-triangle template is a small image as shown in Figure 4.6 with a double-triangle figure on it defined as $I_{Template}$ with size $J \times K$ pixels. The image of the checkerboard pattern is defined as I_{Source} with size $M \times N$ pixels, where $J \leq M$ and $K \leq N$.



Figure 4.6 Example of a template image and template size (20x20 pixels)

The correlation $Corr$ between the template and the image can be calculated by Equation (4.10).

$$Corr = F^{-1} \left(F_{\phi} (I_{source}) \cdot F_{\phi}^* (I_{template}) \right) \quad (4.10)$$

Where F^{-1} is the inverse Fourier Transform, $F_{\phi}(I_{source})$ is the phase-only part of the Fourier Transform of I_{source} . $F_{\phi}^*(I_{template})$ is the complex conjugate of the phase-only part of the Fourier Transform of $I_{template}$.

After the correlation computing, a correlation threshold is used to find the position of all double-triangle figures. The threshold is set up based on the test and try in computation. If $Corr > threshold$ at one position of the pattern image then the position is assumed to be the position of a double-triangle figure in the image.

Step 3: All positions of the five double-triangle figures p_{figure} are obtained in step 2. They are $p_{figure} = [x_i, y_i]^T$ $i = 1 \dots 5$, where $[x_i, y_i]$ are coordinates of the positions of the five double-triangle figures, and i is the number of five double-triangle figures. If there are more or fewer than five positions found in Step 2 ($i \neq 5$), the template $I_{Template}$ will be rotated and scaled and go back to Step 2.

Step 4: A test is performed to check that p_{figure} are the correct positions of the five double-triangle figures in the image. The details of the test method have been described in Section 4.4. If the test fails, the template $I_{Template}$ will be rotated and scaled, then return to Step 2.

Step 5: A homography method is used to find positions of all feature points in the image. The method is described as below. Firstly, a coordinate system is set up on the pattern as shown in Figure 4.4. The origin is at the top-left double-triangle figure. The coordinates of all feature points $P_{pattern} = [X, Y, 0]^T$ in the pattern are known, where $[X, Y, 0]$ is the coordinate of the feature points on the pattern. The coordinates of positions of all double-triangle figures $P_{figure} = [X_i, Y_i, 0]^T$ $i = 1 \dots 5$ are known, where $[X_i, Y_i, 0]$ are the coordinates of the double-

triangle figures on the pattern, i is the number of five double-triangle figures. Secondly, a coordinate system for image of the pattern is set up as described in Section 4.4. P_{figure} has been obtained in step 4. Thirdly, P_{figure} and p_{figure} are used to compute the homography H between the checkerboard pattern and the image of the pattern. then, the coordinates of all grid corners $p_{pattern}$ are computed using Equation (4.11).

$$p_{pattern} = HP_{pattern} \quad (4.11)$$

Finally, $p_{pattern}$ are used in a sub-pixel corners finding algorithm to get accurate coordinates of these feature points. All coordinates of the feature points are used in a calibration program to compute the intrinsic and extrinsic parameters of the camera.

4.6 Experiments

The checkerboard pattern shown in Figure 4.2 is designed on a letter-sized (28*21 cm) paper, and is mounted on a flat panel. The size of black and white blocks in the pattern is 29*29 mm. The size of the double-triangle figures is 20*20 mm. Three digital cameras (Sony MVC-FD97, Kodak DC3200 and Sumsung SC-D353) with 640x480 pixels JPEG image format are used to test that the algorithm is reliable for different cameras. The algorithm is implemented using MATLAB.

The proposed method is tested in different conditions that include the pattern of different sizes, with a different background and uneven illumination. Seven test images are selected to cover these conditions as shown from Figures 4.7 to 4.11. In the experiments the template is rotated around Z axis based on a left-hand coordinate system and scaled in searching process to detect the double-triangle figures in the image. The template sizes and rotating angles used

to find the double-triangle figures are shown in brackets of the Figures. All feature points of the pattern found by the detection method are shown in Figures within the rectangles. The light used in Figure 4.7 is an even light of indoor, size of the template is 11*11 pixels and rotating angle is 0. High contrast lights are used in Figures 4.8. A lamp is used in Figure 4.8 to generate a high light on the pattern. There is no background light in Figure 4.8. The size of the template is 11*11 pixels and rotation angles are 0. The pattern is captured in sun light with a natural background as shown in Figures 4.9 and 4.10, both template sizes are 15*15 pixels and rotation angles are 0. In Figure 4.11 the light condition is same as in Figure 4.7, but the pattern has an angle with the camera. Size of the template is 11*11 pixels and rotating angle is 12. In Figures 4.12 Kodak digital cameras are used in experiments. Size of the template is 11*11 pixels and rotating angle is -10. In Figures 4.13 Sumsung digital cameras are used. Size of the template is 11*11 pixels and rotating angle is 0.

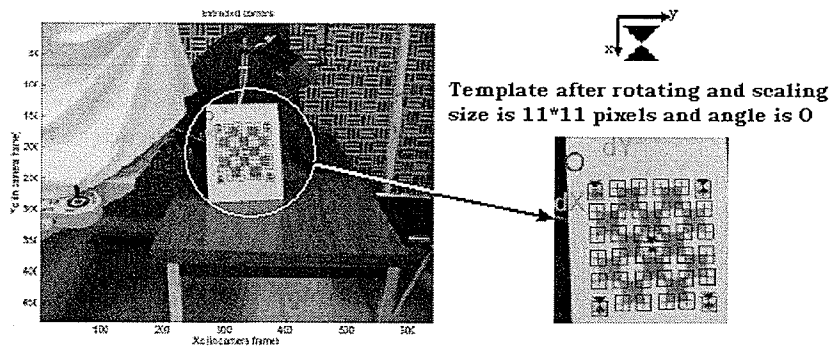


Figure 4.7 Even lights of indoor
(the template size 11*11, rotate angle:0)

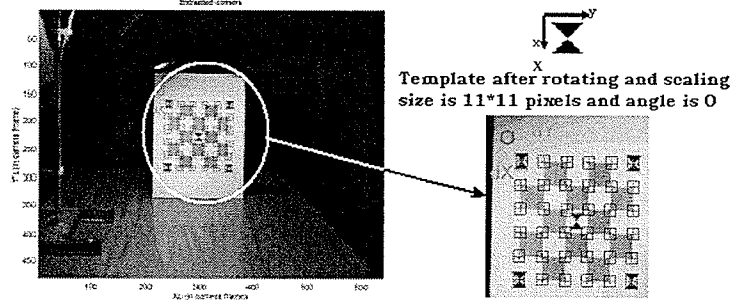


Figure 4.8 High contrast lighting in the indoor environment (the template size 11*11, rotate angle: 0)

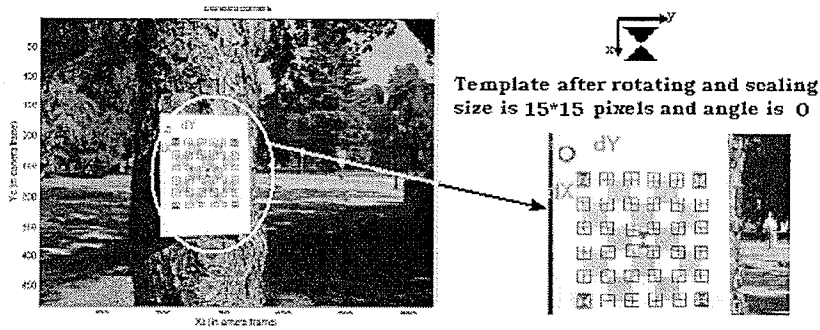


Figure 4.9 Sun light with complex background (the template size 15*15, rotate angle:0)

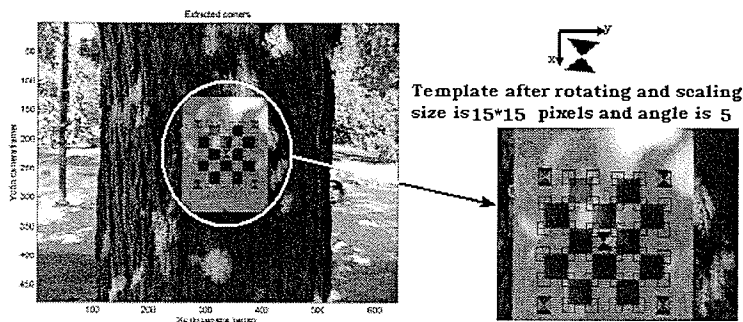


Figure 4.10. Sun light with shade (the template size 15*15 rotating angle: 5)

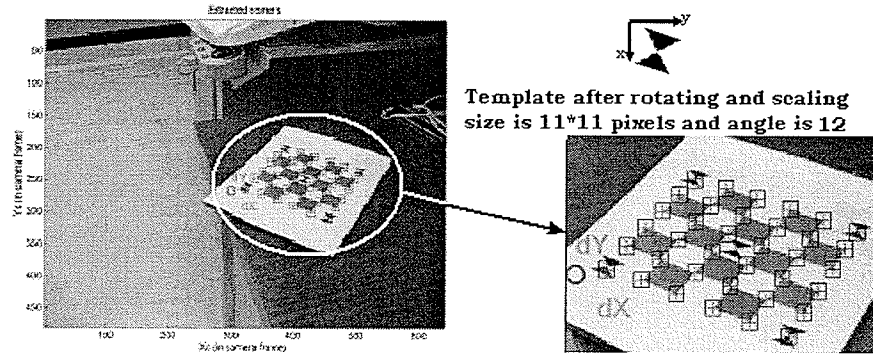


Figure 4.11 Pattern in an angle
(the template size 11*11, rotating angle: 12)

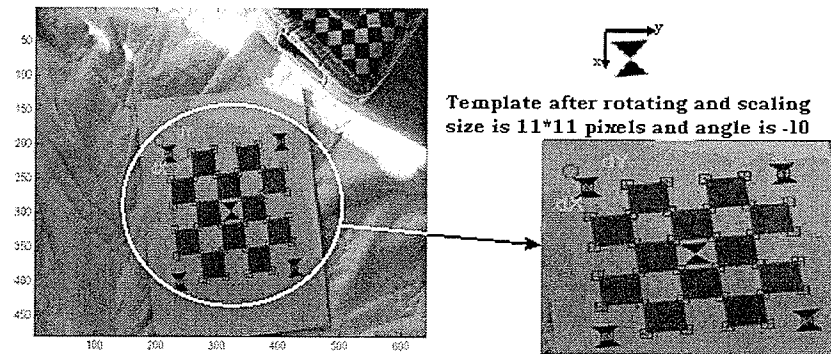


Figure 4.12 The picture is taken by Kodak digital camera
(the template size 11*11, rotating angle: -10)

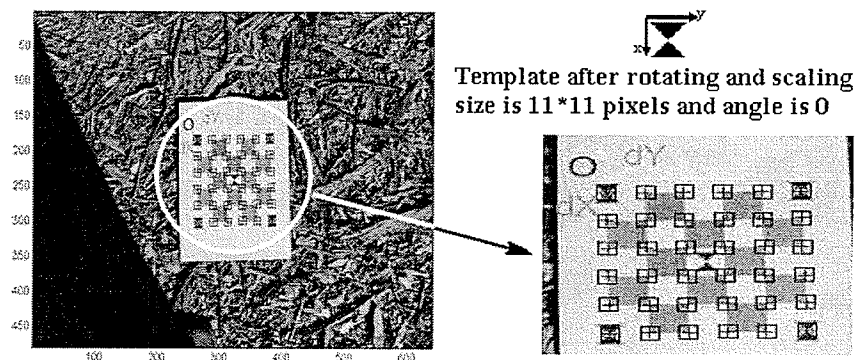


Figure 4.13 The picture is taken by Samsung camcorder
(the template size 11*11, rotating angle: 0)

P_{figure} and p_{figure} are obtained after recognitions of the checkerboard. They are used to calibrate the camera. Figure 4.14 shows a series of images of the new checkerboard pattern that had been taken from nine different views.

The tests are compared with a manual method to prove that P_{figure} and p_{figure} obtained by the double-triangle method are suitable for the camera calibration. In the manual method, the locations of the checkerboard pattern in the images are selected by the user and then all feature points are obtained by a corner detecting method. Table 4.1 shows the obtained intrinsic parameters of the camera using the double-triangle method and manual method. Table 4.2 shows the obtained extrinsic parameters by the double-triangle method and manual method. Extrinsic parameters include rotation matrix and translation matrix. In this research, the rotation vector is used to represent the rotation matrix. The rotation vector and the rotation matrix are related through the Rodrigues formula (Bouguet, 2002). The experimental results show that the intrinsic and extrinsic parameters obtained by the double-triangle method are almost as same as those obtained by the manual method, therefore, the double-triangle method is a feasible method for the camera calibration.

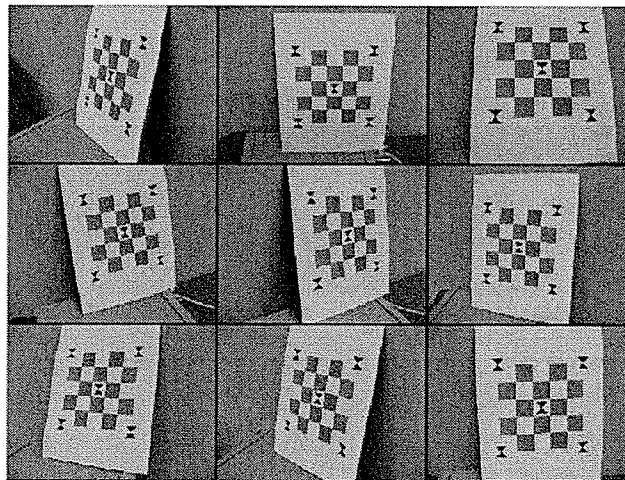


Figure 4.14 Images of the new checkerboard pattern

Table 4.1 Experimental results of the intrinsic parameters of the camera

Intrinsic parameters	Double-triangle method	Manual method
$[f_x, f_y]$	$[743.8, 745.2] \pm [6.7, 6.1]$	$[741.3, 747.4] \pm [7.1, 6.9]$
$[u_o, v_o]$	$[324.4, 233.9] \pm [7.3, 7.2]$	$[325.4, 232.9] \pm [8.1, 8.5]$
s	0.00	0.00

Table 4.2 Experimental results of the extrinsic parameter for one image

Extrinsic parameters	Double-triangle method	Manual method
Rotation vectors	$[-2.2, -2.1, -0.2]$	$[-2.5, -2.7, -0.2]$
Rotation errors	$[\pm 0.1, \pm 0.1, \pm 0.1]$	$[\pm 0.1, \pm 0.1, \pm 0.1]$
Translation vectors	$[-60.5, -64.1, 405.9]$	$[-61.2, -66.4, 402.5]$
Translation errors	$[\pm 4.4, \pm 4.6, \pm 4.1]$	$[\pm 5.1, \pm 5.4, \pm 4.8]$

Chapter 5

A unified calibration method for FTP systems

This chapter presents a novel approach in calibrating an FTP system using only one image. The introduction of the FTP method and the system parameters obtained from the calibration process are presented first. The principle of the proposed method, the system hardware and the process of the FTP-based 3D data acquisition method are then discussed. The experimental results are also presented.

5.1 Introduction

In research mentioned in the literature review of Chapter 2, a series of images are required from different locations of the calibration pattern, for the system calibration. The mass data of the images have to be processed. The calibration procedure is a time-consuming process. In this chapter, a unified calibration method for the FTP-based 3D data acquisition is proposed. There is only one image of a specially designed pattern needed to calibrate the FTP-based 3D data acquisition system. The height calibration and the plane calibration are unified in one step. Therefore this method suggests a faster and simpler way to calibrate FTP-based 3D data acquisition systems.

5.2 The FTP method and 3D coordinates calculation

5.2.1 Object's 3D shape and phase

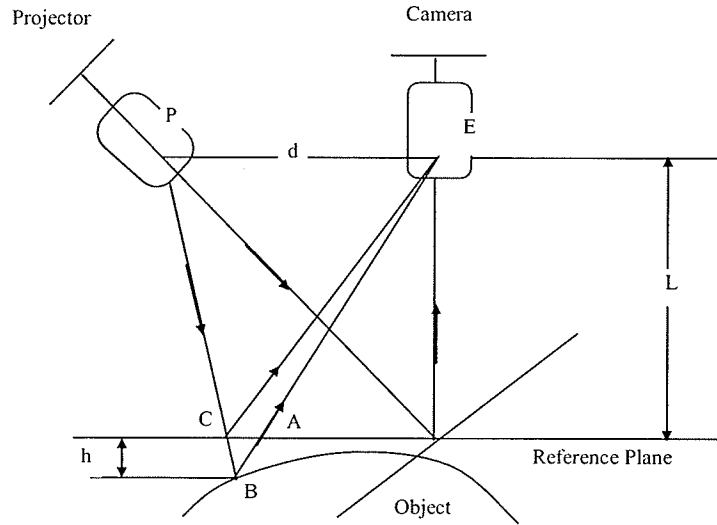


Figure 5.1 A geometry structure of the projection and image system

Figure 5.1 shows the geometry of a projection and imaging system. Points P and E are the optical centers of the projector and camera respectively. The relationship of phase and height is obtained based on the paper of Takeda and Mutoh (1983). Thus,

$$h(x, y) = \frac{L}{d} AC = L \Delta\phi(x, y) / (\Delta\phi(x, y) - 2\pi f_r d) \quad (5.1)$$

where L is the distance between the optical center of the camera and the reference plane; d is the distance between P and E; f_r is the spatial frequency of the projected fringes in the reference plane; $\Delta\phi(x, y)$ is the phase information, which contains the surface height information.

If the phase $\Delta\phi(x, y)$ is obtained then the height information of the surface can be calculated.

FTP is used to compute the phase $\Delta\phi(x, y)$.

5.2.2 FTP methods

When an object is put on the reference plane, the deformed grating image can be expressed by

$$g(x, y) = r(x, y) \sum_{n=-\infty}^{n=\infty} A_n \exp(i(2\pi n f_{r_0} x + n \varphi(x, y))) \quad (5.2)$$

when $h(x, y) = 0$, the grating image is written as

$$g_0(x, y) = r_0(x, y) \sum_{n=-\infty}^{n=\infty} A_n \exp(i(2\pi n f_{r_0} x + n \varphi_0(x, y))) \quad (5.3)$$

where $r(x, y)$ and $r_0(x, y)$ are non-uniform distributions of reflectivity on the surface of the object and on the reference plane respectively. The A_n are the weighting factors of Fourier series, f_{r_0} is the fundamental frequency of the observed grating image, $\varphi(x, y)$ is the phase resulting from the object height distribution and $\varphi_0(x, y)$ is the original phase when $h(x, y) = 0$.

The 1D Fourier transform of the observed image in Equation (5.2) is computed and the Fourier spectrum of the image is obtained. A series of filters are applied to the Fourier spectrum image. The filtering operations determine the quality of phase information. The objective of filtering operations is to remove the direct component and all noises around the fundamental spectrum. These operations can be conceptually separated into three steps: removing the direct component, removing negative frequency components and removing noise around the fundamental spectrum in the positive spectrum. Figure 5.2 shows this process.

The inverse Fourier transform is applied to the fundamental component. The image is transformed back to the spatial domain. The real and imaginary components resulting from the result are used to calculate the phase information.

An image that only carries the deformed grating information is obtained:

$$\hat{g}(x, y) = A_1 r(x, y) \exp(i2\pi f_{r_0} x + \phi(x, y)) \quad (5.4)$$

The same operation is applied to Equation (5.3), then

$$\hat{g}_0(x, y) = A_1 r_0(x, y) \exp(i2\pi f_{r_0} x + \phi_0(x, y)) \quad (5.5)$$

The phase $\Delta\phi(x, y)$ that has relationship with the height distribution is:

$$\Delta\phi(x, y) = \text{Im} \{ \log[\hat{g}(x, y) \hat{g}_0^*(x, y)] \} \quad (5.6)$$

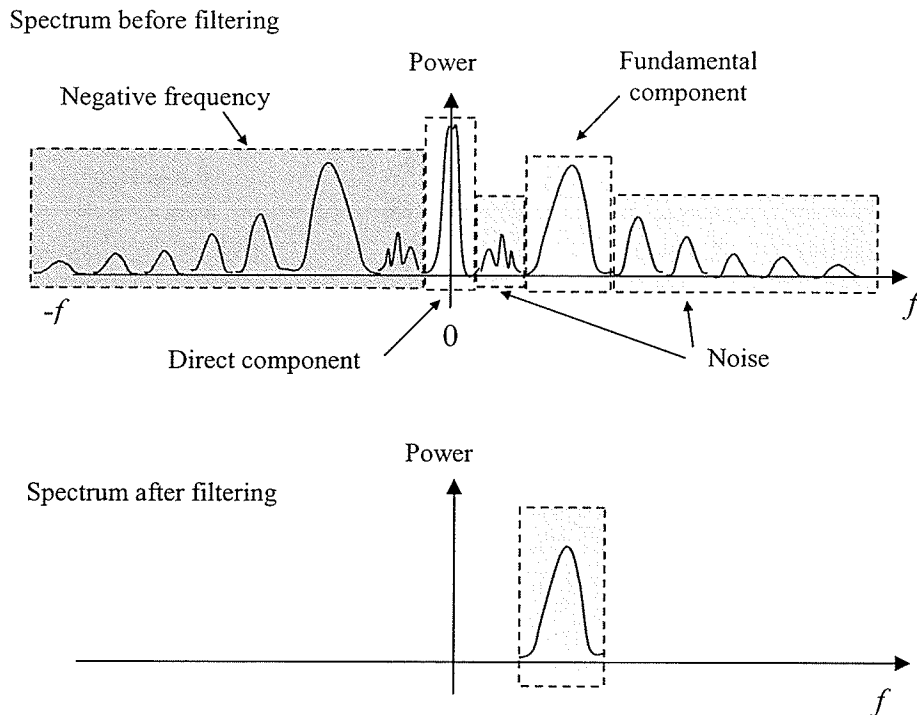


Figure 5.2 Filtering in the Fourier spectrum

Figure 5.3 shows the process of a FTP method. The details are described as follows.

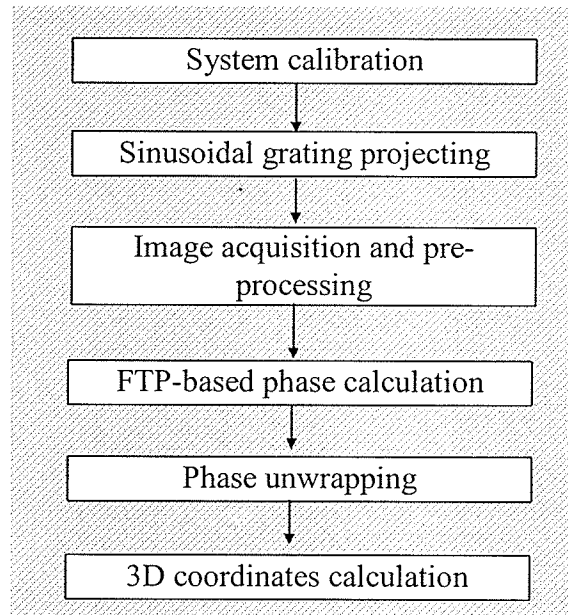


Figure 5.3 The overall structure of the FTP algorithm

(1) System calibration accurately determines parameters in the FTP method. The parameters are geometrical parameters of the system and internal parameters of digital cameras. Generally these parameters are difficult to measure directly. A calibration procedure is used to obtain these parameters for the FTP method.

(2) Using sinusoidal grating projection, a grey scale grating with the intensity varying sinusoidally across the grating is projected onto the object. An image of a sinusoidal grating is shown in Figure 5.4.

(3) Two images are required for the image acquisition and pre-processing. One is the reference-grating image, and the other is deformed grating image. The noises in the acquired images have to be removed by the pre-processing.

(4) For FTP-based phase calculation, the acquired images are computed by One-dimensional (1D) Fourier transform to obtain Fourier spectra. The spectra are then filtered to obtain the

fundamental component with a mid-pass filter function. The inverse Fourier transform is applied to the fundamental component to obtain the required phase information.



Figure 5.4 A sinusoidal grating

(5) Since the phase calculated by the FTP method gives principal values ranging from $-\pi$ to π . The phase distribution is wrapped into this range and has discontinuities with 2π jumps when the phase variation is larger than 2π . These discontinuities can be corrected by adding or subtracting 2π according to the phase jump ranging from $-\pi$ to π or vice versa. The procedure of constructing the continuous natural phase is called phase unwrapping.

(6) Based on the phase information, the 3D coordinates of points on the object can be calculated.

5.2.3 Phase unwrapping

Since the phase calculated by FTP methods gives principal values ranging from $-\pi$ to π , the phase distribution is wrapped into this range and has discontinuities with 2π jumps when the phase variation is larger than 2π . These discontinuities can be corrected by adding or subtracting 2π according to the phase jump ranging from $-\pi$ to π or vice versa.

5.2.4 3D coordinates calculation

Based on the phase information, 3D coordinates of the object's surface can be calculated. As shown in Figure 5.5, the world coordinate system is set that X, Y coordinates are on the

reference plane and the coordinate centre is in a line with the coordinate centre of the camera coordinate system. X , Y and Z are parallel with the x , y and z of the camera coordinate system. The principal point of the camera is assumed at the centre of the image, the skew coefficient and distortions are zero. Therefore, the 3D coordinates (X , Y , and Z) of a point on the object can be calculated as follows:

Z coordinate is the height $h(x, y)$ from the point on the object to the reference plane and it can be calculated by Equation (5.1). X coordinate can be calculated as follows:

$$X = \frac{U * L}{f / \alpha} \quad (5.7)$$

where U is the coordinate of the point in the image coordinate system, f is the focus length of the camera, α is the size of a pixel on image and L is the distance from the optical center of the camera to the reference plane. Y coordinate can be calculated as follows:

$$Y = \frac{V * L}{f / \alpha} \quad (5.8)$$

where V is the coordinate of the point in image coordinate system.

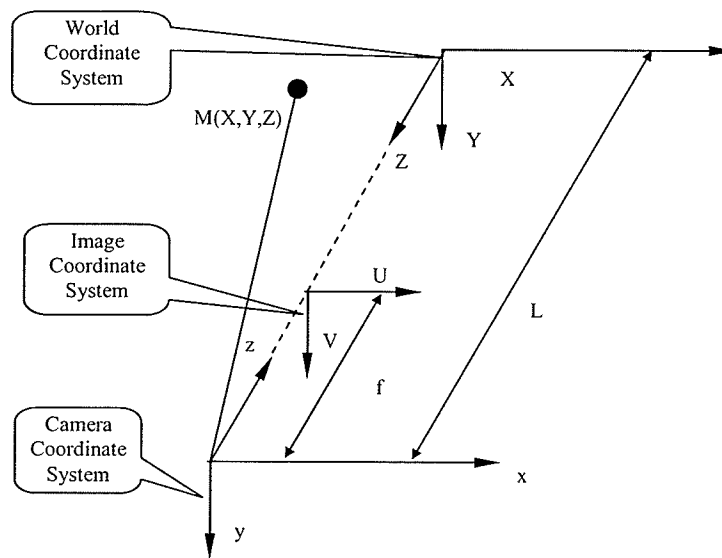


Figure 5.5 Coordinate systems for 3D coordinates calculation

5.3 Image-based parameter measurement methods

Based on the analysis of the FTP method, L , d and f/α should be obtained to calculate 3D coordinates of the objects. An image-based method to calculate these parameters is described in the following parts.

5.3.1 Helper pattern design

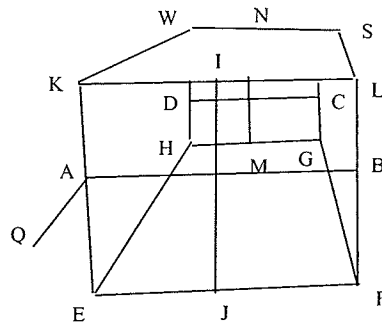


Figure 5.6 The helper pattern

The helper pattern is a special designed tool inspired by the research of Bénallal and Meunier (2002). It is used for a system construction and parameters (L , d and f/α) measurement. The pattern is composed of a box, a stick and two crosses as shown in Figure 5.6. The box is opened in the front (rectangle KLEF) and at the back (rectangle SWGH). The width, height and length of the box are known. One cross (line AB and IJ) is attached in front of the box and another (line CD and MN) is attached at the back. Both crosses are perfectly aligned. The stick (line AQ) is attached in front of the box and on the horizontal line of the cross (line AB). The length of the stick is known. In this research the helper pattern is used to calculate L , d and f/α using image-based methods.

5.3.2 Principle of the new method

There are three assumptions used in this method: (1) the pinhole model of a camera is used, (2) the distortion, zero-skew and unit aspect ratio in the image plane are not considered, and (3) the image is governed by laws of the projective geometry.

The camera needs to be oriented to the helper pattern so that the two crosses of the pattern are perfectly aligned together (only one cross can be seen in the image). Because both crosses are on parallel planes, the center point of the crosses in image planes is the intersection of optical axis of the camera with the image plane. The image plane is parallel to both cross planes.

The projector is set at a position so that: (1) the optical axis of the projector crosses with the optical axis of the camera at center point of cross AB-IJ (O''); (2) the line that passes through points P and O is parallel to the cross line AB; and (3) the cross ABIJ is on the reference plane as shown in Figure 5.7.

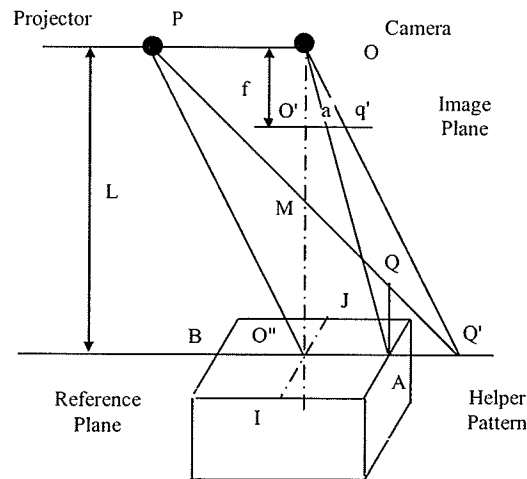


Figure 5.7 Geometry structures of the camera, the projector and the helper pattern

In Figure 5.7, a and Q' are the projective point of A and Q on the reference plane and q' is the projective point of Q' on the image plane. According to $\triangle OPM \sim \triangle MO''Q'$,

$\Delta Q'QA \sim Q'MO''$, $\Delta OO'a \sim \Delta OO''A$ and $\Delta OO'q' \sim OO''Q'$, the following equations can be obtained.

$$\frac{OP}{O''Q'} = \frac{OM}{MO''} \quad (5.9)$$

$$\frac{QA}{MO''} = \frac{Q'A}{O''Q'} \quad (5.10)$$

$$\frac{O'q'}{O''Q'} = \frac{OO'}{OO''} \quad (5.11)$$

$$\frac{O'a}{O''A} = \frac{OO'}{OO''} \quad (5.12)$$

$$O'q' = n \times \alpha \quad (5.13)$$

$$O'a = u \times \alpha \quad (5.14)$$

$$F_\alpha = f / \alpha \quad (5.15)$$

where n is the amount of pixels from O' to q' on the image; u is the amount of pixels from O' to a on the image; α is the size of a pixel on the image; f is the focal length of the camera.

Therefore the distance between the optical center of the projector and the camera can be calculated:

$$OP = \frac{OO'' \times O''A \times (n - u) - QA \times O''A \times n}{QA \times u} \quad (5.16)$$

Where AQ is the length of the stick; $O''A$ is a half of the width (AB) of the helper pattern.

In Equation (5.16), if the distance from the camera to the reference plane (OO'') could be obtained then OP can be calculated.

Figure 5.8 shows the geometry structure of the image and the helper pattern. According to $\Delta Oab \sim \Delta OAB$ and $\Delta Ocd \sim \Delta OCD$, following equations can be obtained.

$$\frac{O'a}{O'A} = \frac{OO'}{OO''} \quad (5.17)$$

$$\frac{O'd}{O''D} = \frac{OO'}{OO''} \quad (5.18)$$

$$OO'' - OO' = AD \quad (5.19)$$

$$AO'' = O''D \quad (5.20)$$

$$O'a = u \times \alpha \quad (5.21)$$

$$O'd = v \times \alpha \quad (5.22)$$

$$OO' = f \quad (5.23)$$

where u and v are the amount of pixels of line aO' and dO' on the image. AD is the length of the helper pattern. AO'' is a half of AB and AB is the width of the helper pattern. a , b , c and d are projective points of A , B , C and D on the image.

We can get:

$$OO'' = \frac{v \times AD}{(u - v)} \quad (5.24)$$

and

$$F_\alpha = \frac{f}{\alpha} = \frac{u \times OO''}{AO''} \quad (5.25)$$

Combining OO'' with Equation (5.15), OP can be calculated.

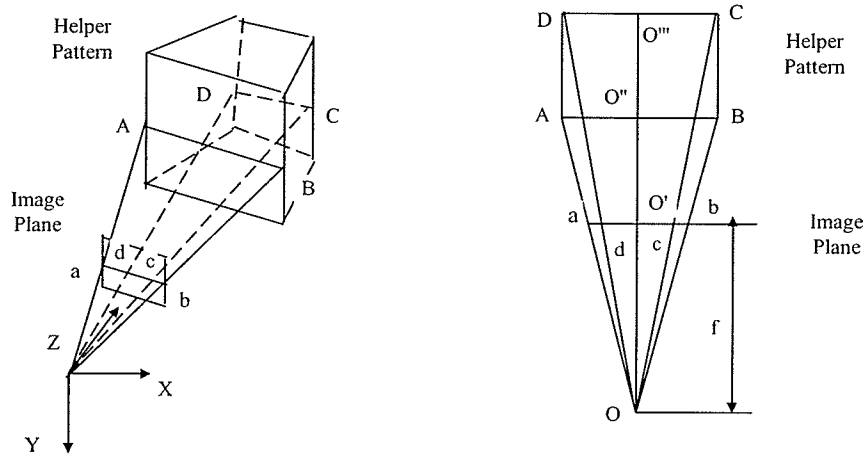


Figure 5.8 Geometry structure of the image and the helper pattern

5.4 An FTP-based 3D data acquisition system with the unified calibration

5.4.1 System hardware

The system layout is shown in Figure 5.9. According to the projection geometry of Figure 5.6, the optical centers of the projector and the digital camera are located at the same distance L from the reference plane, and d is the distance between them. A sinusoidal grating is generated by the computer and is projected on the object and the reference plane by the projector. It allows users to change the cycle time of the grating for FTP methods at a low cost. Images of the deformed grating and the object are captured by the digital camera and saved in the computer. The helper pattern is used for system construction and parameters measurement.

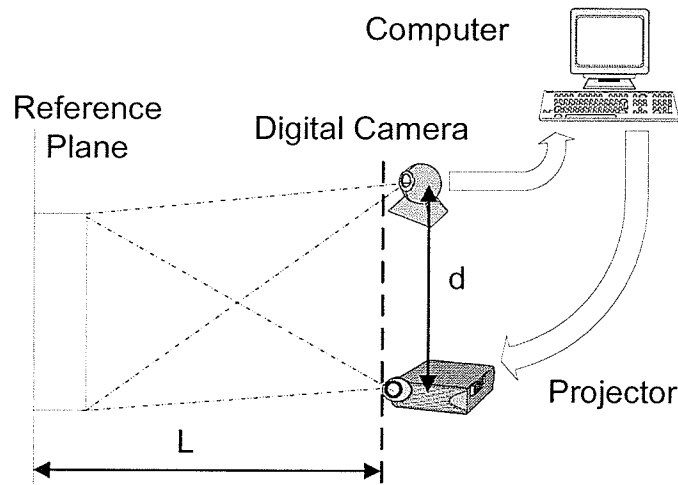


Figure 5.9 System hardware and layout

5.4.2 The working process of the system

The overall process of the FTP-based 3D data acquisition is shown in Figure 5.10 and is described as follows.

(1) The system hardware is set up based on the system structure. Parameters calculation obtains system parameters. The positions of the digital camera, the helper pattern and the projector meet the requirements described in Section 5.1. An image with the helper pattern is taken, the system parameters L , d and f/α can be calculated.

(2) Sinusoidal grating is generated by Equation (5.26).

$$I(x, y) = A + B \cos[2\pi f_{r_0} x + \alpha_i] \quad (5.26)$$

where $I(x, y)$ is the gray intensity of pixel (x, y) of the sinusoidal grating image; A is the average intensity of the image background; B is the intensity modulation; f_{r_0} is the fundamental frequency of the grating image; α_i is the angle of phase shift.

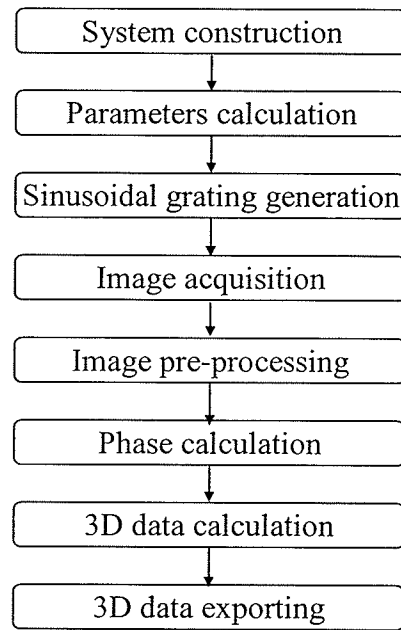


Figure 5.10 The overall process of the FTP-based 3D data acquisition

(3) Two images are required based on Equation (5.6). One is the reference-grating image, the other is deformed grating image. The reference-grating image is the grating image on the reference plane without an object in front of the reference plane.

(4) Grating image pro-processing is for removing the noise from acquired images. Low-pass filter image processing is used in this procedure.

(5) In phase calculation, images are computed by 1D Fourier Transform to obtain the Fourier spectra. Then the spectra are filtered to obtain the fundamental component with a mid-pass filter function. Finally, the inverse Fourier transform is applied to the fundamental component to obtain $g(x,y)$ and $g_0(x,y)$, the phase can then be obtained using Equation (5.6).

(7) Based on the phase information, 3D coordinates of data points on the object are calculated. The algorithm is described in Section 5.2.

(8) The 3D data of the object obtained in Step (7) are the point clouds and they are output to CAD systems to build the 3D model.

5.5 Experiments and discussions

5.5.1 Experiments setup

The layout of the FTP-based 3D acquisition system is shown in Figure 5.9. In this experiment, the projector is an EIKI LC-7000 projector and the resolution of the projector is 1024 x 768 pixels. The digital camera is SONY FDMavica and the image size used is 1024 x 768 pixels. FTP algorithms are developed using MATLAB. The reliability-guided algorithm is used for the phase unwrapping (Su and Chen, 2004). A prototype of the helper pattern is built and the dimension of the helper pattern is shown in Figure 5.11(a). A holder is used as an example in the experiment. Figure 5.11 (b) is the original image of the holder.

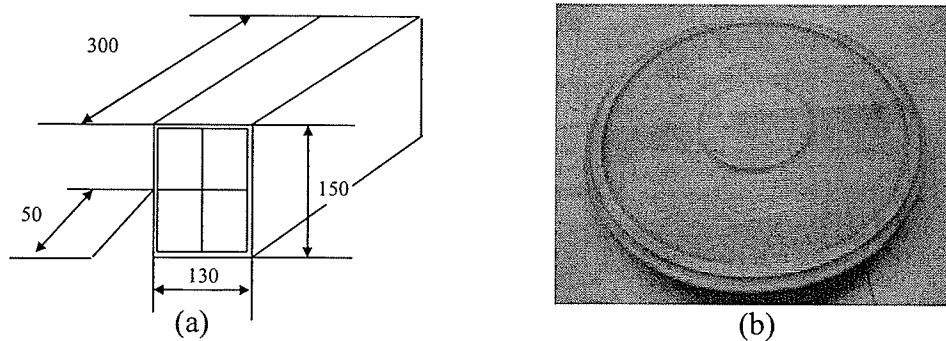


Figure 5.11 (a) The dimensions of the helper pattern; (b) Original image of the holder

5.4.2 Experimental results

In this experiment, the first step is the system construction with the aid of the helper pattern. The hardware layout is shown in Figure 5.9. Figure 5.12 is an image of the helper pattern taken after the system construction. In Figure 5.12, the centre point (O') of the cross in the image of the helper pattern is the original point of the coordinate system where $x=0$, $y=0$. The distances between O' and a , d , a' , q' are measured in the image of the pattern.

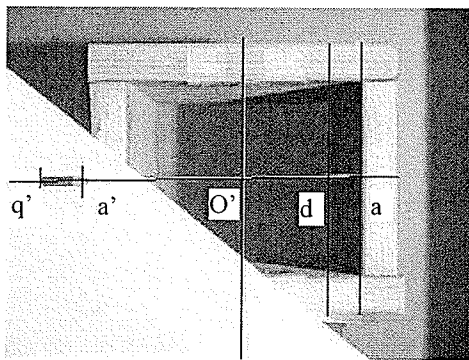


Figure 5.12 The image of the helper pattern

Parameters of the system are computed by Equations (5.23), (5.24) and (5.15). The result is $L=851.35\text{mm}$, $d= 208.97\text{mm}$ and $f/\alpha = 1590.68$. Figure 5.13 (a) is the sinusoidal grating image of eight pixels per cycle that is generated by the computer and the size is 1024 x768 pixels.

Figure 5.13 (b) shows the picture of a deformed grating image. The straight grating lines in Figure 5.13 (a) serve as the reference signal for determining absolute phase values to be converted into a height distribution. Figure 5.14 shows the recovered shape of the holder.

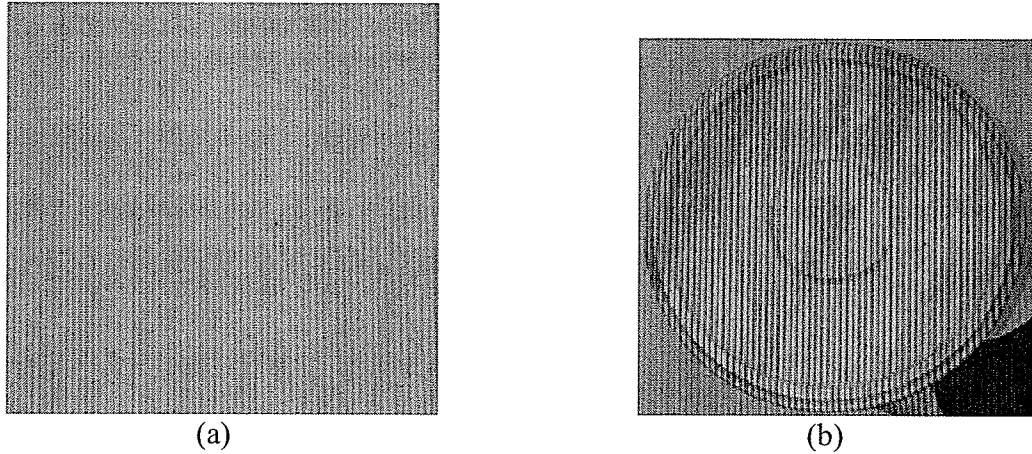


Figure 5.13 (a) Sinusoidal grating image (b) Deformed grating and the holder

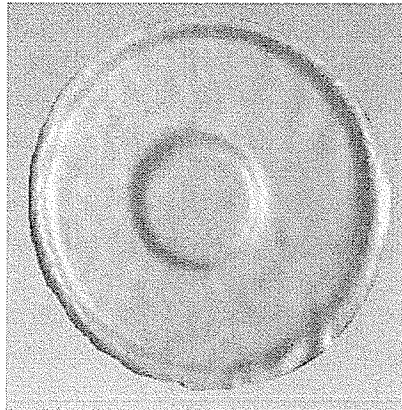


Figure 5.14 The recovered shape of the holder

Figures 5.15 and 5.16 show examples of the holder's profile obtained by CMM and the FTP method. The profile is obtained by cutting the holder along a diameter of the holder.

Figures 5.15 and 5.16 are drawn using Microsoft excel. In Figure 5.15, the maximum distance of top and bottom of the holder is $(72.2101 - 66.3307) = 5.8794$ mm. In Figure 5.16, the maximum distance is 6.4 mm. The average error of the distance from the top to the bottom of the holder is about 8%. But the shape of two profiles is the same.

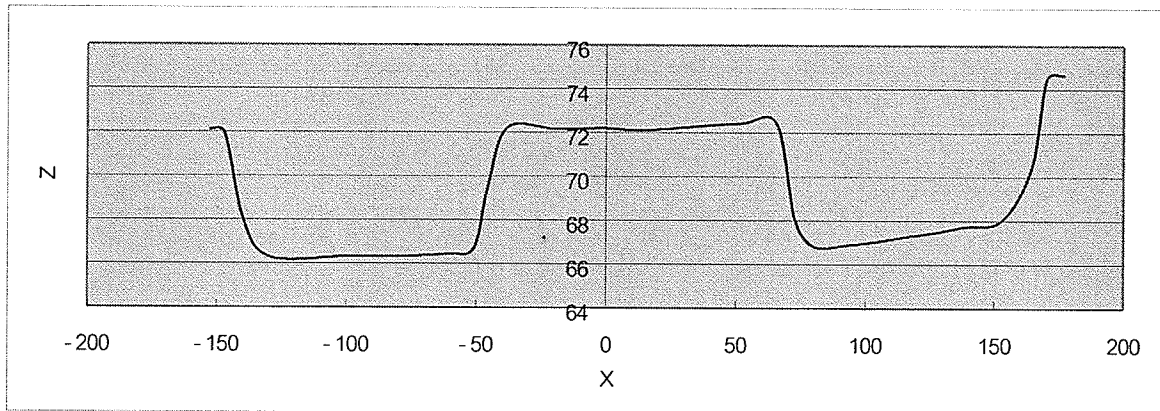


Figure 5.15 Profile of the holder that is measured by CMM

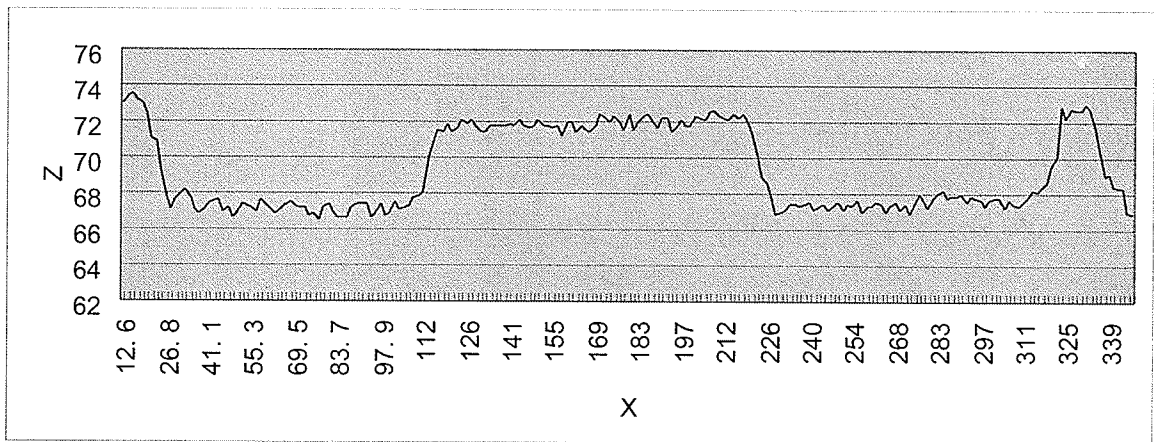


Figure 5.16 Profile of the holder that is obtained by FTP

5.5.3 Discussions

In Equations (5.23) and (5.24), the length of the pattern is used to compute the distance. Not only is the center point of the cross used as original points of the coordinate system to measure pixel distance of the object, but also the center point is used for orientating the camera. Therefore this method is sensitive to the accuracy of the helper pattern. In Figure 5.11, the boundary of the helper pattern on the image is composed of 2 or 3 pixels. An error of 1 pixel on the edge detection can generate errors. Therefore this method is sensitive to the

accuracy of edges or points detection on the image. The alignment of the optical axis requires some accurate tuning mechanics.

A comparison of the unified calibration method and other calibration methods is shown in Table 5.1. The height calibration and the plane calibration are processed in one step. There is no need to move the helper pattern. The parameters calculation is easy as only similar triangles method is used.

Table 5.1 A comparison of the unified calibration method and other calibration methods

No.	Unified calibration	Other calibration methods (Hu <i>et al</i> , 2003; Guo <i>et al</i> , 2005; Zhang <i>et al</i> , 2005; Takeda and Mutoh, 1983)
1.	One image with the helper pattern is needed. The height calibration and the plane calibration are processed using the image.	A series of images with calibration rig are needed. The height calibration is completed by pure fringe images and the plane calibration is processed using images of the calibration rig.
2.	Calibration process is simple. The helper pattern is at one fixed position in the calibration procedure.	The calibration rig is moved to different positions in the calibration procedure. The position of the rig has to be measured accurately.
3.	Only similar triangles method is used to calculate the parameters of the system. The calculation is simple.	Least-square algorithm and linear interpolation algorithm are used to calculate the parameters. The calculation is time-consuming.

Chapter 6

Correlation-based phase unwrapping in FTP methods

A new phase unwrapping algorithm based on correlation for FTP methods is presented in this chapter. The overview of the new phase unwrapping algorithm is introduced first. Then the 1D phase unwrapping algorithm and the reliability-guided phase unwrapping algorithm are discussed. After that a correlation-map function is proposed to calculate the reliability of the fringe image. The correlation-map function is used as a guide to find the optimized phase unwrapping path in the correlation-based phase unwrapping algorithm. The experimental results are shown at the end of this chapter.

6.1 Introduction

A correlation-based phase unwrapping method is proposed in this research to avoid choosing the width of the filter window for phase unwrapping in FTP methods. The reliability of the phase data is calculated by a correlation-map function. It simplifies the procedure of phase unwrapping for the FTP method. In the method, phase-shifted sinusoidal fringe images are generated by a computer with phase shift. A deformed fringe image is obtained by the FTP method. The correlations between the computer-generated fringe images and the deformed fringe image are calculated by the correlation-map function. The value of the correlation-map function is higher in areas of smooth surface than that in areas of height discontinuity, shadow and speckle-like noise. Therefore the correlation-map function is related to fringe

quality. Starting from a pixel with the maximum value of the correlation-map function, the unwrapping procedure is guided by the value of the correlation-map function from the pixel with high fringe quality to the pixel with low fringe quality. The error of the phase unwrapping is limited to local minimum areas.

6.2 1D phase unwrapping algorithm

The 1D phase unwrapping algorithm scans the wrapped phase image obtained by FTP methods from the top to bottom line by line. For each line, the first phase value in the line is recorded. The phase value of its neighbour is then compared with the value. If the difference between the two values is greater than π or less than $-\pi$ then $2K\pi$ is added to the phase value. K is incremented by 1 when there is a phase jump. The process of the algorithm is shown in Figure 6.1. The method treats the noise as a phase wrap and update the remaining phase values accordingly. The error will be accumulated through the entire unwrapped distribution and the final result is not accurate.

Figure 6.2 shows a phase distribution with two "spot noise", and Figure 6.3 shows the phase distribution after phase unwrapping using this method.

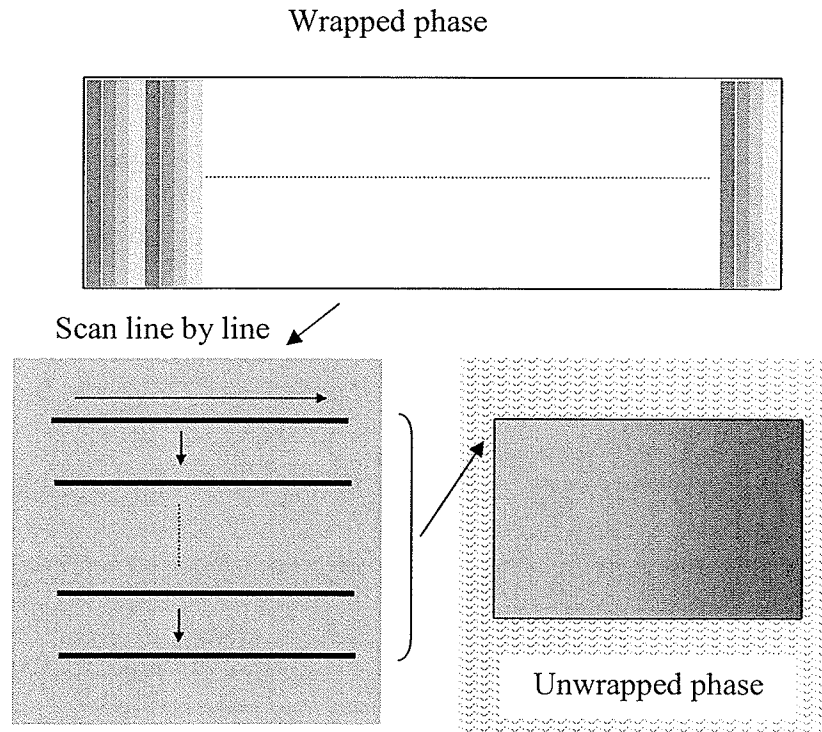


Figure 6.1 The process of 1D phase unwrapping algorithm

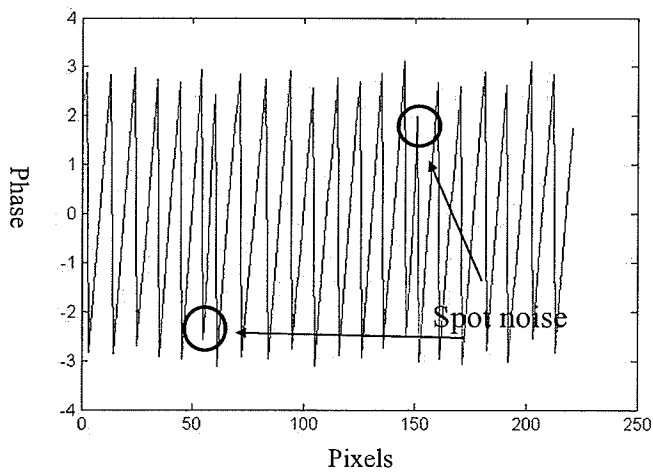


Figure 6.2 A phase distribution with two “spot noise”

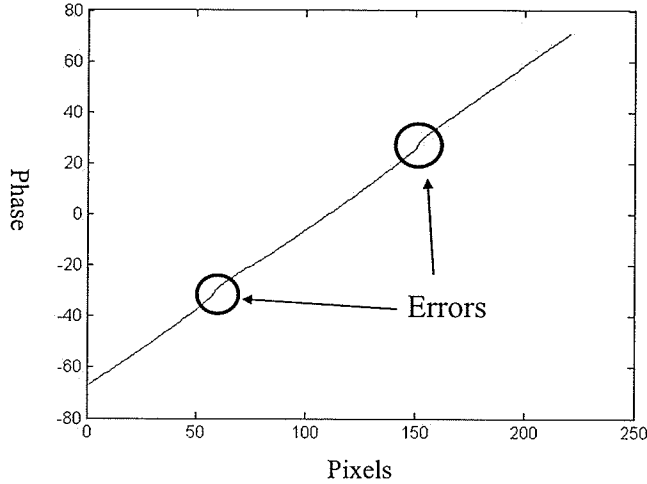


Figure 6.3 The phase distribution after phase unwrapping

6.3 The reliability-guided phase unwrapping algorithm

For the FTP method, the modulation function as a reliability parameter can be calculated by the following equation:

$$M(x, y) = |\hat{g}(x, y)| = \sqrt{[\text{Im}(\hat{g}(x, y))]^2 + [\text{Re}(\hat{g}(x, y))]^2} \quad (6.1)$$

where $\hat{g}(x, y)$ can be obtained by Equation (5.2).

The reliability-guided phase unwrapping algorithm computes the modulation $M(x, y)$ of the deformed grating image (Li *et al*, 1997). The phase unwrapping starts from the pixel with maximum modulation and unwraps the phase along a path from the pixel with a higher modulation to the pixel with a low modulation. The process of unwrapping is shown in Figure 6.4. The advantage of this approach is that it can always unwrap phase in local minimum areas therefore the error propagating of phase unwrapping is avoided.

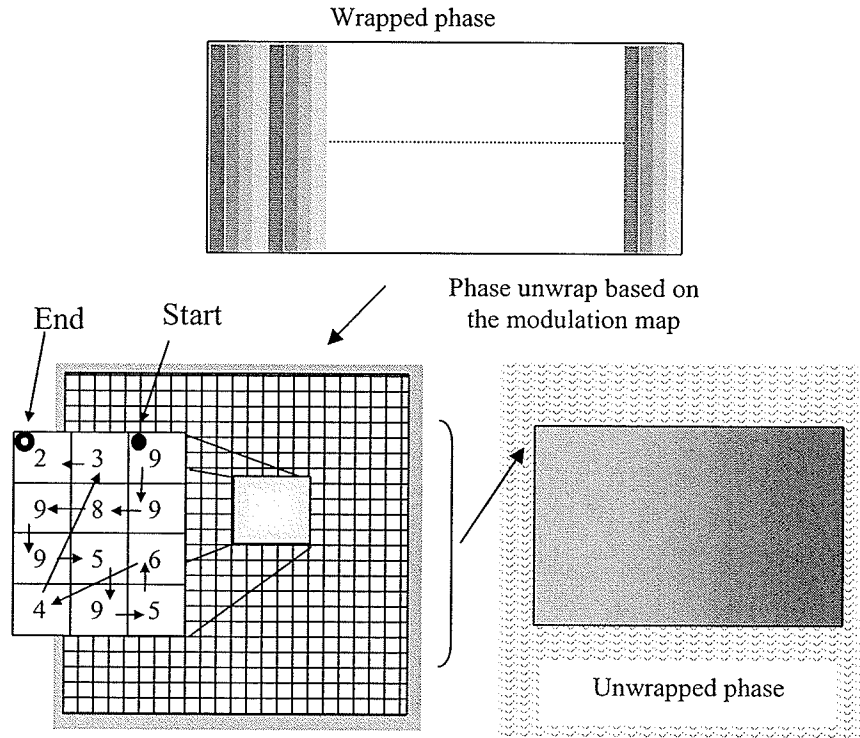


Figure 6.4 The process of reliability-based phase unwrapping algorithm

6.4 Analysis of the correlation-based phase unwrapping method

In image processing, correlation is a standard method of estimating the degree to which two series are correlated. If two images are captured, one is the source image $g_0(x, y)$, the other is the template image $g(x, y)$. These two images are same size ($M \times N$). The correlation between two images is calculated by Equation (3.16) in Chapter 3. For any pixel of (x, y) inside $g(x, y)$ and $g_0(x, y)$, two image regions of size $s \times t$ around the pixel are put into Equation (3.16) to obtain one correlation value of $c(x, y)$.

A correlation map is calculated by the correlation method to measure the reliability of the wrapped phase. The correlation-map function is defined as:

$$CM(x, y) = \sum_{\theta=0}^{\pi/2} \{Corr[I_{source}, I(\theta)] - Corr[I_{source}, I(\theta + \pi)]\} \quad (6.2)$$

Where I_{source} is the image region of size $s \times t$ around the pixel of (x, y) inside the deformed fringe image. $I(\theta)$ is the image region of size $s \times t$ around the pixel of (x, y) inside a computer generated fringe image. $I(\theta) = I_0 \sin(\varphi(x, y) + \theta)$. Where I_0 is the basis intensity, $\varphi(x, y)$ is phase function which is computed by the period of deformed fringe image. θ is the initial phase. $I(\theta + \pi)$ is $I(\theta)$ with the initial phase plus π . $Corr[I_{source}, I(\theta)]$ and $Corr[I_{source}, I(\theta + \pi)]$ are the correlations of $I_{source}, I(\theta)$ and $I_{source}, I(\theta + \pi)$.

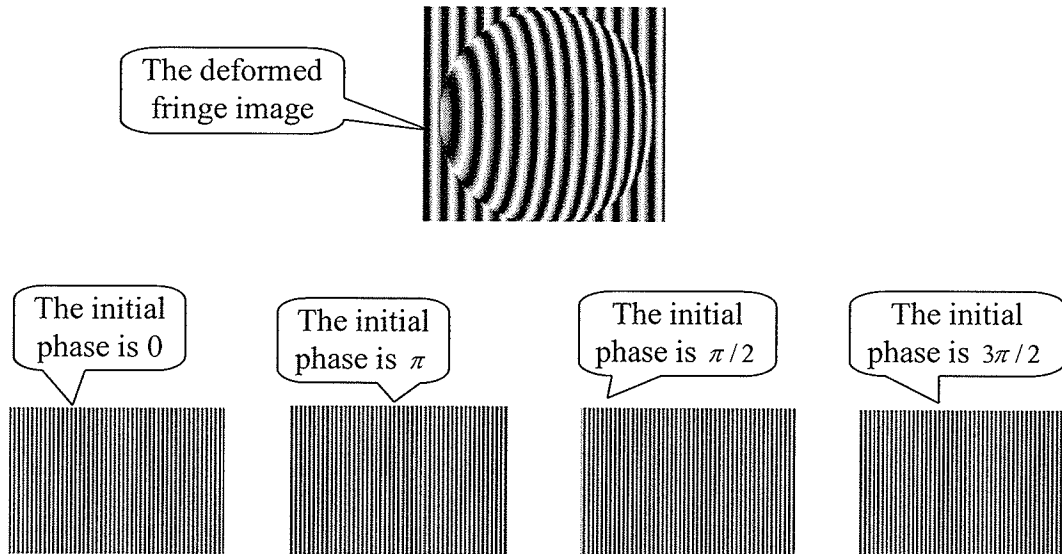


Figure 6.5 The source image and four computer-generated fringe images

The procedure of calculating the correlation map is as follows:

- 1) Generate four fringe images by a computer as shown in Figure 6.5. The initial phase of the four images are $0, \pi, \pi/2$ and $3\pi/2$.

- 2) Compute the correlation of the source image and four images for every pixel from top left to bottom right of the source image.
- 3) Obtain four correlation maps of four images as, $Corr[I_{source}, I(0)]$, $Corr[I_{source}, I(\pi/2)]$, $Corr[I_{source}, I(\pi)]$ and $Corr[I_{source}, I(3\pi/2)]$.
- 4) Compute the final correlation map by Equation (6.2).

The effect of the correlation-map function is in Figures 6.6 and 6.7 with the results of computer simulation.

The sinusoidal fringes are generated by Equation (6.3) in the computer simulation.

$$I(x, y) = A + B \sin[2\pi s_{r0}x + \alpha_i] \quad (6.3)$$

where $I(x, y)$ is the gray intensity of pixel (x, y) of the sinusoidal fringe image; A is the average intensity of the image background; B is the intensity modulation; f_{r0} is the fundamental frequency of the fringe image; α_i is the angle of initial phase.

Figure 6.6 shows that the value of the correlation-map function is decreasing along with increasing of the intensity of the image background from left to right. Then the random noise is added to the sinusoidal fringes. Figure 6.7 shows the relationship of the correlation-map function with the intensity modulation and the intensity of the image background in the environment of random noise. The correlation-map function is lower when the intensity of the background is higher and intensity modulation is lower.

The correlation-map function is proportional to intensity modulation. In the areas of local shadow and abrupt discontinuities, the intensity of image background is higher and the intensity modulation is lower. The value of the correlation-map function in the areas of local shadow and abrupt discontinuities is lower than the value in the other areas. Therefore, the

correlation-map function can be used to identify the areas of local shadow and physical discontinuities on the object's surface.

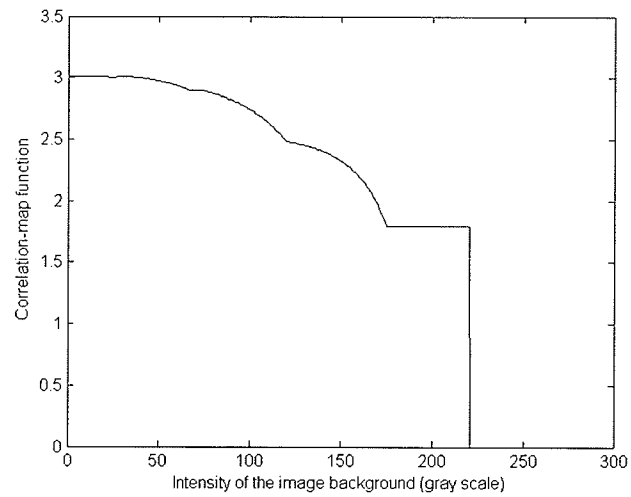


Figure 6.6 The relationship of the correlation-map function with the intensity of the image background

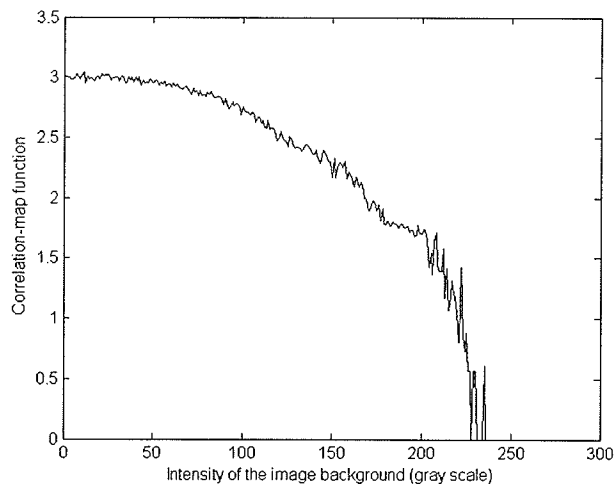


Figure 6.7 The relationship of the correlation-map function with the intensity of the image background with noise

6.5 The proposed algorithm for the correlation- based phase unwrapping method

A flow chart of the proposed algorithm for the correlation-based phase unwrapping is presented in Figure 6.8. A data queue and a binary mask are built in the algorithm. The binary mask is used to identify the wrapped and unwrapped points. All unwrapped pixels are placed in the data queue in order by the value of the correlation-map function. The detailed steps of the algorithm are as follows:

- 1) Compute the wrapped phase by the FTP method, and compute the correlation map by Equation (6.2). The size of the correlation map is the same as the matrix of the wrapped phase.
- 2) Find the maximum value from the correlation map, the corresponding pixel in the matrix of the wrapped phase is the starting point of phase unwrapping. Then, the corresponding point in the binary is marked as 1. It means that the point has been wrapped. All initial values in the binary mask are set to 0, representing that the corresponding phase is not unwrapped. The process of this step is shown in Figure 6.9.
- 3) Put four neighbour points of the starting point into the data queue, and order them according the value of the correlation-map function from the highest to the lowest. The pixel with the maximum value is put at the top of the queue.
- 4) Pick the pixel with the maximum value from the top of the queue and process its phase unwrapping on the basis of the starting point. If the difference between this point and the starting point is more than π ; the natural phase of this point equals to its wrapped phase subtracting 2π . If the difference is less than $-\pi$; the natural phase equals to its wrapped

phase adding 2π . After the phase unwrapping is done for the point, the corresponding point in the binary mask is marked as 1.

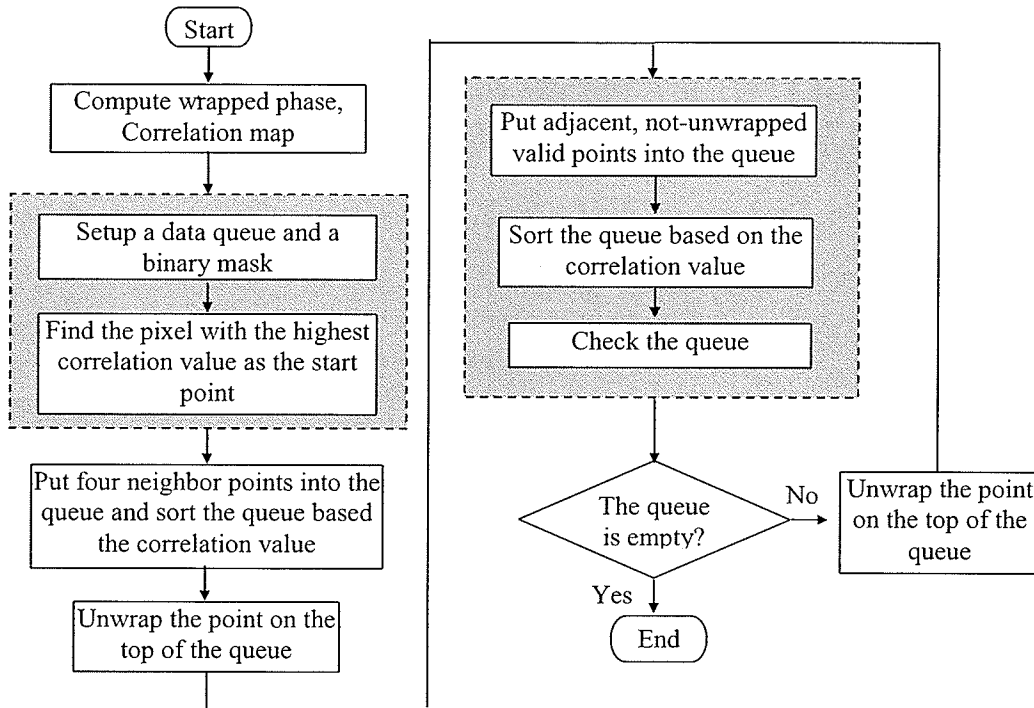


Figure 6.8 The proposed algorithm of the correlation based phase unwrapping method

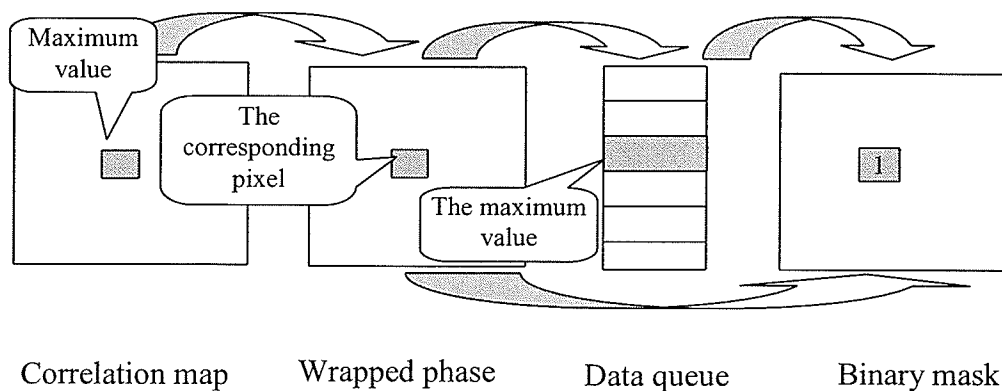


Figure 6.9 The process of the phase unwrapping

5) Put its four neighbour points which have not been unwrapped into the queue, and order them from highest to lowest. Remove the point with the maximum value from the queue, and repeat Step 4).

6) Repeat Steps 4) and 5) until the queue is empty, which means that all the points have been unwrapped, phase unwrapping is finished.

6.6 The experiments

A plastic kettle is measured in the experiment. The testing system layout is shown in Figure 6.10. The optical centers of the projector and the digital camera have the same distance L from the reference plane, and d is the distance between them. A sinusoidal fringe is generated by the computer. It is projected on the object and the reference plane by a projector. Images of the deformed fringe and the object are captured by the digital camera and saved in the computer. In the experiment, the projector used is an EIKI LC-7000 projector and the resolution of the projector is 1024 x 768 pixels. The digital camera is SONY FDMavica and the resolution of the camera is 1024 x 768 pixels.

The deformed fringe pattern is displayed in Figure 6.11. Four fringe images generated by the computer are shown in Figure 6.12. The initial phase of the images are 0 , π , $\pi/2$ and $3\pi/2$. Figure 6.13 shows the wrapped phase obtained after the phase calculation by the FTP method. The modulation map and the correlation map are shown in Figure 6.14. The dark areas in the images are the lowest modulation or correlation area. In both images, the dark areas are at positions of shadow areas or sparkle areas in the deformed fringe image as shown in Figure 6.11. Therefore, the phase reliability can be recognized from the correlation value. The higher value of the correlation-map function means the higher fringe quality.

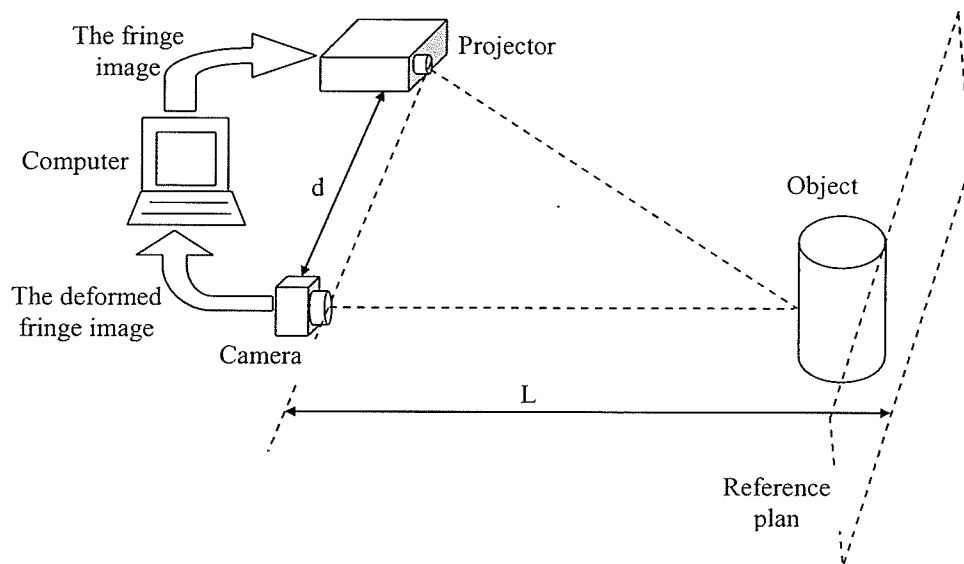


Figure 6.10 The layout of the experimental system

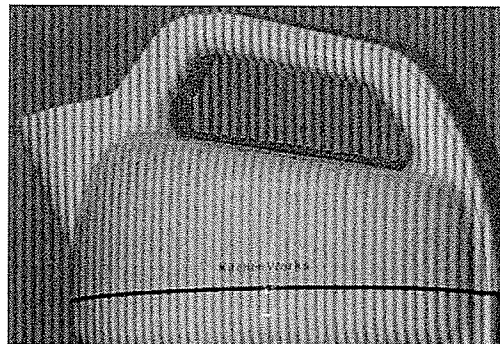


Figure 6.11 The deformed fringe pattern on the kettle

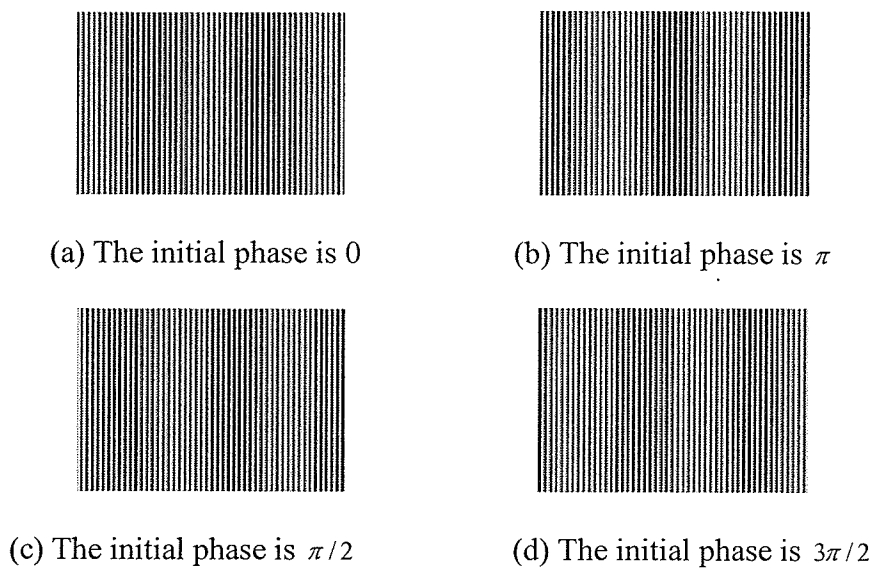


Figure 6.12 Computer generated fringe images

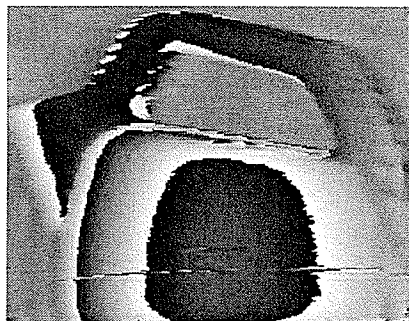


Figure 6.13 The wrapped phase obtained by FTP method

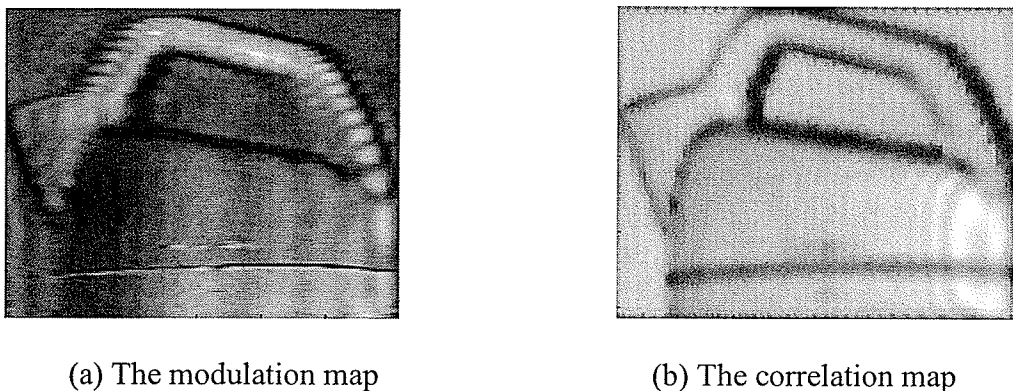


Figure 6.14 The modulation map and the correlation map for phase unwrapping

Figure 6.15 show the result obtained by using the 1D phase unwrapping algorithm. Because the errors propagating can't be avoided, many errors are happened. The 3D shape of the kettle can't be constructed correctly by this method.

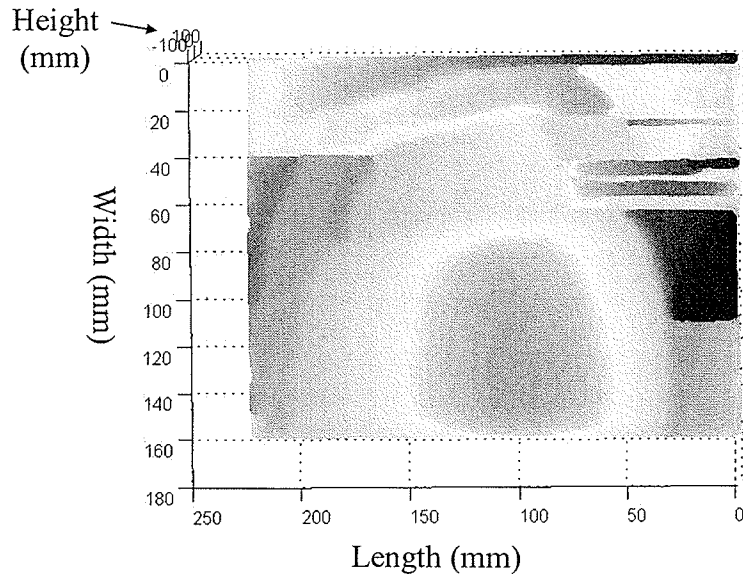


Figure 6.15 The result obtained by using the 1D phase unwrapping algorithm

The reconstructed 3D models of the kettle obtained by the modulation method and the correlation-based method are compared with the 3D model obtained by a 3D laser scanner. The dimensions of the kettle is 230 mm x 180 mm x 160 mm (length x width x height).

The comparison of the modulation method with the laser scanner is shown in Figure 6.16.

Figure 6.17 is the comparison of the correlation-based method with the laser scanner. Figure

6.18 shows the comparison result of the modulation method with the laser scanner, but the 3D model of the kettle is obtained by the modulation method with a wider filtering window.

The errors are shown in different gray-scales. The error in the area ① is 2 mm, in the area ②

is 1 mm and in the area ③ is 3 - 5 mm. The area ④ includes the mouth and the handle of the kettle. The error is 1 – 9 mm. The whole kettle is properly obtained except big errors in the area ④.

The area ⑤ is the bottom of the kettle in Figure 6.18. It cannot be reconstructed correctly as a wider filter window is used in the modulation method, the higher-order spectrums and the zero spectrums overlap the fundamental spectrums. The path of the phase unwrapping goes through an unreliable area and transfers the errors in the area ⑤, the phase in the area cannot be unwrapped correctly.

Comparing with the modulation, the correlation-map function can be used as a parameter to indicate the reliability of the fringe image without choosing the width of the filter window in FTP method. It simplifies the procedure of phase unwrapping for the FTP method.

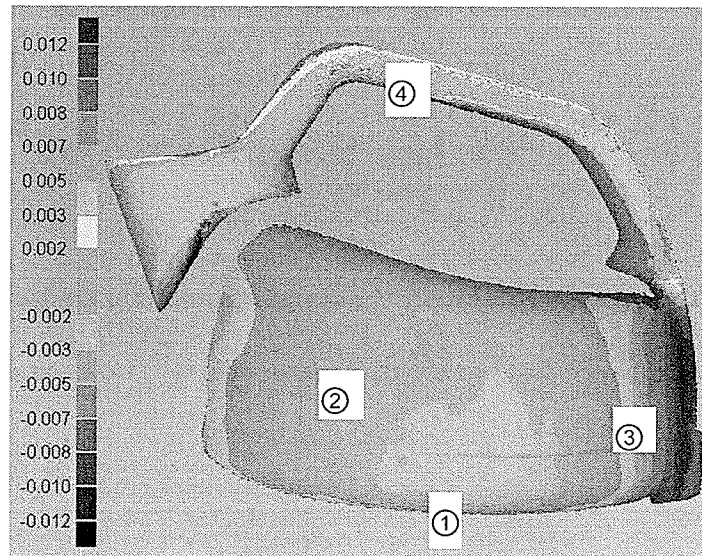


Figure 6.16 The comparison result obtained by the correlation method

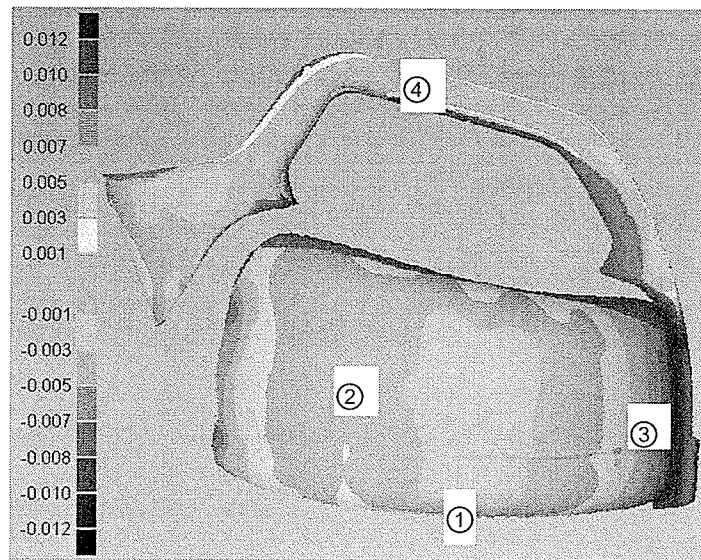


Figure 6.17 The comparison result obtained by the modulation method

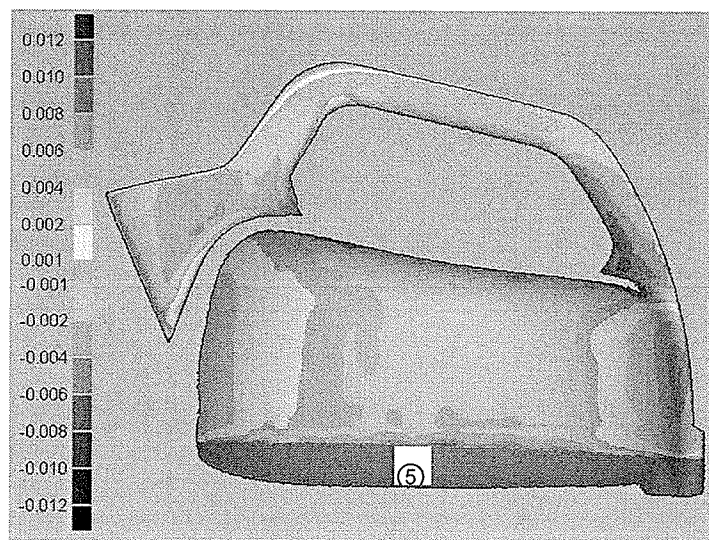


Figure 6.18 The comparison result obtained by the modulation method with a wider window

Chapter 7

The image-based 3D ice detection system

An application of the image-based 3D data acquisition methods is presented in this chapter. This research proposes a novel method to monitor ice accretions on power transmission lines with an image-based 3D detection technique. The introduction of the image-based 3D ice detection system is presented first. The principle of the proposed method and the development of the ice detection support system are then discussed. The experiments on the 3D ice detection algorithm, tested in a laboratory and application in a real environment are presented at the end of this chapter.

7.1 Introduction

The image-based 3D ice detection system aims to monitor the ice accumulation on power transmission lines. The system can detect the ice shape and measure the ice thickness continuously when the ice grows on power transmission lines. If the ice thickness is greater than a defined threshold an alarm message will be sent to users. When the alarm is received, a decision can be made based on ice images in order to remove ice on power transmission lines. The research in the literature review all focuses on the general solution of feature detection and feature matching in image processing. None of them has been used to monitor the ice accumulation in real environments. In this research, the proposed method will combine the existing methods in a practical way to provide a useful solution to find the

corresponding points in two ice images. Detecting and matching points in two ice images is very difficult. As the ice is transparency or semi-transparency it is easy to be affected by background noise. The noise may decrease the gradient to deteriorate the performance of feature detection. The smooth surface of the ice also increases the difficulty in finding the corresponding points on the ice images. But the ice thickness calculation will only need the 3D information of the top and bottom edges of the ice, not all of the surface. The interested corresponding points will only be located on the ice edge. These points will be used to calculate the maximum ice thickness along a power transmission line. The proposed method uses two ice images of the same power transmission line that are taken by two cameras to calculate ice thickness. The rotation, translation and intrinsic parameters of two cameras are obtained by a calibration process. The thicknesses of the ice can be obtained after the ice on the power transmission lines is identified. A multi-scan edge detection method is applied for the ice detection. After ice detection, peak points on the ice edges can be obtained. Epipolar line and correlation methods are used to find the corresponding points of these peak points in the two images. The 3D coordinates of these points can then be calculated using the corresponding points. The ice thickness is the distance between two peak points of edges. The accurate ice thickness can be obtained as the influence from vibration of transmission lines is eliminated by 3D ice information.

Figure 7.1 shows a framework of the proposed system. The system includes three parts:

- 1) The image capture hardware: two digital cameras are used in this system. The processing computer can trigger these two cameras to take ice images at the same time. The captured images are uploaded automatically to the processing computer through USB (Universal Serial Bus) hardware interface.

2) The processing computer: the ice images are analyzed using image processing methods and the ice thickness can be calculated in this computer. The alarm message and ice information can be sent to the base station using wireless network technology.

3) The base station: the alarm message is automatically accepted through wireless network and is displayed to users. It has functions to download present status images and data for a further analysis. This allows users to make the right decision for removing ice on the power transmission lines.

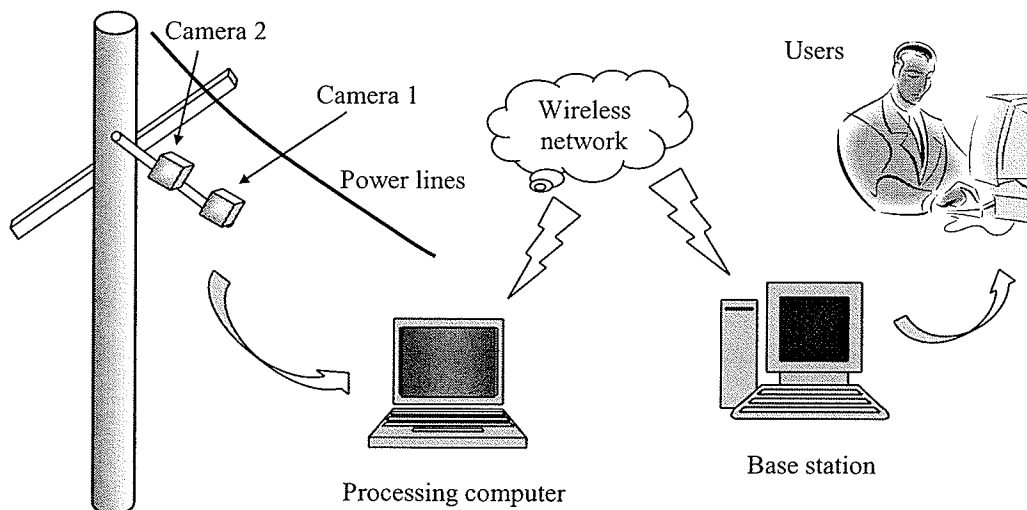


Figure 7.1 The framework of the proposed 3D ice detection system

This research focuses on the software development. Based on the framework of the system, the software includes two parts: one is ice detection software and the other is system support software.

The objectives of the ice detection software are:

- Connecting with digital cameras to download images for processing.

- Automatically transferring images from JPEG (Joint Photographic Experts Group) format to BMP (Bitmap) format and vice versa to meet the need of image processing, storage, retrieval and the data transfer.
- Detecting ice accumulation on power lines. The iced power lines will be detected and the thickness of ice will be calculated.
- Saving ice thickness data and ice profile for further analysis.

The objectives of the system support software are:

- Server software for sending commands from users' office to the ice detection software. Users can check current status of the ice detection system and history data without leaving their office.
- Client software for communicating with the server software. The client software receives commands from the server software and executes the commands for checking ice status or history data.

7.2 The 3D ice detection method

The photogrammetry method is used to measure the ice thickness. In photogrammetry method, the 3D coordinates of an object point are calculated by using corresponding points in two images. Therefore the most important step in this method is the point matching algorithm which finds the same physical point in two ice images. As the surface of the ice is smooth without special features to be used for matching points in the ice images, the feature-based and area-based points-matching method are combined in this research to provide a solution for the corresponding points in two ice images.

The feature information in the ice images, epipolar geometry and the top and bottom edges of ice, are used to find the search area for a corresponding point. The correlation method is used to find the precise position of the corresponding point. A work flow of the point matching is shown in Figure 7.2. The epipolar line is computed after a point is given by users. The search area is composed by a group of points around the intersection of epipolar lines and edges. The cross-correlation method is used to calculate the similarity score (Gonzalez and Woods, 2002). In the search area, if the similarity score at one point is greater than a defined threshold then the point is the matching point. An example is shown in Figure 7.3.

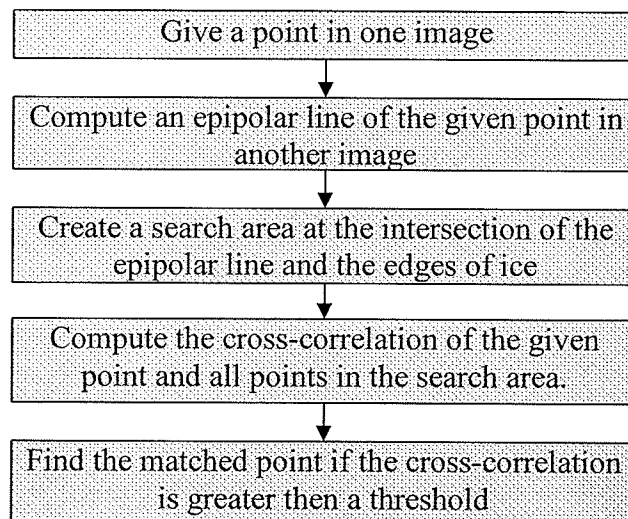


Figure 7.2 The workflow of points matching

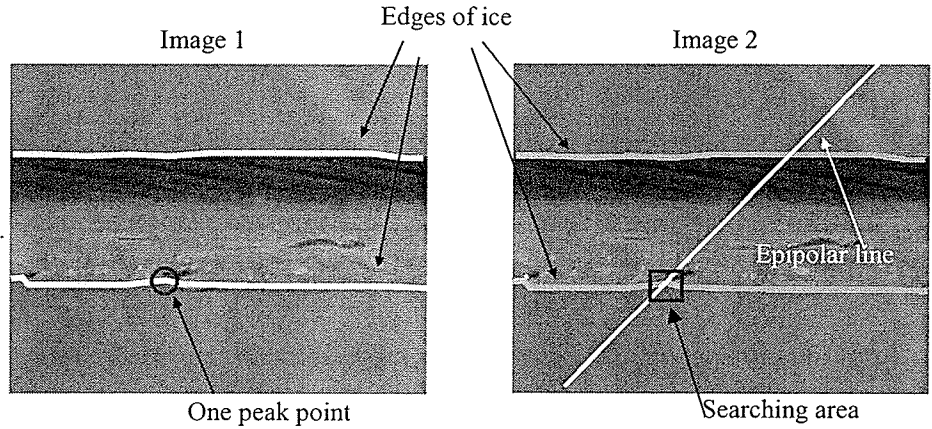


Figure 7.3 Feature-based and area-based points matching method

Figure 7.4 shows a flow chart of the algorithm of the 3D ice detection system. The major steps involved in the process of the algorithm are system calibration, image data acquisition and ice thickness calculation.

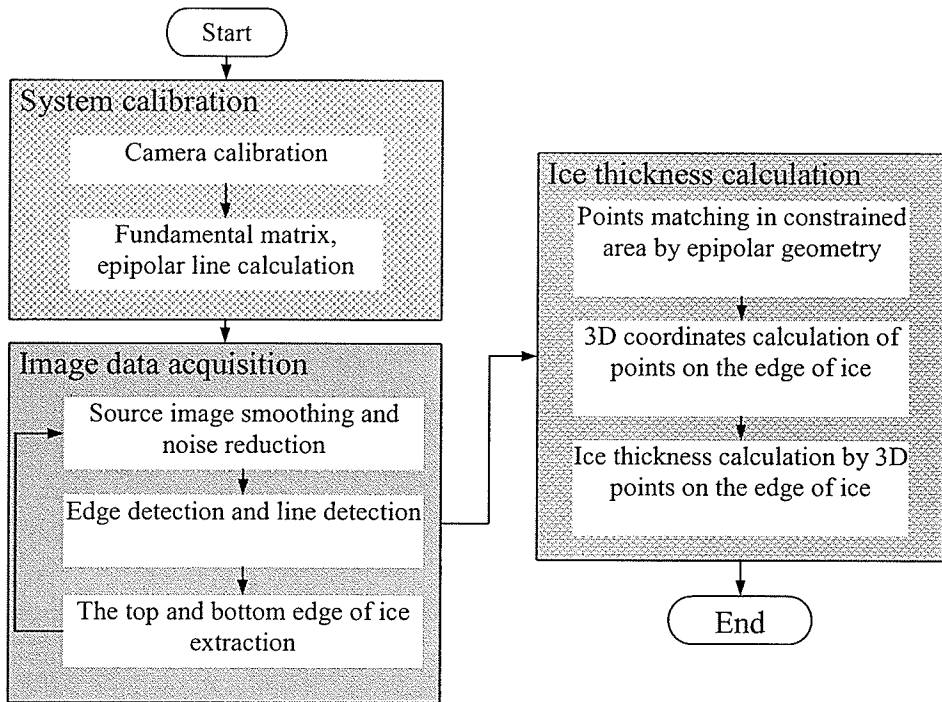


Figure 7.4 Flow chart of the algorithm of 3D ice thickness acquisition

In the system calibration, the camera calibration and epipolar geometry calculation are performed. Since the novel calibration technique has been discussed in Chapter 4, the details about the camera calibration will not be described in this section. Two types of parameters associated with cameras will be determined in camera calibration including intrinsic parameters and extrinsic parameters. The camera projection matrix is obtained as follows:

$$P = K[R^T - R^T l] \quad (7.1)$$

Epipolar geometry is determined by estimating the fundamental matrix which describes the projective transformation between the points contained in images. One of the main problems associated with this approach is the fact that the fundamental matrix is very sensitive to errors of the point location. In this research the problem is solved by using two checkerboard patterns. The use of the checkerboard pattern provides accurate locations of corresponding points in two images because all corresponding points are corners of black and white squares on checkerboard pattern and can be easily extracted in both images. A 8-points algorithm is used to calculate fundamental matrix (Hartley and Zisserman, 2004). The epipolar line l' can be calculated after the fundamental matrix is obtained.

$$l' = Fx \quad (7.2)$$

Where F is the fundamental matrix and x is a point on an image. The epipolar lines will be used in points matching.

In the image data acquisition, top and bottom edges of the ice on power transmission lines are extracted from 2D images. A multi-scan method is implemented in this research and the multiple image-scanning are included in the method. Each image-scanning includes 3 steps: image smoothing, edge detection and edge connection (Gonzalez and Woods, 2002). The iteration numbers of an image-scanning are determined by experiments. After the image-

scanning, top and bottom edges of ice on transmission lines are obtained by searching the two longest lines in the images. The intersections of a vertical line with the top and bottom edges are called peak points. Four pairs of peak points are selected as the distances between the top and the bottom edges are the first four maximum. A pair of peak points is shown in Figure 7.5.

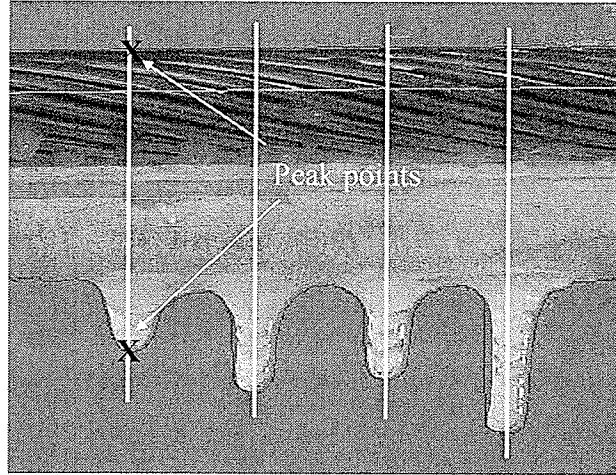


Figure 7.5 Peak points on an ice image

In the ice thickness calculation, the point matching algorithm is used to find the corresponding points of the peak points. The 3D coordinates of matching points are computed based on the triangulation algorithm (Hartley and Zisserman, 2004). After points matching, the following equations can be obtained:

$$\begin{aligned} x &= PX \\ x' &= P'X \end{aligned} \quad (7.3)$$

Where x and x' are the correspondent points in two ice images obtained in point matching algorithm. P and P' are projection matrix of two cameras. X represents the 3D coordinates of a point on outline of the ice edge. P^{iT} is the rows of P and P' . The system of linear equations is as follows:

$$\begin{bmatrix} xP^{3T} - P^{1T} \\ yP^{3T} - P^{2T} \\ x'P^{3T} - p^{1T} \\ yP^{3T} - P^{2T} \end{bmatrix} X = 0 \quad (7.4)$$

The 3D coordinates of peak points X can be obtained by Equation (3.44). Therefore, the ice thickness can be obtained from the distance between two peak points on the widest outline of the ice edge detected.

7.3 Development of the ice detection support system

To support the 3D ice detection method working in real environments, a support system is developed. As shown in Figure 7.6, client/server architecture on wireless networks is used in the system. The system consists of a server program, a client program and the ice detection program. The functions of the ice detection program are to analyze a captured ice image to obtain the ice thickness. The core part of the ice detection system has been discussed in Section 7.2. The functions of the server program are to send commands to the client program to check the current status of ice accumulation and the history data. The server is in users' office for the users to collect ice information without leaving their office. The functions of the client program are to receive commands from the server and return ice information to the server.

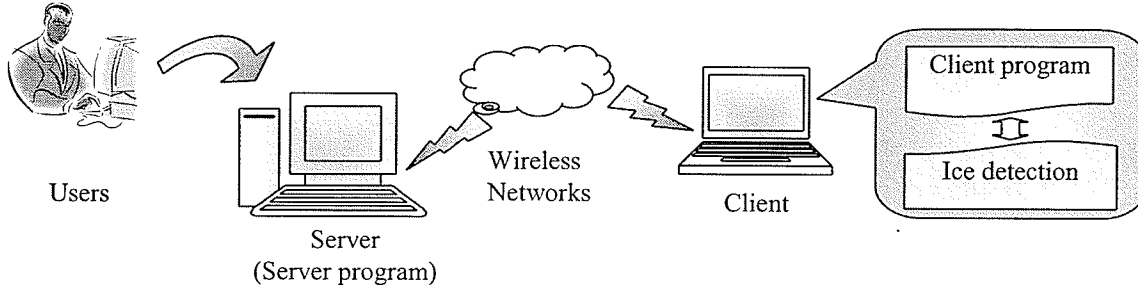


Figure 7.6 System structure

The ice detection support system developed is implemented using Visual C++. The component diagram of the system is shown in Figure 7.7. There are five components in the system. The server program, the client program and the ice detection program have been introduced. The functions of the wireless network threads are to create network connections and communicate through them. The wireless network threads constitute separate computational process that can run in parallel with the server and the client program. The advantage of this method is that the wireless network threads could be blocked for waiting for incoming messages, but the server and the client program are still able to continue performing user's command. The communication among components is the fundamental problem to solve for implementing the system.

To exchange the information between the server and client, a protocol is required to send commands and data over the wireless network. The protocol is designed based on the functions in the server program and the client program. When the server or the client program receives a protocol command, the programs will start a function based on the command. The functions in the server program are listed in Table 7.1. The functions in the client program are listed in Table 7.2. The network protocols are listed in Tables 7.3 and 7.4.

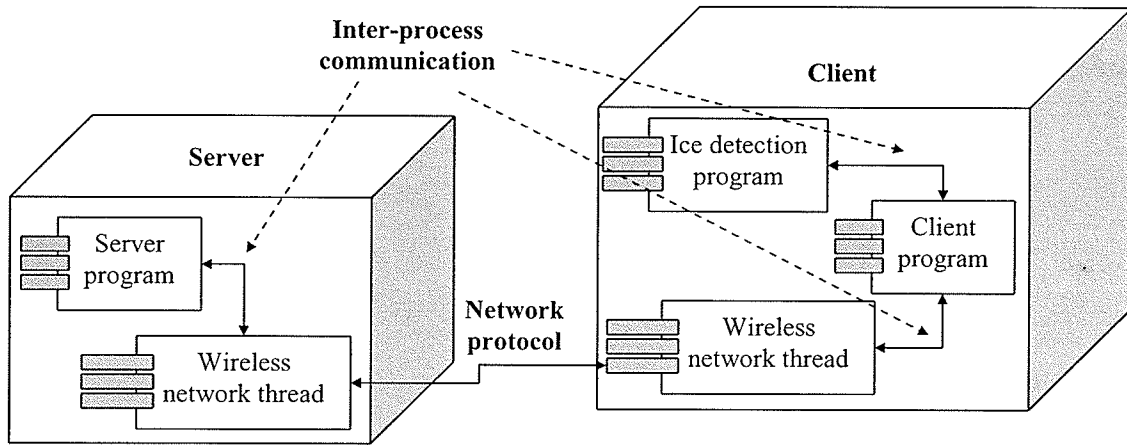


Figure 7.7 The component diagram of the ice detection system

Table 7.1 The functions in the server program

No.	Function name	Description
1	Retrieve Temp	Retrieve temperature data from the client program
2	Retrieve IceData	Retrieve ice data from the client program
3	Retrieve Picture	Retrieve an ice picture from the client program
4	Reset Mode 1	Set operation mode 1 to the line feature program.
5	Reset Mode 2	Set operation mode 2 to the line feature program.
6	Capture Picture	Request the client program to take a picture.
3	Client Status	Check whether the client program has connected with the wireless network.

Table 7.2 The functions in the client program

No.	Function name	Description
1	Send Alarm	Send an alarm message to the server when the ice thickness is greater than the alarm threshold.
2	Send Temp	Send temperature data to the server program.
3	Send IceData	Send ice data to the server program.
4	Send Picture	Send an ice picture to the server program.
5	Take Picture	Take an ice picture and send the picture to the server program.
6	Hello	Check whether the server program has connected with the wireless network.

Table 7.3 The network protocol in server side

No.	Protocols	Descriptions
1	CMD_RTemp_date	Retrieve the temperature data by the date.
2	CMD_Rice_date	Retrieve the ice data by the date.
3	CMD_RPic_date	Retrieve an ice picture by the date. The ice picture is the latest picture in client.
4	CMD_Capture_Pic	Request the client program to take a picture
5	Hello_Client	Check the status of the client program

Table 7.4 The network protocol in client side

No.	Protocols	Descriptions
1	CMD_Client_Alarm	Send an alarm message to the server program
2	CMD_Pic_Taken_filename.jpg	Send the filename of an ice picture to the server program when the picture is requested.
3	No_Existing	If the requested temperature data, ice data or ice picture doesn't exist then send this command
4	OK_message	If the requested temperature data, ice data or ice picture exist then send this command. The message is the length of the requested file
5	Hello_Server	Check the status of the server program

The communication between two programs in same computer is called inter-process communication. The client program and the ice detection program are two separated programs in client side. Two functions are needed in the client program: one is “starting and ending the ice detection program from the client program” and the other is “sending and receiving messages between the client program and the ice detection program”. The server program and the wireless network thread are two separated programs in server side. The function of sending message from the wireless network thread to the server program is needed in the server program. To solve these problems, the inter-process communication technique is used. The solutions are discussed as follows.

(1) Starting and ending a program

The CreateProcess() function is used to start the ice detection program from the client program. In short, CreateProcess() takes a filename for an executable file that will be run in the new process. The details of the CreateProcess() function can be obtained in Visual c++ reference books or at online help of MSDN. Following is an example using the function to start the ice detection program.

```
    BOOL bWorked;

    STARTUPINFO suInfo;

    PROCESS_INFORMATION procInfo;

    // set the path of the line feature program
    CString m_Process = "C:\\\\iceV2\\Debug\\Line_Feature.exe";
    char *vip = " aa";

    memset (&suInfo, 0, sizeof(suInfo));
    suInfo.cb = sizeof(suInfo);

    bWorked = ::CreateProcess(m_Process,

                               vip,          // can also be NULL

                               NULL, NULL, FALSE, NORMAL_PRIORITY_CLASS, NULL,

                               NULL, &suInfo, &procInfo);

    // keep the process id in memory
    m_dProcessPid = procInfo.dwProcessId;
```

If CreateProcess() succeeds, the ice detection program can be ended by the CloseHandle() function. The details of the function can be obtained on MSDN online help. Following is an example to end the ice detection program.

```
//The m_dProcessPid is kept in memory when starting the program
HANDLE ps = OpenProcess( SYNCHRONIZE|PROCESS_TERMINATE,
```

```
FALSE, m_dProcessPid);  
EnumWindows(EnumWindowCallback, m_dProcessPid);  
CloseHandle(ps) ;
```

The EnumWindows() function enumerates all windows using the EnumWindowsProc callback function. It will return the handle of a process that matches the value of m_dProcessPid. The handle is used by the CloseHandle() function to close the process.

(2) Sending and receiving messages

The WM_COPYDATA message is used to send and receive data between the client program and the ice detection program. One program sends a WM_COPYDATA message to pass the data to another program named SendMessage() function. The WM_COPYDATA message can be processed by OnCopyData() function of CWind class. Following is an example to send WM_COPYDATA message.

```
COPYDATASTRUCT cds;  
cds.cbData = count;  
cds.dwData = 0;  
cds.lpData = &msg;  
::SendMessage(hWndRecv, WM_COPYDATA, (WPARAM) m_hWnd, (LPARAM)  
    &cds);
```

(3) Sending message from the wireless network thread to the server or the client program

A custom message is used to send message to the server or the client program. The message is defined as follows:

```
#define MY_WM_ServerCommRec (WM_APP + 10)
```

The wireless network thread sends the message to pass a command to the server or the client program. The message is handled by OnMyWMServerCommRec() function of the server or the client program. Following is a code example to send the message.

```
SendMessage(hMain, MY_WM_ServerCommRec, n, 0)
```

The third parameter of the SendMessage() function is the command that the thread sends to the server or the client program. It is an integer number. Table 7.5 lists the commands.

Table 7.5 List of commands

Command	Descriptions
“1”	The requested file doesn't exist
“2”	The alarm command is sent
“3”	A new picture has been taken.
“4”	The client is connected with network
“5”	The requested data file or picture is ready for download
“10”	The progress bar is triggered to start
“11”	The progress bar moves one step forward
“12”	The progress bar is triggered to end

7.4 Experiments

The experiments for the image-based 3D ice detection system include two parts: (1) Testing the 3D ice detection method in laboratory, (2) Testing the ice detection support system in real environments. The integration of the 3D ice detection method and the support system is the next step of system development. The 3D ice detection method is implemented using MATLAB™ and Visual C++, which consists of four modules: the camera calibration, edges of ice detection, points matching based on the epipolar geometry, and 3D coordinates calculation. The advantage of separating the algorithm into different modules is that it makes it possible to exchange the algorithm for each module at a later stage. The algorithm can be improved by developing a new algorithm for each module without having to redefine whole

algorithm. The client side of the ice detection system includes a digital camera and a laptop computer that are installed on a pole cross-arm. The server side is a desktop computer which is installed in a base station.

7.4.1 Experiments for the 3D ice detection method

Experiments were carried out with images taken by digital cameras. The input image size is 640*480 pixels. The diameter of the transmission line is 16 mm. A planar checkerboard with double-triangle pattern is used for camera calibration.

Figure 7.8 shows the experimental results of the camera calibration. The proposed camera calibration method is used in the camera calibration. Figure 7.9 shows the experimental results of the ice edge detection. The edges of ice are successfully detected by a multi-scan method. Three image-scanning images are shown in the Figure. Figure 7.10 shows the experimental results of the points-matching. One epipolar line and two matched points are shown in the pictures. Eight peak points on ice edges are marked by numbers. Number 4 is used as the example. The peak point is marked by a dot in left image. The epipolar line of the given point in right image is shown in a black line. The edges of ice are shown in gray lines. The search area for the given point in right image is constrained by the epipolar line and ice edges. The black rectangle in right image is the search area. The matched point is marked by a dot. With the help of the epipolar lines and ice edges the matched points are found on the smooth surface of ice. The experimental results of the 3D coordinate calculation are shown in Figure 7.11. Eight matched points are shown in the figure. The comparison of calculated ice thicknesses with measured values is shown in Table 7.6. Four results are selected from all experimental results and shown in the table.

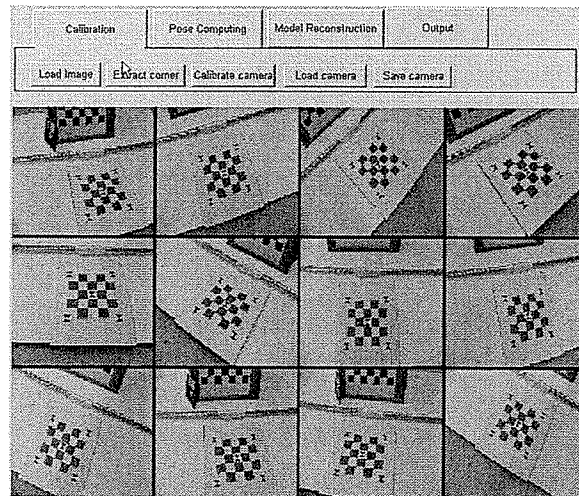


Figure 7.8 The camera calibration

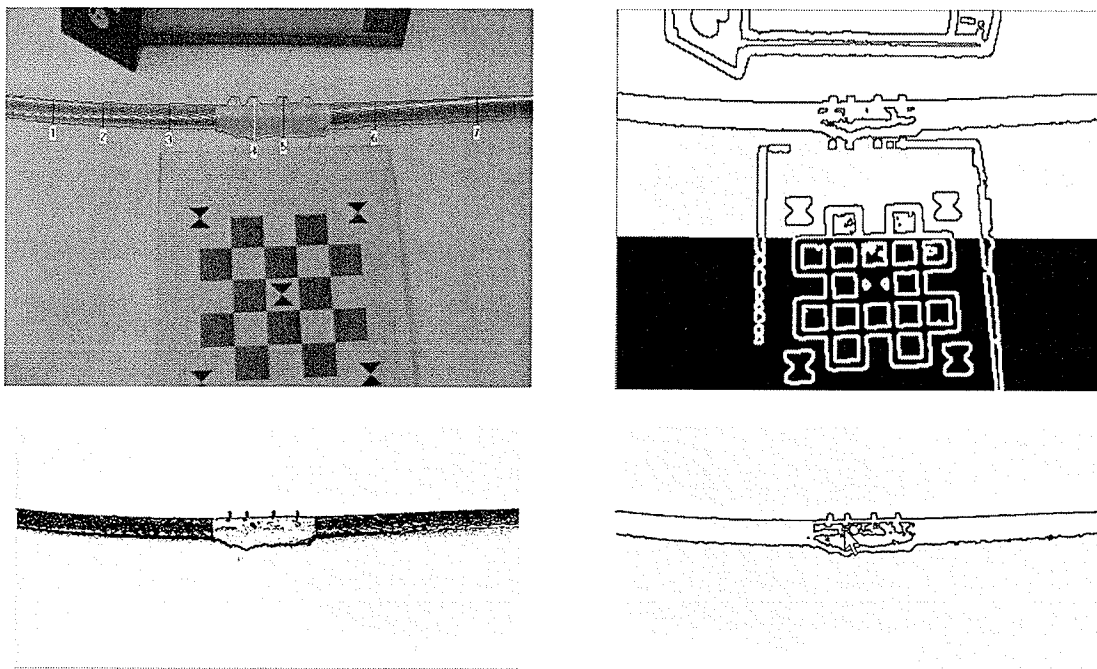


Figure 7.9 Multiple scan to detect ice edges

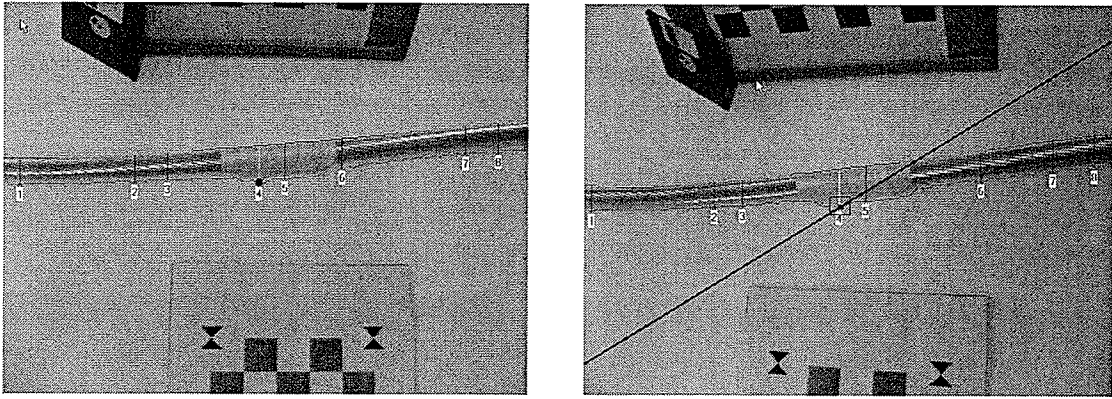


Figure 7.10 Epipolar lines in two images

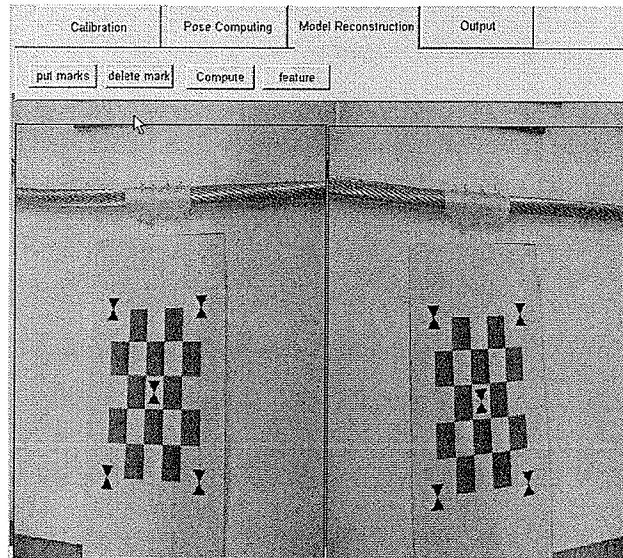


Figure 7.11 The 3D coordinates calculation of peak points on edges of the ice

The experimental results show that the obtained ice thicknesses are not accurate. But the correspondent points are successfully detected using this method in the experiment. Therefore the experiment provides a strong indication that the method is feasible.

Table 7.6 Experimental results of ice thickness calculation

Ice thickness	Experimental results (mm)	Measured value (mm)
1	8.5	4.9
2	6.2	5.4
3	4.3	4.0
4	3.5	3.1
Average	5.6	4.4

7.4.2 Ice detection support system in real environments

Figure 7.12 shows that the ice detection system that has been installed in a real environment. The distance between the pole and the base station is about 500 meters. The system has continuously worked since Dec. 2006 without any problems. Thousands of ice images have been taken. Four ice images are selected and shown in Figures 13 -16. Figures 13 and 15 are hoarfrost on the power transmission line at daytime. Figures 14 and 16 are ice on the power transmission line at night. Ice edges are successfully detected for both hoarfrost and ice. The experimental results prove that the ice detection support system can support the 3D ice detection method to work in real environments.

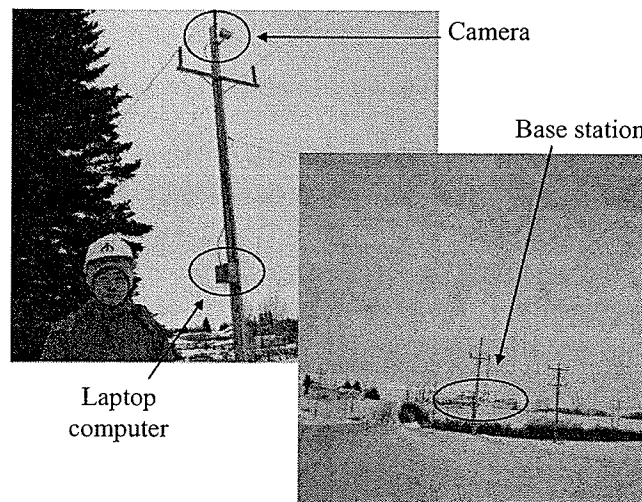


Figure 7.12 System installation (Dec 16, 2006)

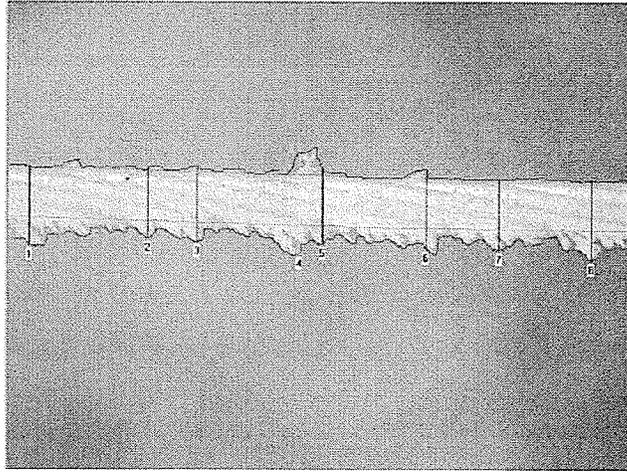


Figure 7.13 Hoarfrost on the power transmission line at daytime (Feb 10, 2007)

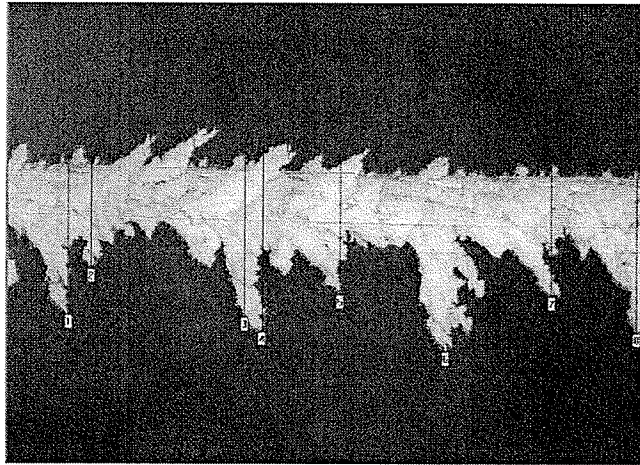


Figure 7.14 Hoarfrost on the power transmission line at night (Feb 10, 2007)

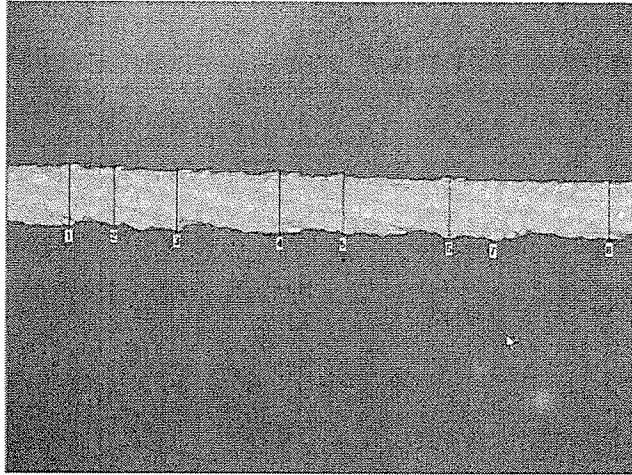


Figure 7.15 Ice on the power transmission line at daytime (Jan 20, 2007)

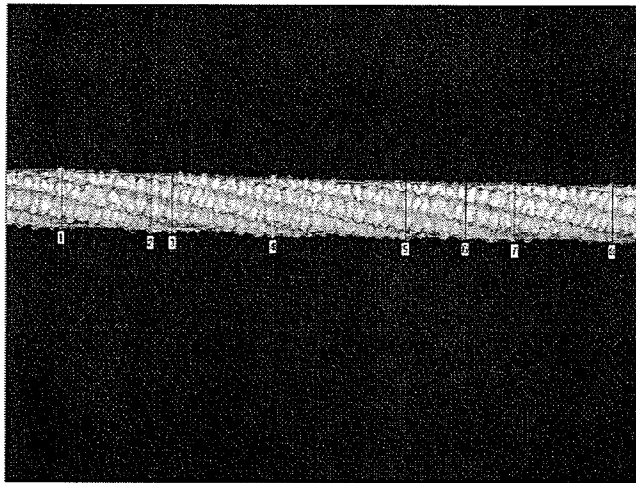


Figure 7.16 Ice on the power transmission line at night (Jan 20, 2007)

Chapter 8

A VR-based data retrieval system

The second application of the image-based 3D data acquisition methods is presented in this chapter. A VR-based data retrieval system for product design and manufacturing is proposed. The framework of the system and the key technologies in the framework implementation are presented first. The principles of the VR-based user interface design and construction are then discussed. An image-based 3D data acquisition system is developed to aid in building the 3D user interface. An example is presented at the end of this chapter.

8.1 The framework of the VR-based data retrieval system

The methods discussed in the literature review (Chapter 2) have their disadvantages in user interface building and represent layers. Firstly, a separated 3D world has to be built for connecting with the database to retrieve product information. Secondly, these methods use cubes or cones to represent the schema in a database: therefore they are not convenient to use in order to understand the structure of a product and the relationship of components in the product. Nowadays Virtual Reality has been applied in the whole design and manufacturing process. It provides users a virtual design and manufacturing environment. Users can design 3D models of a product, simulate the manufacturing process and analyze the product function, therefore the 3D product model can be directly used as 3D user interface and the 3D model can help users to understand the structure and relationship of a product to search product data quickly. Therefore the objectives of the VR-based data retrieval system are to

help users to search for information on a product and its development easily and to make collaboration effective in a concurrent engineering (CE) environment. In the system shown in Figure 8.1, users in a CE group are linked with a data retrieval system that has three major components: a VR-based user interface, an integrated product database and a Web and database server set. The data retrieval system uses VR as a user interface where the user can:

- 1) Easily find and obtain information related to a product development process;
- 2) Understand the information of whole product; and,
- 3) Search product information using the touch sensor in a virtual environment.

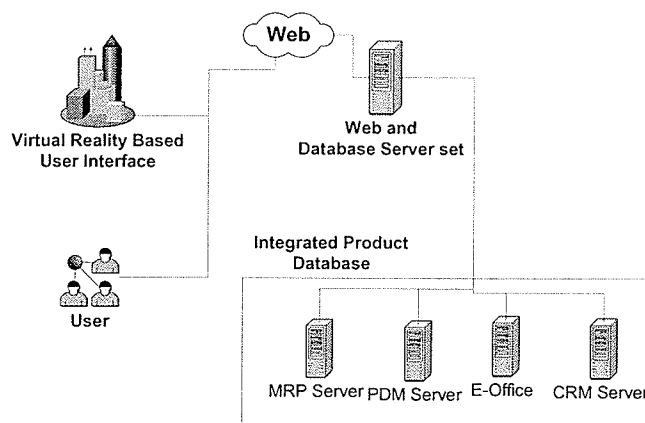


Figure 8.1 The framework of the VR-based data retrieval system

The Web technology is adopted in a database server set as a tool for collaborating in CE. Each user in different locations connected by a network can access the same product information of an integrated product database. The integrated product database runs on the database server set. It then gathers data from different systems including PDM (Product Data Management) or MRPII (Manufacturing Resource Planning) and provides this data to the VR-based data retrieval system. The integrated product database also enables users to find dynamic information from a design change, solutions of problems in manufacturing process, or varying customer demands.

8.2 Key technologies in the framework implementation

An integrated product database and the VR-based user interface are two key technologies to implement the framework.

8.2.1 An integrated product database

The VR-based data retrieval system supports information of the product design, process planning, manufacturing and customers' feedback. It is important to have the necessary and adequate product information in the VR-based data retrieval system. An integrated product database gathers information from other existing product data systems, such as PDM, MRP II etc. The design and implementation of the integrated product database are described as follows.

(1) Use of UML (Unified Modeling Language) in the integrated product database

UML is an industrial standard for the object-oriented analysis and software development (Rumbaugh *et al*, 1999; Roques, 2004). Literature shows that UML is an excellent model language in developing the information system (Eynard *et al*, 2004; Costa *et al*, 2001). UML models a system through the system development life cycle, starting from the system description to the complete software system. A product design and manufacturing process is a complex system and it includes static and dynamic activities. A UML model can describe all aspect of a product development. Therefore UML is a good tool for developing the integrated product database.

UML consists of nine types of diagrams. They are class diagram, object diagram, state chart diagram, activity diagram, sequence diagram, collaboration diagram, use case diagram, component diagram and deployment diagram. In this research only activity diagram and class diagram are used in a product design and manufacturing system. An activity diagram

describes activities and actions occurring in a product design and manufacturing system. A class diagram uses classes to describe types of objects in a system, and relationships for static relationships among the objects in the integrated product database.

(2) The system structure of the integrated product database

The proposed system structure of the integrated product database is shown in Figure 8.2. The diagram illustrates two key components: dynamic query server and product database. The dynamic query server is a server program. The server can load dynamic product data from other PDM or MRP II systems and store them in the product database. The product database stores product data and provides the data to the VR-based user interface.

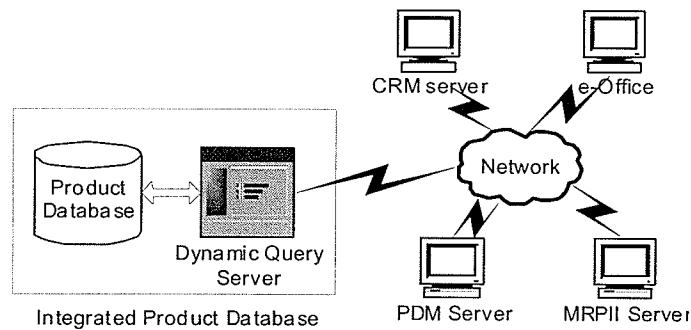


Figure 8.2 System structure of the integrated product database

To load dynamic product data from other systems, the dynamic query server collects product data based on a schedule. For example, it collects product data at 10 o'clock every night from a PDM or MRP II system. All product data that have been updated will be updated in the product database. Therefore the product database will be kept updated. This ensures users can get the latest product information. This step cannot be done in real-time because of the time-consuming product data format conversion. The details of product data format conversion are explained as follows.

As above-mentioned, product data are generated from various applications and these data cannot be displayed directly in current VR systems. Therefore the format of product data has to be converted for the VR display. Product data can be divided into three types: 3D models, 2D drawings, and different types of text documents. Product data format conversion is based on these three types of data. 3D models include 3D product models generated by 3D CAD software, 3D analysis results and 3D simulation models. All these 3D models have to be converted into standard product data exchange formats, such as, VRML (Virtual Reality Model Language) or IGES (Initial Graphics Exchange Specification). These files can be imported into VR systems. 2D drawings are engineering drawings generated by CAD software systems. If a VR system cannot display 2D drawings then the 2D drawings have to be converted into 2D images. Different types of documents include the product specification and experiment results. Most of text documents can be displayed directly in VR systems. If documents have special style, such as embedded tables or pictures, they have to be converted into 2D images by using conversion software.

(3) Design of the integrated product database using UML

The product design and manufacturing process is a complex process. The related information comes from sales, design engineers, managers and manufacturing engineers through the process. For a large amount of product data, it is important to identify the necessary and adequate product data for the integrated product database. There are two steps required to develop an integrated product database. The first one is the product design and manufacturing process analysis. A model that describes the whole product design and manufacturing process has to be obtained. The model shows all design and manufacturing entities in the process, and the relationships of the entities in the process. The other is the

product data structure analysis. A model is needed to describe the data structure of the integrated product database. The model shows all product data types, attributes, value constraints for data attributes, and the relationships of product data. The integrated product database can then be developed based on the model.

8.3 VR-based user interface

The VR-based user interface provides a visually rich environment for the product data search.

(1) VR construction methods

Building VR models has always been a difficult task. There are three methods to build 3D models for VR systems: using CAD packages, using 3D scanners, or 3D modeling from 2D images. Methods 2 and 3 are suitable to the model created from an existing environment. In a product design and manufacturing process without the existing product, 3D models are normally generated using CAD systems. Figure 8.3 shows the VR construction from different data.

The data from 2D drawings can be modeled using different CAD systems, for examples, Pro/Engineer or AutoCAD, and models are then converted into standard product data exchange formats to export into a VR system. The output data of the Fourier Transform Profilometry (FTP) method are cloud points. The data have to be converted into the solid model in CAD systems. Then the model is assembled in the VR system. The output data of the photogrammetry method is the coordinates of feature points. The solid model can be built in CAD systems using the coordinates. In addition to the scaling problem that can be avoided

using the same unit in CAD systems for VR models, differences of coordinate systems of the 3D models can be solved by using position information in assembly models.

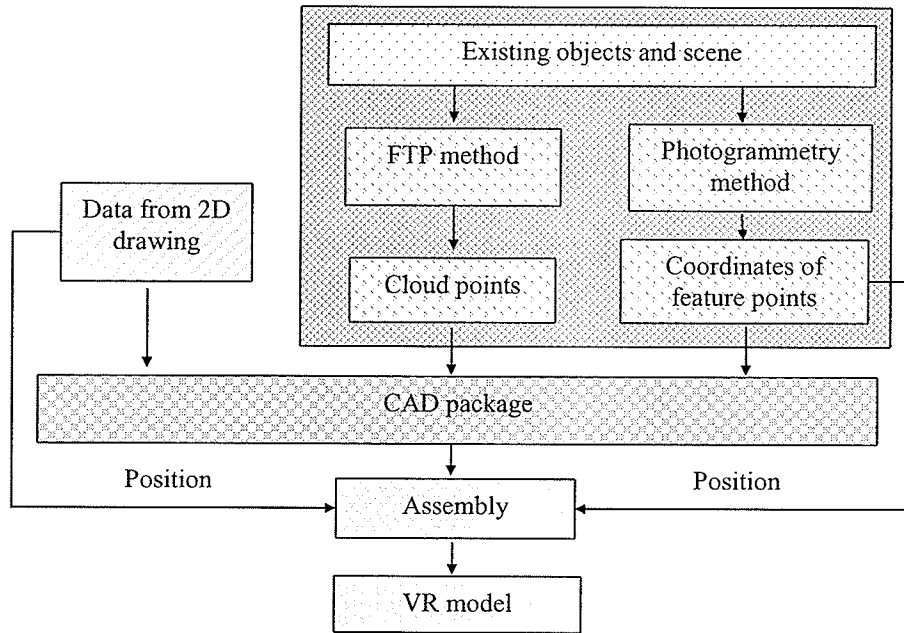


Figure 8.3 The VR construction from different data

(2) Development of the VR-based user interface

An immersive VR system is used in this research. The structure of the VR-based user interface is shown in Figure 8.4. It consists of a VR-based user interface and four inputs. 3D CAD models are generated from CAD systems for 3D views of a product in the VR-based user interface. Query requirement is used for users to send “query command” to search product information through the VR-based user interface. As there is no computer keyboard or mouse available in the immersive VR system, a virtual user-based method is used in this research. The virtual user is a 3D model to represent a real user in VR. The “query command” is attached to 3D models in the VR system. Collision detection nodes are attached to the virtual user and 3D models. When the virtual user touches a 3D model in the VR system, the collision happens. The collision detection node gets the “query command” and

sends it to the database server set. The system can simulate a product assembly, disassembly, or a production process.

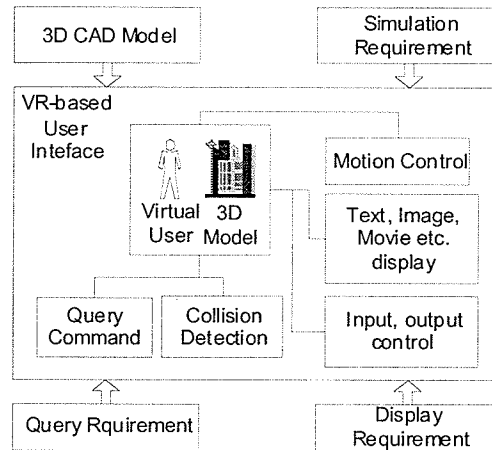


Figure 8.4 The structure of the VR-based user interface

8.4 Image-based 3D data acquisition system

8.4.1 Overview of the image-based 3D data acquisition system

The image-based 3D data acquisition system is to generate 3D models using 2D images. Because the FTP method is only suitable for small and medium size objects with freeform surfaces because the shape variation of the no-freeform surface is greater than the phase distribution of the fringes and the photogrammetry method is suitable for a wide range of objects and scenes, the integration of two methods is a feasible approach to 3D data acquisition for different sizes and types of objects. Therefore the 3D data acquisition system proposed in this research has three modules of the photogrammetry method, the FTP method and data output as shown in Figure 8.5. The photogrammetry method includes three components: Camera calibration, position calculation and feature point calculation. The FTP

method includes three components: system calibration, phase calculation and cloud point calculation. Each component in the system is described as follows:

Camera calibration: The intrinsic parameters of the camera are obtained in this component. The details of camera calibration are described in Chapter 4.

Position calculation: The extrinsic parameters of the camera are obtained in this component.

Feature point calculation: The feature points are selected by users. The users click the left button of a mouse in two images of one feature point to obtain the image coordinates of the point. The 3D coordinates of feature points are calculated using the triangulation method.

System calibration: The system parameters of the FTP method are obtained in this component.

Phase calculation: The phase information is obtained using FTP method. Phase unwrapping is involved in this component.

Cloud point calculation: The 3D coordinates of object points are calculated using phase information and the system information.

The output data module exports the 3D information to CAD software.

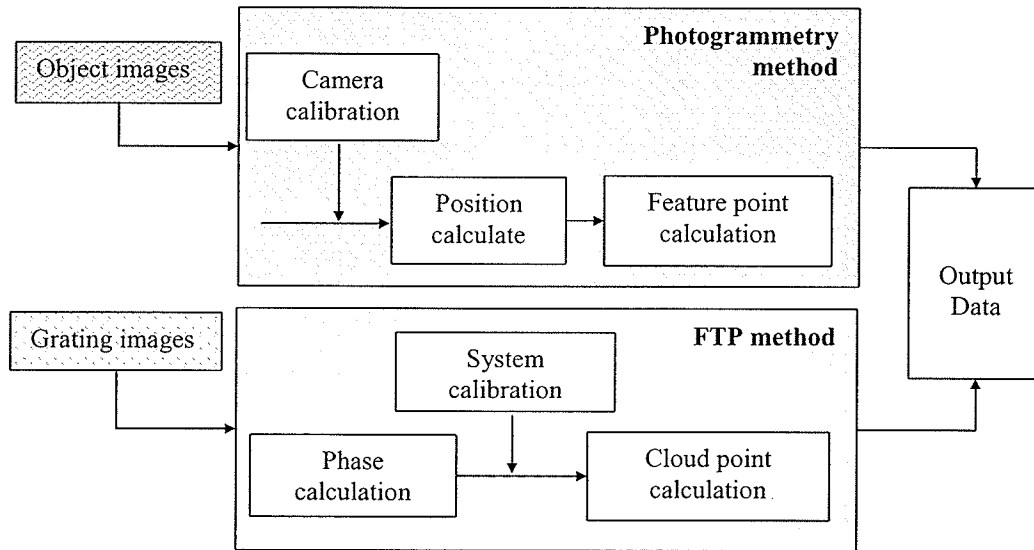


Figure 8.5 The structure of the image-based 3D data acquisition system

8.4.2 System interface

The user interfaces of the image-based 3D data acquisition system are shown in Figures 8.6 and 8.7. As shown in Figure 8.6, six user interfaces are implemented for 3D data acquisition using the photogrammetry method. The main user interface displays a list of two methods, and allows users to run the photogrammetry method or the FTP method. The images of the calibration patterns are loaded in the user interface of camera calibration to calibrate the camera. Pose calculation and feature points calculation are performed by loading two images of an object into the program and marking corresponding points in two images. Tools for loading images, marking points, and storing system parameters are provided by the toolbar. 3D points are displayed in the user interface of output.

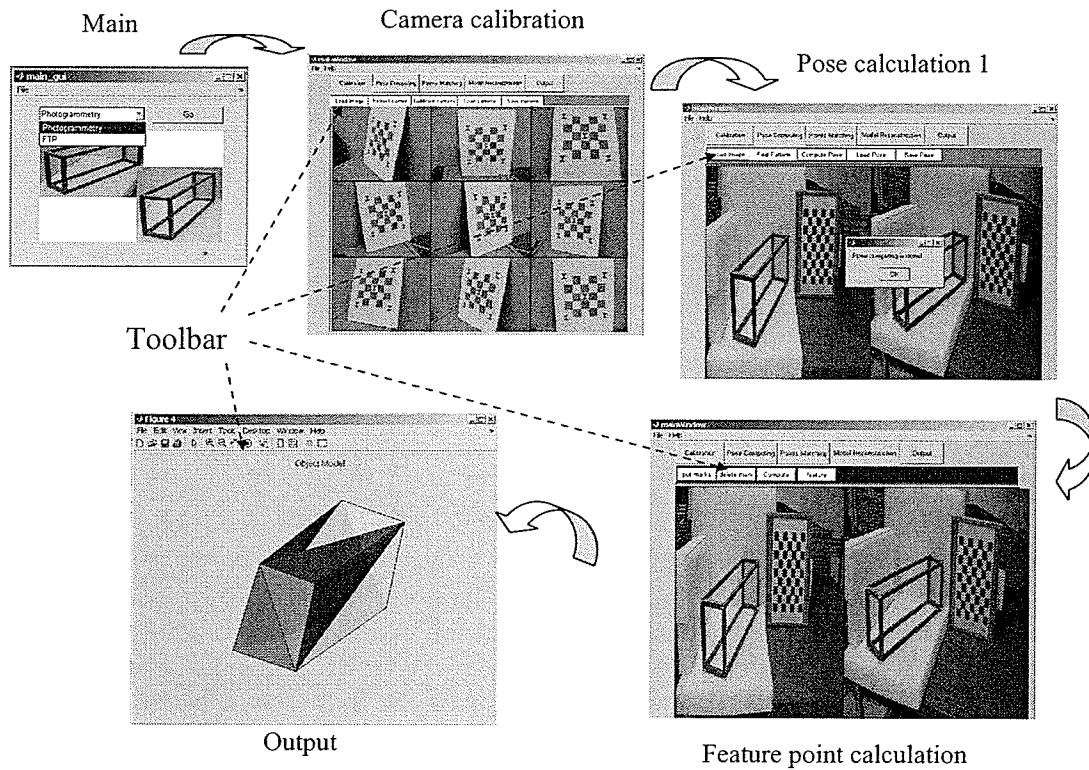


Figure 8.6 User interfaces for photogrammetry method

As shown in Figure 8.7, five user interfaces are implemented for 3D data acquisition using the FTP method. The image and parameters of the helper pattern are inputted in the user interface of system calibration to calibrate the FTP system. The reference grating image and the deformed grating image are loaded in the user interface of phase calculation to obtain the phase information. The 3D coordinate calculation is performed by using the phase information and the system parameters in the user interface of cloud point calculation. 3D data are exported to CAD software in the user interface of output.

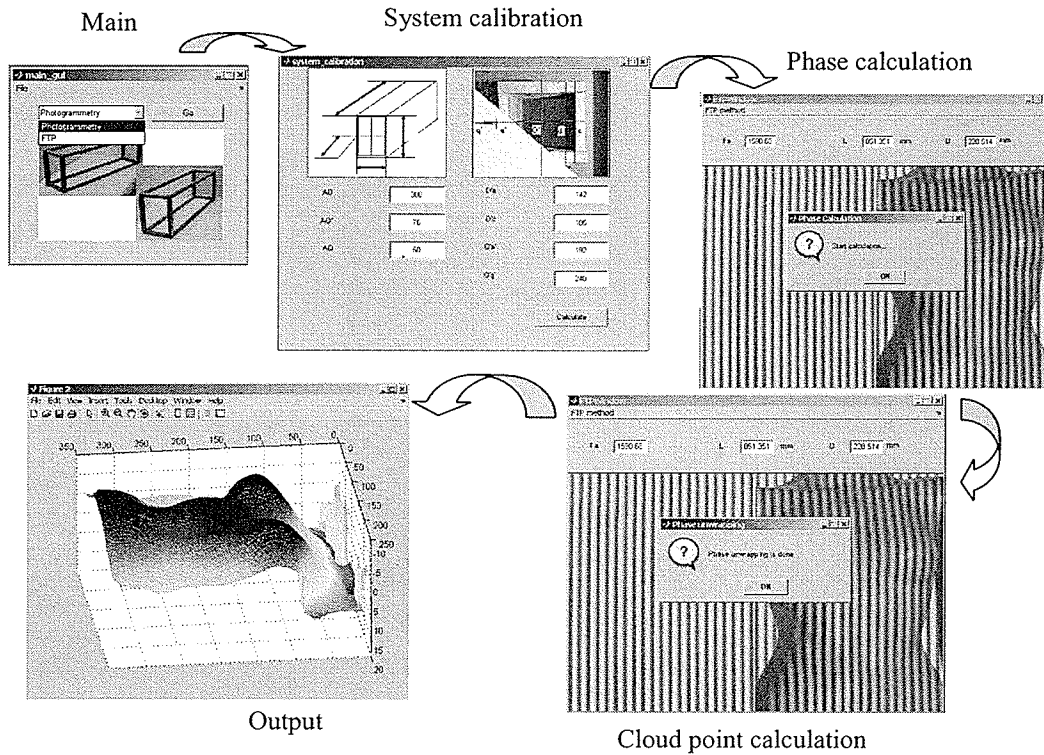


Figure 8.7 User interfaces for FTP method

8.5 An example and discussion

An example is used to evaluate the proposed framework of the data retrieval system. The example is developed using the EON Reality system (Eon 2003), JAVA and Access database. In the implementation, the integrated product database is composed of Access database and JAVA program. When this application runs in the Eon software, it shows the VR scene in EonX plug-in. Users can view a 3D product model in a HMD (Head mounted display) and move their virtual hand in VR and give commands to VR using the data-glove. When users use their virtual hand to touch a virtual part and send a “search” command, the application will search the Access database and return results to the VR scene. The searched results are displayed in the VR scene.

8.5.1 The integrated product database

A general product design and manufacturing process is shown in Figure 8.8. The structure of the integrated product database is obtained through analyzing a general product design and manufacturing process. Figure 8.9 is the class diagram of the integrated product database. There are 11 classes in the diagram. They are product, drawing, machine, order, tools, maintenance, suppliers, storage, quality, schedule and operation. The class “product” includes the product itself and assembly, sub-assembly or parts of the product. The function of all class is listed in Table 8.1.

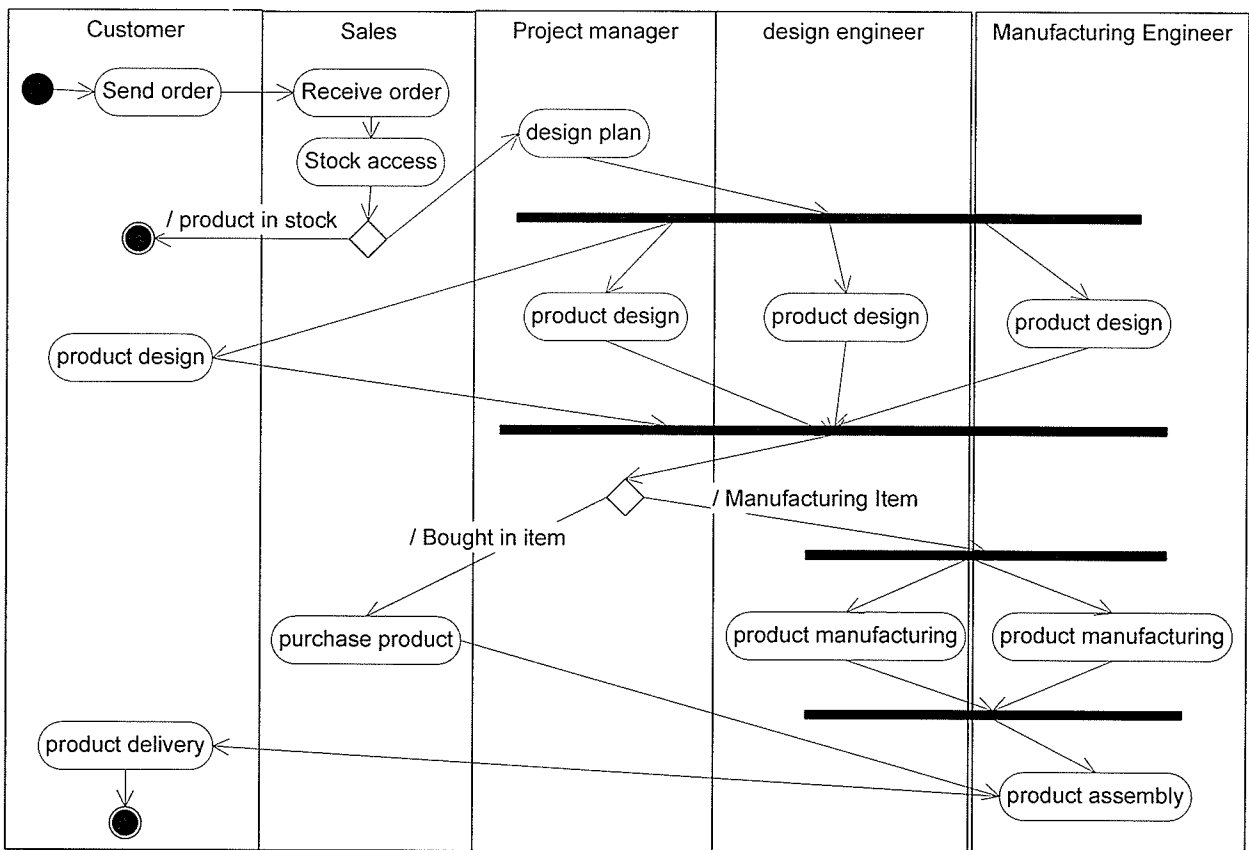


Figure 8.8 A general product design and manufacturing process

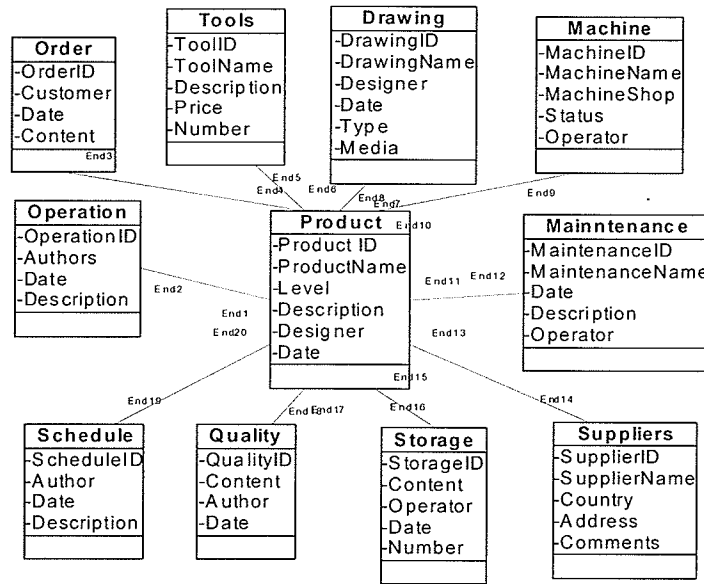


Figure 8.9 Class diagram of product data deposit

Table 8.1 Function of class in the model of product data deposit

Class	Function
Product	Information about product or components of the product
Drawing	View the 2D drawing of a product or components of the product
Machine	Information about machines required when manufacture a part.
Order	Order information about a product or components of the product
Tools	Information about tools required when manufacture a component of the product
Suppliers	Information about suppliers when buy a component of the product
CNC	View CNC programs for a component of the product
Operation	View the sequence of operations for a component of the product
Quality	Requirement of quality for a component of the product
Schedule	Manufacturing schedule of a component of the product
Storage	Storage information of a component of the product

8.5.2 The VR system

EonX Plug-in and Eon Immersive are used for 3D product model displaying and communicating with the VR. They are products of EON Reality Inc. The EON Immersive system is a PC-based system. It consists of stereo capable HMD and data gloves. The EonX Plug-in is an ActiveX objects for viewing an EON model without having EON installed. It allows distribution of VR applications on the network and it supports data gloves and HMD. By using this system, a user can navigate and control the VR system simply by hand and head movements. The system is shown in Figure 8.10. The 3D model of the VR system is displayed in the HMD. There are three motion sensors in the system, one is on the HMD and two are on the data gloves. When users move their head or hands, the sensors can transfer the motion information to Eon Immersive software. The Eon Immersive software controls the 3D model based on script program of the system. The details of the 3D model construction and script program will be discussed in the following part.

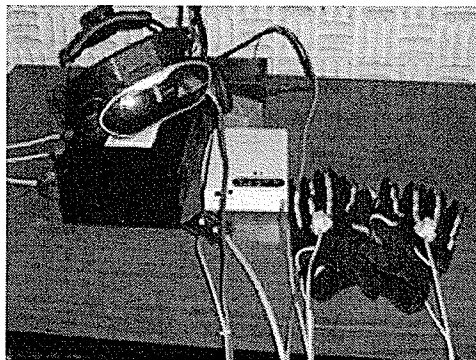


Figure 8.10 HMD and Data-gloves

A JAVA applet located on the same Web page as the EonX plug-in is used to communicate with the integrated product database. EonX plug-in first gets the command from the data gloves and sends user's command to JAVA Applet, then the JAVA Applet sends a request to the database server set. A JAVA-based program runs on the database server set to search the

integrated product database and sends back searched information to the EonX plug-in. A JAVA program is developed in this system to transfer data from other relational databases to the Access Database. The program reads data from those databases and saves the data into Access Database. This technology can be used to transfer data from PDM or MRPII to the integrated product database and it enables the dynamic information integration. This structure is shown in Figure 8.11.

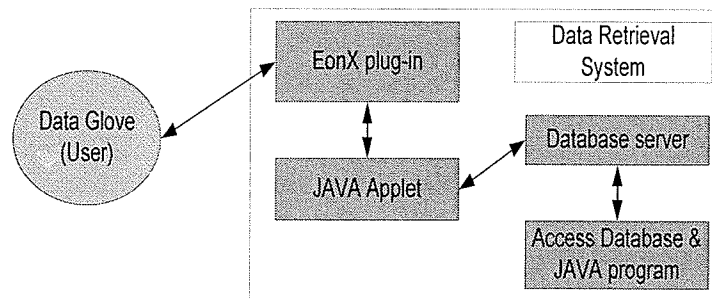


Figure 8.11 System structure of getting data from product data deposit

8.5.3 The VR-based user interface

The VR-based user interface is built using EON Studio and Pro/E. It consists of three parts: the static displayed 3D product model, scripts for user interaction and an immersive virtual environment. The static model is formed in Pro/E and saved as "SLP render" file. The "SLP render" file can be exported directly into Eon Studio. There are three parts in the static model. One is the 3D product model, and another is a virtual hand in the VR. The virtual hand represents the virtual user in this system. The third part is a virtual room to display the product. Nodes and scripts can be added based on requirements of the application in EON Studio, for example, a pinch glove node is added to receive commands from the data glove. Some in-event and out-event nodes are added in the model to communicate with JAVA Applet. In this model, collision detections are added to each model of parts to detect user's virtual hand touch with the product model. If the hand touches the part, the collision node

will send the "component ID" to a script node to tell the system which part is touched. After the model is created, it can be published to Web browsers using "create Web distribution" in EON studio.

The core part of the system is the immersive virtual environment. Three techniques are used in the EON software to implement the immersive virtual environment. These three techniques are an interface with data gloves and HMD, a virtual user, and a virtual user control.

The interface with data glove and HMD in the EON software uses the 3SPACE FASTRAK® tracker system as a tool to detect 3D positions of the data gloves and HMD. The EON software provides Peripherals node, FastrakManger node, TrackSystemReceiver node, PinchGove node and Gesture node as the interface of the hardware. Figure 8.12 shows the use of these nodes to connect HMD and the data gloves in the system. A FastrackManager node is placed under a Peripherals node, and three TrackerSystemReceiver nodes (TrackerSystemReceiver_R_Hand, TrackerSystemReceiver_L_Hand and Head) are placed under the FastrackManger node. Three TrackerSystemReceiver nodes are used to connect with HMD and the data gloves for left hand and right hand. The PinchGlove node and all Gesture nodes (R1 Grab, R2 Walk, R4 Gesture, etc.) are used to identify gestures of the data gloves. The virtual user is used to send "query command", it is represented by a body node. The body node is composed of a head and two hands as shown in Figure 8.13. Users can view the virtual environment through the head node and can navigate and manipulate the virtual environment by two hands. The virtual user control operates 3D positions of HMD and the data gloves using the 3SPACE FASTRAK® tracker system. The virtual user navigates the virtual world based on inputs. Figure 8.14 shows its implementation in the

EON software. Users' positions can be received by the notes of TrackerSystemReceiver_R_Hand, TrackerSystemReceiver_L_Hand and Head. The positions are sent to Script nodes. The HeadAdjust script node adjusts the position of the head node so that users can see different scenes of the virtual environment when they turn around their head. The ScriptRHandPostAdjust and ScriptLHandPostAdjust adjust positions of two virtual hands in the virtual environment for users to grab objects and manipulate virtual objects. The Navigation_script_left and Navigation_script_right nodes adjust positions of whole body of the virtual user for users to “walk” in the virtual environment.

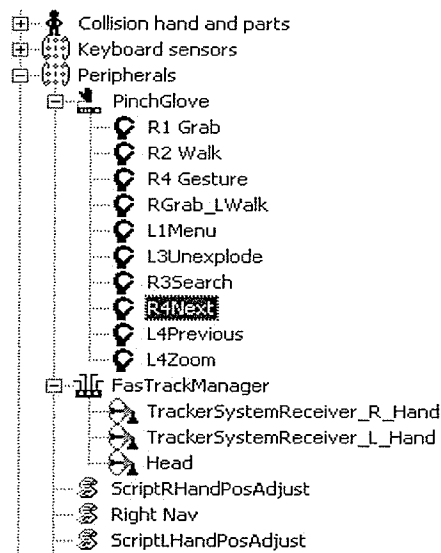


Figure 8.12 Interface of EON software with VR Hardware

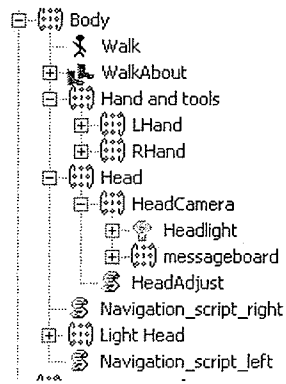


Figure 8.13 The structure of the virtual user

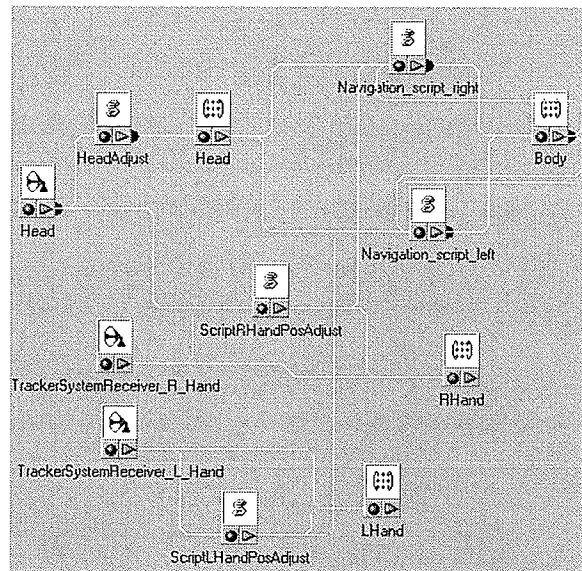


Figure 8.14 Implementation of virtual user control

8.5.5 The system user interface

The system user interface is embedded in the Internet Explorer as shown in Figure 8.15. Users retrieve product data from the database Server. The user wears HMD and data gloves. There are virtual hands in the VR scene. Users can move their hands to control the virtual hands and move the head to change views in the scene. The sequence of data searching is operated as follows: the user moves the virtual hands to touch a part in the 3D product model, a collision detection is used to find the part that the user has touched, and the related part

number of the product. Then the user moves virtual hands to system menu to choose an action. The system menu shows a list of the product information, the details is shown in Table 8.1. After the user pinches the thumb and index finger of right hand to send a “search” command, the part number and the request of the product information are sent to the database server. A SQL (Structured Query Language) is created based on the part number and the category of the product information. Then the product information is searched in the integrated product database based on the SQL and is sent back to the user interface. The product information is displayed in a message board at the middle-top of the user interface. A 2D drawing is displayed in the VR-based user interface as shown in Figure 8.16. In this system, there is no need to type in the part number, and therefore users do not have to memorize the menu to search the product information. The 3D product model in the system shows the hierarchy structure of a product. It provides users an overview of the product and helps users to understand the structure of the product to find the specific part information of the product.

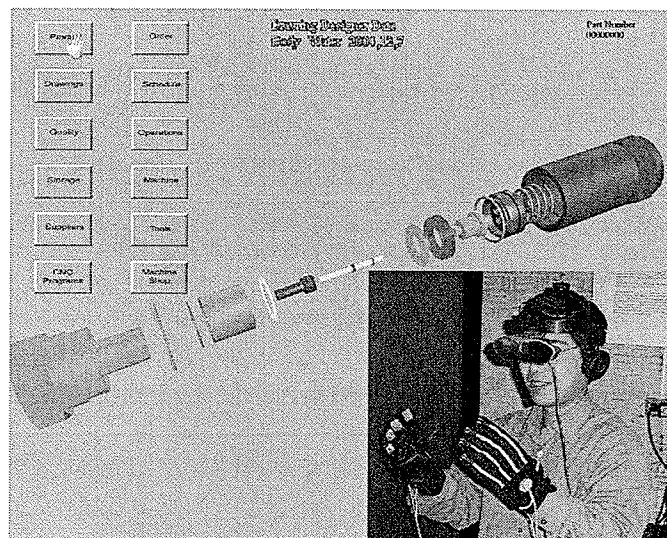


Figure 8.15 The system user interface

This data retrieval system provides an effective support for CE in the search of product information. The VR-based data retrieval system implemented in this research has following advantages:

- 1) It provides an overview of the product structure and relationships of the product data.
- 2) The product data in the scene can be edited and selected.
- 3) Different needs from various users can be satisfied, and the system is easy to operate.

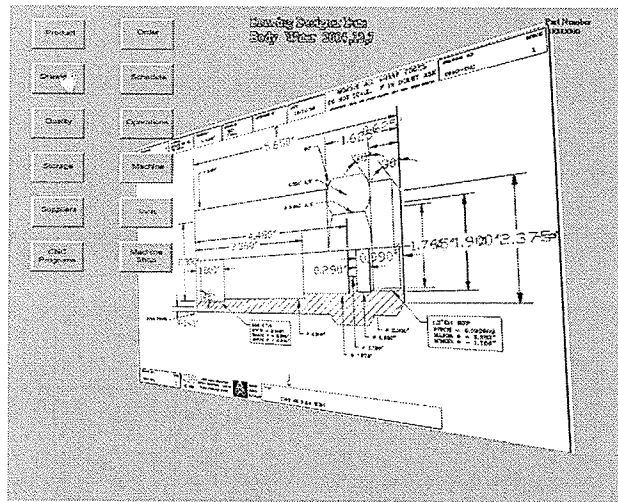


Figure 8.16 A 2D drawing in the VR-based user interface

8.5.6 CMM machine modeling

The 3D model of a CMM machine is built using the proposed 3D data acquisition system. Figure 8.17 is a flow chart of the modeling process.

The first step is the camera calibration. The checkerboard pattern with the double-triangle was used to calibrate the camera. The second step is the image capturing. Two images of the CMM machine were taken from two directions. The third step is the dimension measurement for 3D modeling. The length, width and height of components of the machine were calculated using the photogrammetry method. The final step is the 3D model construction. The 3D model was constructed using the Solidworks modeling system based on the

dimensions obtained. Figure 8.18 is the images captured to calibrate the camera. The intrinsic parameters of the camera are:

$$k = \begin{bmatrix} 1194.18 & 0 & 498.96 \\ 0 & 1187.53 & 364.36 \\ 0 & 0 & 1 \end{bmatrix}.$$

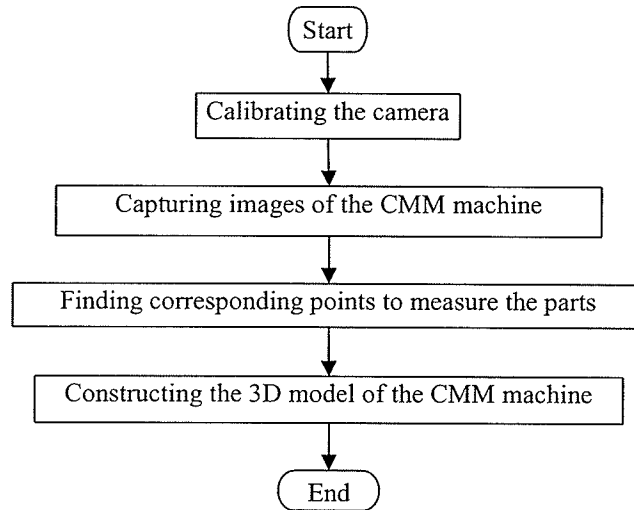


Figure 8.17 The flow chart of building a 3D model of the CMM machine

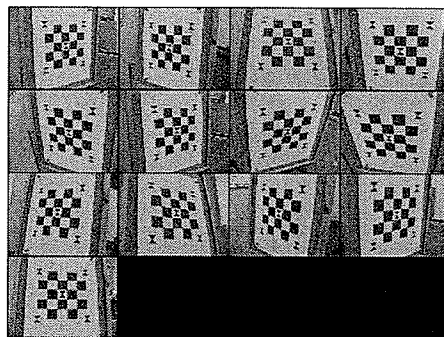


Figure 8.18 The images for camera calibration

Figure 8.19 shows the CMM machine. There are 9 components that are constructed by the photogrammetry method. They are numbered from 1 to 9 as shown in Figure 8.19.

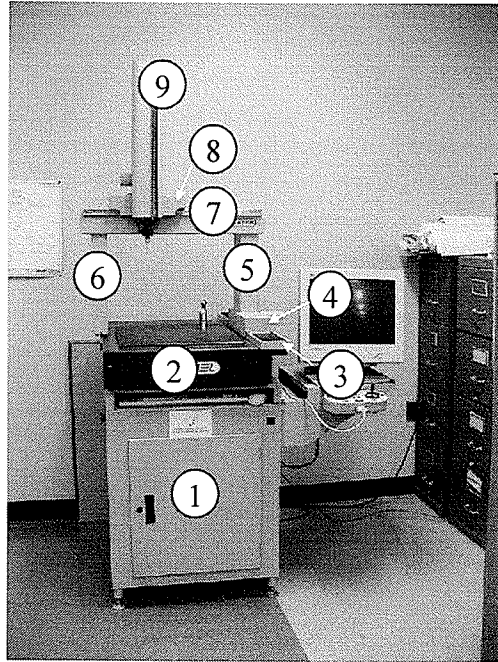


Figure 8.19 The image of the CMM machine

Figure 8.20 shows two images used to measure the dimensions of components 1 and 2. The mark “○” in left image and the mark “□” in right image are the correspondent pixels for the dimension calculation.

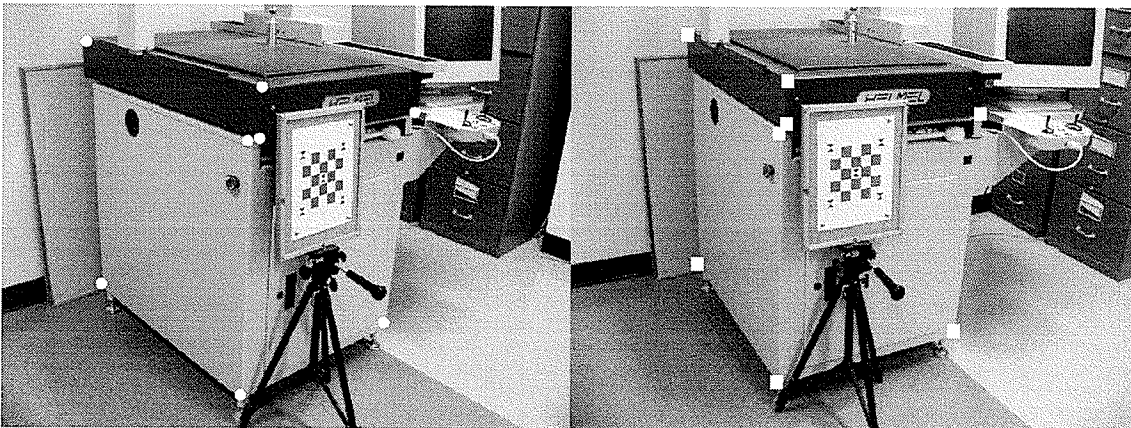


Figure 8.20 Two images for measuring parts 1 and 2

Figure 8.21 shows two images used to measure the widths and heights of parts 3, 4 5, 6, 7, 8 and 9. The mark “○” in left image and the mark “□” in right image are the correspondent pixels for the dimension calculation.

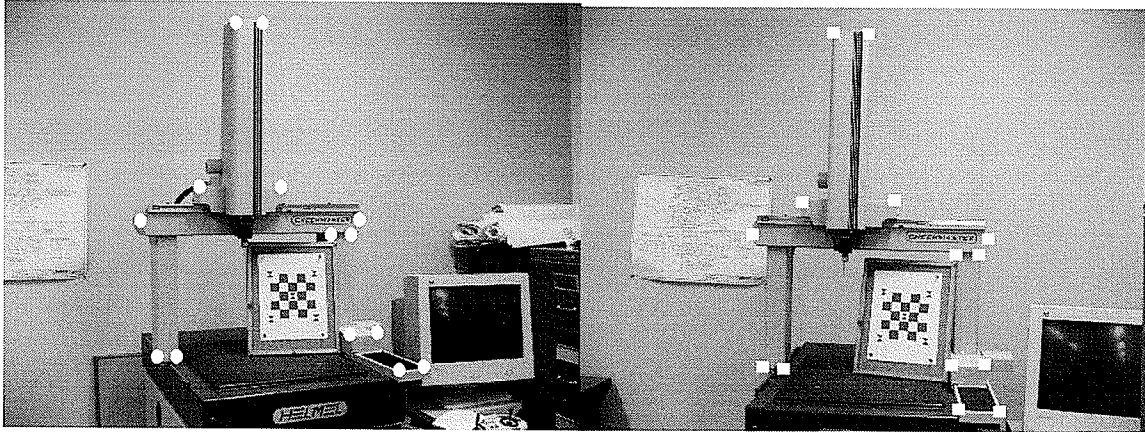


Figure 8.21 Two images for measuring widths and heights of parts 3 to 9

Figure 8.22 shows two images used to measure the lengths of parts 3, 4 5, 6, 7, 8 and 9. The mark “○” in left image and the mark “□” in right image are the correspondent pixels for the dimension calculation.

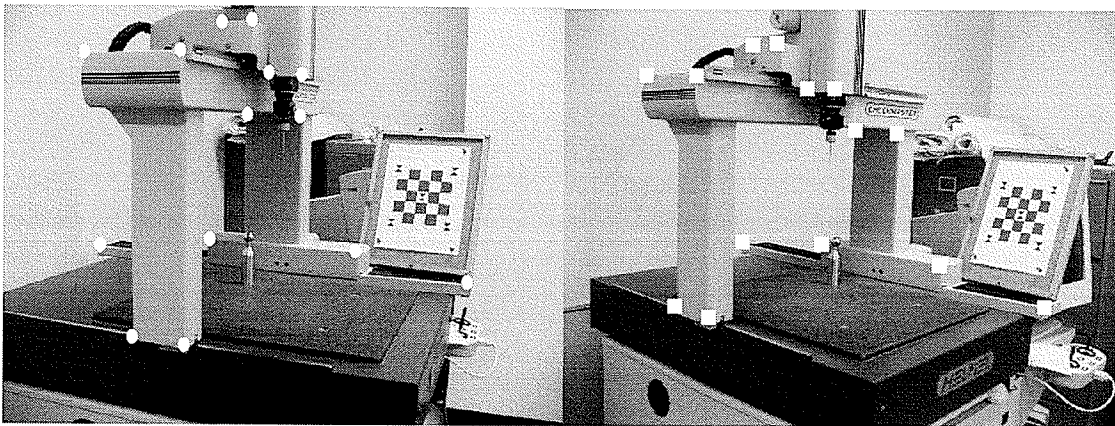


Figure 8.22 Two images for measuring widths of parts 3 to 9

Figure 8.23 is the 3D model of the CMM machine. The dimensions of each part are listed in the Table 8.2. The measuring values were measured by a ruler. The calculation values were

measured by the photogrammetry method. The accuracy of the length of parts 4, 7, 8 and 9, the width of parts 3, 5 and 9, and the height of parts 3, 4, 6 and 7 are greater than 1%. The reason is that there are smooth surfaces on those parts. The smooth surfaces consist of the chamfer or fillet faces, it is difficult to find the corresponding points on these surfaces as there are not clear identifying points. The FTP method is not used in this model construction because the detailed surface is not required to model the CMM machine.

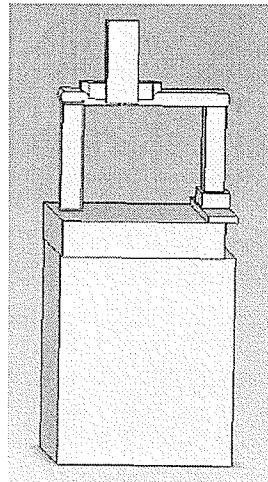


Figure 8.23 The 3D model of the CMM machine

Table 8.2 The dimensions of the CMM machine

Part	Dimensions (mm)						Accuracy (%)		
	Measuring values			Calculation values					
	Length	Width	Height	Length	Width	Height	Length	Width	Height
1	816.5	638.5	765.5	822.9	637.8	765.1	0.78	0.11	0.05
2	920.5	593.7	133.5	924.9	594.8	132.9	0.47	0.19	0.45
3	1007.8	106.2	28.8	1004.3	104.6	27.3	0.34	1.5	5.21
4	398.5	102.8	55.5	380.5	102.5	54.3	4.52	0.29	2.16
5	102.5	64.9	389.9	102.2	64.3	393.5	0.29	0.92	0.92
6	148.5	76.5	312.5	149.9	74.6	319.3	0.94	2.48	2.17
7	177.5	715.5	87.5	188.5	719.9	86.3	6.20	0.61	1.37
8	74.5	285.5	79.5	76.7	286.8	80.1	2.95	0.46	0.75
9	57.5	114.5	586.5	55.7	116.1	591.3	3.10	1.40	0.83

Chapter 9

Conclusions and Future Research

This chapter summarizes the described research, and provides proposals for improvements and future work.

9.1 Summary

The work presented in this dissertation deals with the development of image-based 3D data acquisition methods from an engineering perspective. Simplifying the operation procedure and reducing the interactive operations between operators and computers are the purpose of this research. The work consists of developing new methods and using these methods in engineering applications.

These new methods and applications are summarized as follows:

To reduce the interactive operations for camera calibration, an automatic recognition method of the checkerboard pattern for camera calibration was developed in this dissertation. First a double-triangle figure was designed and added in a common checkerboard pattern. And then an iterative algorithm was developed to find the checkerboard pattern in an image, in which a homography method was used to test the correction of found positions of double-triangle figures. The automatic recognition method could be used in camera calibration to automatically extract feature points from 2D images of the checkerboard pattern. And the interactive operations between operators and computers were reduced. Good results were also obtained in uneven illumination or complicated backgrounds.

To simplify the procedure of FTP methods, a unified calibration method in FTP-based 3D data acquisition was developed first. Only one image was needed to calculate all parameters of the acquisition system of FTP methods. There were no moving objects in the calibration process. The procedure of system calibration was simplified and the processing time was reduced. Experimental examples show the method was feasible for 3D data acquisition. Second, a correlation-based phase unwrapping algorithm was developed. The core of the method is the correlation-map function, which is proportional to the intensity modulation of a fringe image. The process for selecting the size of a filter window was skipped because the correlation-map function was selected as a parameter to identify the reliability of the phase data for phase unwrapping. The experiments show that an optimal path of phase unwrapping could be obtained by this method.

To apply the developed methods in engineering applications, an effective method for the image-based 3D detection of ice accretions on power transmission lines was first developed. The corresponding points on a transparent and smooth ice surface for 3D ice thickness calculation were successfully detected by combining the existing techniques to form a feasible and practical algorithm. The ice detection support system had been installed and tested in a real environment to support this method. Therefore the reliability of the system had been proven through tests in the real environment. Second, a VR-based data retrieval system was proposed in this research. It was a user-friendly data search system that allowed users on a team to get product information quickly. Because it provides an overview of the structure and relationships of the product data, the information needed is easily selected and edited. An image-based 3D data acquisition system was developed to aid 3D modeling for virtual environments.

9.2 Future research

The current status of the proposed methods and applications in this dissertation are not the endpoint. Several possibilities exist to further enhance the methods and applications.

The first task is to enhance the method of automatic camera calibration. This is a twofold task. On the one hand, the computing speed of the method should be improved. The method of correlation calculation should be replaced by a faster algorithm to increase the calculation speed if it is possible. On the other hand, the accuracy of the method can certainly be improved. An accurate corner finding method should be developed to obtain more accurate coordinates of the feature points.

The second task is to increase the accuracy of the unified-calibration method and the correlation-based phase unwrapping method for the FTP system. Further research will be as follows to improve the system accuracy. (1) The automatic method will be used in the unified-calibration method to detect the helper pattern. The accuracy of the method is limited on the pixel level. By using image processing methods to detect the helper pattern and the coordinates of all key points, sub-pixel accurate solutions could be obtained. (2) One of the limitations of the correlation-based phase unwrapping method is that only four computer-generated gratings and the fixed initial phase are used. Dealing with more computer-generated gratings and different initial phases to obtain an optimal value could be a very interesting area of further research.

The third task is to integrate and evaluate the image-based 3D ice detection method in real-environments and improve the method. In the current system, hoarfrost detection is still an unsolved problem. A false alarm will be sent out when the thickness of the hoarfrost is greater than the alarm threshold. Therefore it still requires that the operator makes a decision

to detect ice on the power lines by checking the ice image. A knowledge-based ice image database should be built to solve the following two problems. (1) After the ice detection system is installed in real environments, a huge amount of ice images and ice data are obtained. These imagery data are stored in an image database. It is necessary to use these data to detect hoarfrost to decrease the numbers of false alarms. (2) The operators need a lot of experience to distinguish ice or hoarfrost. The experience will be lost when an operator retires or leaves the company. The knowledge-based ice image database aims to understand the content of ice images and to store operators' knowledge. The prime function of the database is to detect the hoarfrost. The advanced function of the database can predict the ice accumulation on power lines.

Another task of further research is to extend the image-based 3D data acquisition system. Current research focuses on the area of camera calibration. Potential future work in this system lies in the development of feature matching and data registration from the engineering perspective and the integration of the 3D data from different 3D data acquisition methods. It is possible to improve the 3D data acquisition system to automatically find the corresponding points in two images. Sub-pixel accurate solutions should be considered. The current system does not include a module of data registration and therefore cannot build the whole 3D model of an object from multiple images. This is an open area for future research. Since 3D data is generated by different methods in this research, such as the photogrammetry method and the FTP method, integrating these data to build 3D models for virtual environments will also be an area for future research.

Bibliography

- Achour,K. and Benkhelif,M., “A new approach to 3D reconstruction without camera calibration”, *Pattern Recognition*, 34, pp.2467-2476 , 2001.
- Amstel, P.V., Eijk, P.V.D., etc., “An interchange format for cross-media personalized publishing”, *Computer Networks*, 33(1), pp 179-195, 2000.
- Andra, P., Mieth, U, and Osten, W., “Strategies for unwrapping noisy interferograms in phase sampling interferometry” , *Proceedings of SPIE*, 1508, pp.50-60, 1991.
- Banerjee, M., Kundu, M.K. and Mitra, P, “Corner detection using support vector machines”, *Proceedings of the 17th International Conference on Pattern Recognition*, 2(23-26), pp. 819 - 822, 2004.
- Bao,J.S., Jin, Y., Gu, M.Q., Yan, J.Q., Ma, D.Z., “Immersive virtual product development”, *Journal of Materials Processing Technology*,129(1-3), pp 592-6,2002.
- Basak, J. and Mahata, D., “A connectionist model for corner detection in binary and gray images”, *IEEE Transactions on Neural Networks*, 11(5), pp.1124 - 1132, 2000.
- Bénallal, M. and Meunier, J., “Camera Calibration with a Viewfinder”, the 15th International Conference on Vision Interface,<http://www.cipprs.org/vi2002/pdf/s5-8.pdf>, 2002.
- Borkowski, M., “Digital image processing in measurement of ice thickness on power transmission lines: a rough set approach”, Master thesis of University of Manitoba, 2002.
- Bouchouicha, M., Khelifa, M.B. and Puech, W., “A non-linear camera calibration with genetic algorithms”, *Seventh International Symposium on Signal Processing and Its Applications*, 2, pp.189-192, 2003.

Bouguet, J.Y., "Camera Calibration Toolbox for Matlab",
http://www.vision.caltech.edu/bouguetj/calib_doc/.

Branca, A., Stella, E. and Distanto, A., "A high order relaxation labeling neural network for feature matching", The 1998 IEEE International Joint Conference on Neural Networks ,2, pp.1590 - 1595,1998.

Burkett, W.C., "Product data markup language: a new paradigm for product data exchange and integration", Computer-Aided Design, 33(7), pp 489-500, 2001.

Burton, D.R., Goodall, A.J., Atkinson, J.T. and Lalor, M.J. , "The use of carrier frequency shifting for the elimination of phase discontinuities in Fourier transform profilometry", Optics and Lasers in Engineering, 23(4), pp.245-57, 1995.

Candocia, F. and Adjouadi, M., "A similarity measure for stereo feature matching", IEEE Transactions on Image Processing, 6(10), pp.1460 - 1464, 1997.

Cham, T. and Cipolla, R., "A statistical framework for long-range feature matching in uncalibrated image mosaicing", 1998 IEEE Computer Society Conference on Computer Vision and Pattern Recognition,23-25, pp.442 - 447,1998.

Chan, P., Bryanston-Cross, P.J and Judge, J.T., "Studies of Fourier transform profilometry", Proceedings of SPIE, Visual Data Exploration and Analysis, 2178, pp.165-176, 1994.

Chawla, R., Banerjee, A., "A virtual environment for simulating manufacturing operation in 3D", Proceedings of the 2001 Winter Simulation Conference, pp. 991-997, 2001.

Chen, F., Brown, G.M., and Song, M., "Overview of three-dimension Shape Measurement Using Optical Methods", Optical Engineering, 39, pp. 10-22, 2000.

Chen, W., Hu, Y., Su, X. and Tan, S., "Error caused by sampling in Fourier transform profilometry", Optical Engineering, 38(06), pp.1029-1034, 1999.

Chen, W., Su, X., Cao, Y. and Xiang, L., "Improving Fourier transform profilometry based on bicolor fringe pattern", *Optical Engineering*, 43, pp.192-198, 2004.

Chen, W., Su, X., Cao, Y., Zhang, Q. and Xiang, L., "Study on Fourier transforms profilometry based on Bi-color projecting", *ICO20: Optical Information Processing*, 6027(I), pp.602715, 2006.

Costa, C.A., Harding, J.A. and Young, R.I.M., "The application of UML and an open distributed process framework to information system design", *Computers in Industry*, 46(1), pp. 33-48, 2001.

Cumani, A., "A simple camera calibration method", *Proceedings of the 6th WSEAS International Conference on Circuits Systems*, pp. 332-337, 2002.

Damerval, C. and Meignen, S., "Blob Detection With Wavelet Maxima Lines", *IEEE Signal Processing Letters*, 14(1), pp.39 - 42, 2007.

Dovgard, R. and Basri, R., "Statistical Symmetric Shape from Shading for 3D Structure Recovery of Faces", *8th European Conference on Computer Vision, LNCS 3022*, pp.99-113, 2004.

DWG converter, "Any DWG to Image Converter", <http://anydwg.com/>.

EON, "User Guide", EON Reality Inc., 2003.

Eynard, B., Gallet, T., Nowak, P. and Roucoules, L., "UML based specifications of PDM product structure and workflow", *Computers in Industry*, 55(3), pp. 301-316, 2004.

Fernandes, K.J., Rajaa, V.H., Eyre, J., "Immersive learning system for manufacturing industries", *Computers in Industry*, 51(1), pp 31-40, 2003.

Fiona, B, Paul, P. and James, C., "The effect of windowing in Fourier transform profilometry applied to noisy images", *Optics and lasers in engineering*, 41(6), pp.815-825, 2004.

- Forbes, K., Voigt, A. and Bodika,N., “An Inexpensive, Automatic and Accurate Camera Calibration Method”, <http://dsp7.ee.uct.ac.za/~kforbes/Publications/forbes2002prasa.pdf>.
- Gao, X., Sattar, F. and Venkateswarlu, R., “Corner detection of gray level images using Gabor wavelets”, 2004 International Conference on Image Processing, 4(24-27), pp.2669 - 2672, 2004.
- Gdeisat, M. A., Burton, D.R., Lalor and M.J., “Eliminating the zero spectrum in Fourier transform profilometry using a two-dimensional continuous wavelet transform”, *Optics Communications*, 266(2), pp.482-489, 2006.
- Gonzalez, R.C. and Woods, R.E., “Digital Image Processing, 2nd edition”, Prentice Hall, 2002.
- Grégoire, C., Halleux, L., Vervoort, A., “Application of Ground Penetrating RADAR in a Mining Environment”, *Annual of University of Mining and Geology “St. Ivan Rilski”*, part II, *Minning and Mineral Processing*,46, pp.179-183, 2003.
- Guo, H., He, H., Yu, Y. and Chen, M., “Least-squares calibration method for fringe projection profilometry”, *Optical Engineering*, 44(3), pp.33603-1-9, 2005.
- Hartley, R. and Zisserman, A., “View Geometry in Computer Vision, 2nd edtion”, Cambridge University Press, 2004.
- Heath, M.D., Sarkar, S., Sanocki, T. and Bowyer, K.W, “A robust visual method for assessing the relative performance of edge-detection algorithm”, *IEEE Transactions on Pattern Analysis and Machine Intelligence*, 19(12), pp.1338 - 1359, 1997.
- Heath, M.D., Sarkar, S., Sanocki, T.and Bowyer, K.W, “A robust visual method for assessing the relative performance of edge-detection algorithms”, *IEEE Transactions on Pattern Analysis and Machine Intelligence*, 19(12), pp.1338 - 1359, 1997.

Heikkila, J. and Silven, O. , “A Four-step Camera Calibration Procedure with Implicit Image Correction”, Proceedings of the IEEE Computer Society Conference on Computer Vision and Pattern Recognition, pp.1106-1112, 1997.

Herraez, M., Burton, D., Lalor, M. and Gdeisat, M., “Fast two dimensional phase unwrapping algorithm based on sorting by reliability following a noncontinuous path”, Applied optics, 41(35), pp.7437-7444, 2002.

Hinz, S., “Fast and subpixel precise blob detection and attribution”, IEEE International Conference on Image Processing, 13(11-14), pp. III - 457-60, 2005.

Horner, J.L. and Gianino, P.D., “Phase-only matched filtering”, Applied Optics, 23, pp. 812-816, 1984.

Hu, Q., Huang, P.S., Fu, Q. and Chiang, F., “Calibration of a three-dimensional shape measurement system”, Optical Engineering, 42(2), pp.487-93, 2003.

Hua, X., Yokomichi, M. and Kono, M., “Color stereo matching based on self-organization neural networks”, The 2004 47th Midwest Symposium on Circuits and Systems, 1(25-28), pp. I-213-16, 2004.

Huang, G.Q., Huang, J., etc., “Agent-based workflow management in collaborative product development on the Internet”, Computer-Aided Design, 32(2), pp 133-144, 2000.

Huang, M. and Lai, C., “Innovative phase unwrapping algorithm: hybrid approach”, Optical engineering, 41(6), pp.1373-1386, 2002.

Huntley, J. and Coggrave, C., “Progress in phase unwrapping”, Proceedings of SPIE , 3407, pp.86-93, 1998.

Image Conversion Software, “MS Word Image Conversion and Viewing”, <http://www.snowbound.com>.

Isdale, J., "3D Scanner Technology Review", <http://vr.isdale.com/3Dscanners/3DscannerReview.html>, 1998.

Jezernik, A., Hren, G., "A solution to integrate computer-aided design (CAD) and virtual reality (VR) databases in design and manufacturing processes", *International Journal of Advanced Manufacturing Technology*, 22(11-12), pp 768-774, 2003.

Judge, T., Bryanston-Cross, P., "Review of phase unwrapping techniques in fringe analysis", *Optics and lasers in Engineering*, 21(4), pp.199-239, 1994.

Jun, J. and Kim, C., "Robust camera calibration using neural network", *Proceedings of the IEEE Region 10 Conference TENCN*, 1, pp. 694-697, 1999.

Kanade, T. and Okutomi, M., "A stereo matching algorithm with an adaptive window: theory and experiment", *IEEE Transactions on Pattern Analysis and Machine Intelligence*, 16(9), pp.920 - 932, 1994.

Korves, B., Loftus, M., "Designing an immersive virtual reality interface for layout planning", *Journal of Materials Processing Technology*, 107(1-3), pp 425-30, 2000.

Lee, J., Sun, Y. and Chen, C., "Multiscale corner detection by using wavelet transform", *IEEE Transactions on Image Processing*, 4(1), pp.100-104, 1995.

Li, G. and He, Y., "A hierarchical combined feature and area-based stereo matching algorithm", *IEEE International Symposium on Circuits and Systems*, 2(26-29), pp.II-277- II-280, 2002.

Li, J., Su, X. and Guo, L., "Improved Fourier transform profilometry for the automatic measurement of three-dimensional object shapes", *Optical Engineering*, 29(12), pp.1439-44, 1990.

- Li, J., Su, X. and Li, J., "Phase unwrapping algorithm based on reliability and edge detection", *Optical engineering*, 36(6), pp.1685-1690, 1997.
- Li, W. and Su, X., "Phase unwrapping algorithm based on phase fitting reliability in structured light projection", *Optical Engineering* ,41(6), pp.1365-1372, 2002.
- Li, W. and Su, X. , "Phase unwrapping algorithm based on phase fitting reliability in structured light projection", *Optical engineering* ,41(6), pp.1365-1372, 2002.
- Li, W. S. and Su, X.Y., "Application of improved phase-measuring profilometry in nonconstant environmental light", *Optical Engineering*, 40(3), pp. 478-485, 2001.
- Li,J. and Su, X., "The application of improved Fourier transform profilometry", *International Conference on Optoelectronic Science and Engineering '90*,1230, pp.641-2,1990.
- Lin, J. and Su, X., "Two-dimensional Fourier transform profilometry for the automatic measurement of three-dimensional object shapes", *Optical Engineering*, 34(11), pp.3297-302, 1995.
- Lu, X. and Manduchi, R., "Wide baseline feature matching using the cross-epipolar ordering constraint", *Proceedings of the 2004 IEEE Computer Society Conference on Computer Vision and Pattern Recognition* ,1, pp. I-16 - I-23 , 2004.
- Lu, Y., Wang, X. and He, G., "Phase unwrapping based on branch cut placing and reliability ordering", *Optical engineering*, 44(5), pp.055601, 2005.
- Luo, B., Cross, A.D.J. and Hancock, E.R., "Corner detection using vector potential", *Fourteenth International Conference on Pattern Recognition*, 2, pp.1018-1021, 1998.
- Massari, A., Saladini, L., etc., "a non-immersive VR system to browse multimedia databases", *IEEE International Conference on Multimedia Computing and Systems*, pp. 573-580, 1997.

- Matas, J., Soh, L.M. and Kittler, J., "Object recognition using a tag", International Conference on Image Processing, 1, pp.877-880, 1997.
- Meneses, J., Gharbi, T. and Humbert, P. , "Phase unwrapping algorithm for images with high noise content based on a local histogram", Applied optics ,44(7), pp. 1207-1215, 2005.
- Meng, X., Li, H. and Hu, Z., "A New Easy Camera Calibration Technique Based on Circular Points", Pattern Recognition, 36, pp1155-1164, 2003.
- Meng, X., Li, H. and Hu, Z., "A New Easy Camera Calibration Technique Based on Circular Points", Pattern Recognition, 36, pp1155-1164, 2003.
- Moore a, P.R., Pu, J., Ng, H.C., Wong, C.B., etc, "Virtual engineering: an integrated approach to agile manufacturing machinery design and control", Mechatronics, 13(10), pp 1105-21, 2003.
- Open Computer Vision Library, <http://sourceforge.net/projects/opencvlibrary/>.
- Paillot, D., Merienne, F., Thivent, S., "CAD/CAE visualization in virtual environment for automotive industry", Eurographics Workshop on Virtual Environments, pp 315-16, 2003.
- Pei, S. and Ding, J., "New corner detection algorithm by tangent and vertical axes and case table", IEEE International Conference on Image Processing, 1(11-14), pp. I-365-8, 2005.
- Penersini, F., Pozzoli, E., Sarti, A. and Tubaro, S, "Multi-resolution corner detection", 2000 International Conference on Image Processing, 3(10-13), pp.881 - 884, 2000.
- Peng, Q. and Yu, C., "A visualized manufacturing information system for mass customization", International Journal of Manufacturing Technology and Management, 2007.
- Q. Peng, C. Chung, C. Yu, and T. Luan, A Networked Virtual Manufacturing Systems for SMEs, International Journal of Computer Integrated Manufacturing, 20 (1), p. 71 -79, 2007.

Q. Peng and C. Yu, Enhanced integrated manufacturing systems in an immersive virtual environment. Proc. Instn. Mech. Engrs, Part B: Journal of Engineering Manufacture, Vol. 221(3), p. 477-487, 2007.

Peng, Q., and Loftus, M., "An Image-based Fast Three-dimensional Modeling Method for Virtual Manufacturing", Journal of Engineering Manufacture, 214, pp709-721, 2000.

Peng, Q., Chung, C., Yu, C., and Luan, T., "A networked virtual manufacturing systems for SMEs", International Journal of Computer Integrated Manufacturing, 20 (1), p. 71 -79, 2007.

Pollefeys, M., Koch, R., Vergauwen, M. and Gool, L., "Automated reconstruction of 3D scenes from sequences of images", Journal of Photogrammetry and Remote Sensing, 55(4), pp. 251-267, 2000.

Pratt, W., "Digital image processing, 3rd edition", John Wiley and Sons, Inc., 2001.

Quan, C., He, X. Y., Wang, C.F., Tay, C.J., Shang, H.M., "Shape measurement of small objects using LCD fringe projection with phase shifting", Optics Communications, pp. 21-29, 2001.

Qurban, M. and Sohaib, K., "Camera calibration and three-dimensional world reconstruction of stereo-vision using neural networks", International Journal of Systems Science, 32(9), pp. 1155-1159, 2001.

Roques, P., "UML in practice", John Wiley & Sons Ltd., 2004.

Rumbaugh, J., Jacobson, Ivar and Booch, G., "The unified modeling language reference manual", Addison Wesley Longman, Inc., 1999.

Salomone, T.A., "What every engineer should know about concurrent engineering", Marcel Dekkey, Inc., 1995.

- Salvimas, J., "An Approach to Coded Structured Light to Obtain Three Dimensional Information", Ph.D. Thesis, University of Girona, 2001.
- Sansoni, G., Biancardi, L., Minoni, U. and Docchio, F., "Novel, adaptive system for 3-D optical profilometry using a liquid crystal light projector", IEEE Transactions on Instrumentation and Measurement, 43(4), pp. 558-566, 1994.
- Santos, C.R.D., Gros, P., etc, "Experiments in information visualization using 3D metaphoric worlds", Enabling Technologies: Infrastructure for Collaborative Enterprises, Proceedings. IEEE 9th International Workshops, pp51-58, 2000.
- Savadjiev, K. and Farzaneh, M., "Modeling of Icing and Ice Shedding on Overhead Power Lines Based on Statistical Analysis of Meteorological Data", IEEE Transactions on power delivery, 19(2), pp.715-721, 2004.
- Shen, W and Wang, L., "Web-based and agent-based approaches for collaborative product design: an overview", International journal of computer application in technology, 16(2/3), pp.103-112, 2003.
- Shu, C., Brunton, A. and Fiala, M., "Automatic Grid Finding in Calibration Patterns Using Delaunay Triangulation", Technical Report, NRC-46497/ERB-1104, Nat. Research Council, Inst. for Information Technology, 2003.
- Soetebier, I., Dorner R. and Braun, N., "Seamless integration of databases in VR for constructing virtual environments", European Association for Computer Graphics 20th Annual Conference, 18(3), pp C331-C338., 1999.
- Soh, L.M. and Kittler, J. , "Robust recognition of calibration charts", Sixth International Conference on Image Processing and Its Applications, 2, pp.487-491, 1997.

Stojanovic, R. S., Koubias, S., and Georgoudakis, E., "A Measuring Method for Laser-Based Profilometry and Its Application in Non-Destructive Testing and Quality Control", Proceedings of the 5th International Conference on Vibration Measurements by Laser Techniques – Advances & Applications, 4827, pp. 553-563, 2002.

Sturm P.F. and Maybank, S.J., "On plane-based camera calibration: A general algorithm, singularities, applications", IEEE Computer Society Conference on Computer Vision and Pattern Recognition, 1, pp. 23-25, 1999.

Su, X. and Chen, W., "Reliability-guided phase unwrapping algorithm: a review", Optics and Lasers in Engineering, 42(3), pp. 245-261, 2004.

Su, X., "Phase unwrapping techniques for 3-D shape measurement", Proceedings of SPIE, 2866, pp.460-465, 1996.

Su, X. and Xue, L., "Phase unwrapping algorithm based on fringe frequency analysis in Fourier-transform profilometry", Optical Engineering, 40(4), pp 637-643, 2001.

Su, X., Bally, G. and Vukicevic, D., "Phase-stepping grating profilometry: utilization of intensity modulation analysis in complex objects evaluation", Optics communications, 98, pp.141-150, 1993.

Su, X., Chen, W., Cao, Y., Zhang, Q. and Xiang, L., "Method for eliminating zero spectrum in Fourier transform profilometry", Optics and Lasers in Engineering, 43(11), pp.1267-76, 2005.

Su, X., Sajan, M.R. and Asundi, A.K., "Fourier transform profilometry for 360-deg shape using TDI camera", Int. Conference on Experimental Mechanics: Advances and Applications, 2921, pp.552-556, 1997.

Su, X.Y. and Chen, W. J., "Fourier transform profilometry: a review", *Optics and lasers in Engineering*, 35, pp. 263-284, 2001.

Takeda, M. and Abe, T., "Phase unwrapping by a maximum cross-amplitude spanning tree algorithm: a comparative study", *Optical engineering*, 35(8), pp.2345-2351, 1996.

Takeda, M. and Mutoh, K., "Fourier Transform Profilometry for the Automatic measurement of 3-D Object Shapes", *Applied Optics*, 22(4), pp.3977-3982, 1983.

Tsai, R.Y., "A versatile camera calibration technique for high accuracy 3D machine vision metrology using off-the-shelf TV cameras and lenses", *IEEE Journal on Robotics Automation*, 3(4), pp. 323-344, 1987.

Valkenburg, R.J., "Camera Calibration Using Multiple Reference", *Image and Vision Computing*, pp. 61-66, 1996.

Vincent, E and Laganier R., "An Empirical Study of Some Feature Matching Strategies", *The 15th International Conference on Vision Interface*, <http://www.cipprs.org/vi2002/abstracts.html>, 2002.

Wang, K., "Adaptive stereo matching algorithm based on edge detection", *International Conference on Image Processing*, 2(24-27), pp.1345 - 1348, 2004.

Wang, Y.S., Fu, S., Xu, J.Q., Zhou, C.L., Si, S.C. and Gao, C.Y., "Application of wavelet digital filter of fourier transform profilometry in 3-D measurement", *11th International Manufacturing Conference - Advances in Materials Manufacturing Science and Technology*, 471-472, pp.654-657, 2004.

Yang, C. and Jiang, T. A., "Developing an integration framework to support the information flow between PDM and MRP", *Advanced Manufacturing Technology*, 19(2), pp. 131-141, 2002.

Yang, C. and Pei, H.N., "Developing a STEP-Based Integration Environment to Evaluate the Impact of an Engineering Change on MRP", *Advanced Manufacturing Technology*, 15(11), pp 769-779, 1999.

Yang, C., Sun, F., and Hu, Z. , "Planar conic based camera calibration", 15th International Conference on Pattern Recognition,1, pp. 3-7, 2000.

Yi, J. and Huang, S., "Modified Fourier transform profilometry for the measurement of 3-D steep shapes", *Optics and Lasers in Engineering*, 27(5), pp.493-505, 1997.

Yu, C. and Peng, Q., "A correlation-based phase unwrapping method for Fourier-transform profilometry", *Optics and Lasers in Engineering*, 45(6), pp.730-736, 2007.

Yu, C. and Peng, Q., "A unified-calibration method in FTP-based 3D data acquisition for reverse engineering", *Optics and Lasers in Engineering*, 45(3), pp.396-404, 2007.

Yu, C. and Peng, Q., "Robust recognition of checkerboard pattern for camera calibration", *Optical Engineering*, 45(9), pp.093201-(1-9), 2006.

Yu, C. Wu, L. and Peng, Q., "A VR-based data retrieval system", ASME 2005 International Design Engineering Technical Conferences & Computers and Information in Engineering Conference, pp. 1083-1091, 2005.

Yu, C., Peng, Q., Wachal, R. and Wang, P., "An image-based 3D acquisition of ice accretions on power transmission lines", Canadian conference on electrical and computer engineering, IEEE Canada, pp. 1974-1977, 2006.

Zhang, R., Tsai, P.S., Cryer, J.E., and Shah, M., "Shape from Shading: A Survey", *IEEE Transactions on pattern analysis and machine intelligence*, 21(8), pp.690-706, 1999.

Zhang, X., Lin, Y., Zhao, M., Niu, X. and Huang, Y., "Calibration of a fringe projection profilometry system using virtual phase calibrating model planes", *Journal of Optics A: Pure and Applied Optics*, 7(4), pp. 192-197, 2005.

Zhang, Z., "Flexible Camera Calibration by Viewing a Plane from Unknown Orientations", *Proceedings of the Seventh IEEE International Conference on Computer Vision*, 1, pp. 20-27, 1999.

Zhang, Z., "Camera calibration with one-dimensional objects", *IEEE Transactions on Pattern Analysis and Machine Intelligence*, 26, pp.892 – 899, 2004.

Zhang, Z.Y., "A Flexible New Technique for Camera Calibration", *IEEE on Pattern Analysis and Machine Intelligence*, 22(11), pp.1330-1334, 2000.

Zhaoxue, C. and Pengfei, S., "Efficient method for camera calibration in traffic scenes", *Electronics Letters*, 40, pp.368-369, 2004.

Zheng, Z., Wang, H. and Teoh, E.K., "Analysis of gray level corner detection", *Pattern Recognition Letters*, 20(2), pp.149-162, 1999.

Ziou, D. and Tabbone S., "Edge Detection Techniques - An Overview", *International Journal of Pattern Recognition and Image Analysis*, 8, pp.537-559, 1998.

Curriculum Vitae

Name: Chunsheng Yu

E-mail: umyu1@cc.umanitoba.ca, chunsheng_yu@yahoo.com

Telephone: 1-204-474-8572 (O)

Mailing Address: Department of Mechanical and Manufacturing Engineering,
University of Manitoba, 15 Gillson St. Winnipeg, Manitoba
Canada R3T 5V6

EDUCATION

Doctor of Philosophy, Mechanical and Manufacturing Engineering, The University of Manitoba, Canada, 09/2002-Present.

Master of Science, Mechanical Design Engineering, Northeast University, China, 02/1997.

Bachelor of Engineering, Mechanical Design Engineering, Taiyuan Heavy Machine Institute, China, 07/1993.

PUBLICATIONS

Refereed Papers in Scientific Journals

- (1) **C. Yu** and Q. Peng, A unified-calibration method in FTP-based 3D data acquisition for reverse engineering, *Journal of Optics and Lasers in Engineering*, 2007, 45(3), p. 396–404.
- (2) **C. Yu** and Q. Peng, A correlation-based phase unwrapping method for Fourier-transform profilometry. *Journal of Optics and Lasers in Engineering*, 2007, 45(6), p. 730–736.
- (3) **C. Yu** and Q. Peng, Robust recognition of checkerboard pattern for camera calibration, *J of Optical Engineering*, 2006, 45(9), p. 093201-(1-9).

- (4) Q. Peng and **C. Yu**, Enhanced integrated manufacturing systems in an immersive virtual environment. Proc. Instn. Mech. Engrs, Part B: Journal of Engineering Manufacture, 2007, Vol. 221(3), p. 477-487.
- (5) Q. Peng and **C. Yu**, A visualised manufacturing information system for mass customisation, International Journal of Manufacturing Technology and Management, 2007, 11(3/4), p. 278-295.
- (6) Q. Peng, C. Chung, **C. Yu**, and T. Luan, A Networked Virtual Manufacturing Systems for SMEs, International Journal of Computer Integrated Manufacturing, 2007, 20 (1), p. 71 - 79.
- (7) **C. Yu** and L. Sun, etc., "A CAD/CAE Integrated System for Light Bus Body Structure", Automotive engineering, 2000

Refereed Conference Presentations and Proceedings

- (1) **C. Yu**, Q. Peng, R. Wachal and P. Wang, "An image-based 3D acquisition of ice accretions on power transmission lines", Proceedings of Canadian conference on electrical and computer engineering, p. 1974-1977, 1-4244-0038-4 2006 IEEE, CCECE/CCGEI, Ottawa, May 7-10 2006.
- (2) **C. Yu**, L. Wu and Q. Peng, "3D shape acquisition using an FTP-based method in product modeling", The second CDEN International Conference on Design Education, Innovation, and Practice, Kananaskis, Alberta, Canada, July 18-20, 2005.
- (3) **C. Yu**, Q. Peng and L. Wu, "A VR-based data retrieval system", ASME 2005 Design Engineering Technical Conferences and Computers and Information in Engineering Conference, DETC2005-84325, Long Beach, California, USA, September 24-28, pp. 1083-1091, 2005.
- (4) **C. Yu** and Q. Peng, "A VE-based Data Retrieval System to Enhance Concurrent Engineering", Accepted by "the 11th ISPE International Conference on Concurrent Engineering", 2004